# Pattern Projection Profilometry for 3D Coordinates Measurement of Dynamic Scenes

Elena Stoykova, Jana Harizanova and Ventseslav Sainov

Central Laboratory of Optical Storage and Processing of Information Bulgarian Academy of Sciences

## Introduction

Three-dimensional time-varying scene capture is a key component of dynamic 3D displays. Fast remote non-destructive parallel acquisition of information being inherent property of optical methods makes them extremely suitable for capturing in 3D television systems. Recent advance in computers, image sensors and digital signal processing becomes a powerful vehicle that motivates the rapid progress in optical profilometry and metrology and stimulates development of various optical techniques for precise measurement of 3D coordinates in machine design, industrial inspection, prototyping, machine vision, robotics, biomedical investigation, 3D imaging, game industry, culture heritage protection, advertising, information exchange and other fields of modern information technologies.

To meet the requirements of capturing for the needs of 3D dynamic displays the optical profilometric methods and systems must ensure accurate automated real-time full-field measurement of absolute 3D coordinates in a large dynamic range without loss of information due to shadowing and occlusion. The technical simplicity, reliability and cost of capturing systems are also crucial factors. Some of the already commercialized optical systems for 3D profilometry of real objects are based on laser scanning. As the scanning of surfaces is realized one-dimensionally in space and time (point by point or line by line) at limited speed, especially for large-scale scene in out-door conditions, these systems are subject to severe errors caused by vibration, air turbulence and other environmental influence and are not applicable for measurement in real time. Among existing techniques, the methods which rely on functional relationship of the sought object data with the phase of a periodic fringe pattern projected onto and reflected from the object occupy a special place as a full-field metrological means with non-complex set-ups and processing algorithms that are easy to implement in outdoor and industrial environment. Pattern Projection Profilometry (PPP) includes a wide class of optical methods for contouring and shape measurement going back to the classical shadow and projection moiré topography [1, 2] and the well-known and widely used since the ancient times triangulation. Nowadays, pattern projection systems enable fast non-ambiguious precise measurement of surface profile of wide variety of objects from plastic zones in the notch of the micro-cracks in fracture mechanics [3] and micro-components [4] to cultural heritage monuments [5]. An optimized and equipped with a spatial light modulator (SLM) system provides measurement accuracy up to $5.10^{-5}$ from the object size [1].

The main goal of this Chapter is to consider phase-measuring methods in pattern projection profilometry as a perspective branch of structured light methods for shape measurement emphasizing on the possibility to apply these methods for time-varying scene capturing in the dynamic 3D display. The Chapter consists of 3 Sections. Section 1 gives the basic principles of PPP and Phase Measuring Profilometry (PMP), describes the means for generation of sinusoidal fringe patterns, formulates the tasks of phase demodulation in a profilometric system and points out the typical error sources influencing the measurement. Section 2 deals with phase-retrieval methods. They are divided in two groups – multiple frame and single frame methods or temporal and spatial methods. Following this division, we start with the phase-shifting approach which is outlined with its pros and cons. Special attention is dedicated to error-compensating algorithms and generalized phase-shifting techniques. Among special methods, the Fourier transform method is discussed in detail. The generic limitations, important accuracy issues and different approaches for carrier removal are enlightened. Space-frequency representations as the wavelet and windowed Fourier transforms for phase demodulation are also considered. Other pointwise strategies for demodulation from a single frame as quadrature filters, phase-locked loop and regularized phase tracking are briefly presented. The problem of phase unwrapping which is essential for many of the phase retrieval algorithms is explained with classification of the existing phase-unwrapping approaches. The Chapter also includes the developed by the Central Laboratory of Optical Storage and Processing of Information to the Bulgarian Academy of Sciences (CLOSPI-BAS) experimental set-ups as well as the technical solutions of problems associated with measurement of the absolute 3D coordinates of the objects and the loss of information due to shadowing effect. In the end, we discuss the phase demodulation techniques from the point of view of observation of fast dynamic processes and the current development of real-time measurements in the PMP. This work is supported by EC within FP6 under Contract 511568 "3DTV".

## 1 Pattern Projection Profilometry

### 1.1 General Description

The principle of PPP is elucidated with the scheme depicted in Fig. 1. The optical axes of both projector system and observation system are crossed at

AU: We have shortened the running head. Is this ok.

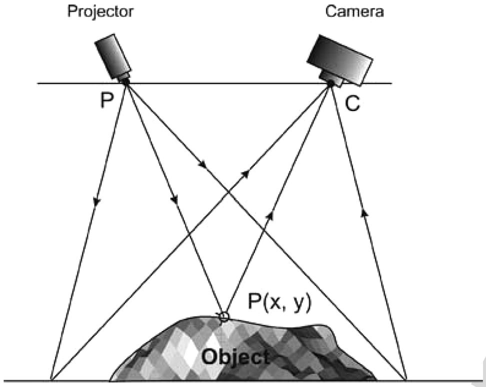

**Fig. 1.** Schematic of pattern projection profilometry

a certain plane called reference plane. Although there exist methods based on a random pattern projection, the PPP generally relies on structured light projection [1]. In structured light techniques a light pattern of a regular structure such as a single stripe, multiple stripes, gradients, grids, binary bars, or intensity modulated fringes as e.g. a sine-wave, is projected onto the object. The object reflects the deformed light pattern when observed from another angle. Analysis of the deformed image captured with a CCD camera yields the 3D coordinates of the object provided known positions of the camera, the projector and the object. The procedure to obtain the required geometric relationships for calculation of coordinates is called camera calibration [6].

The accuracy of the measurement crucially depends on correct determination of the stripe orders of the reflected patterns and on their proper connection to the corresponding orders in the projected patterns. This presumes one or more patterns to be projected – the simpler the pattern structure, the bigger the number of patterns required to derive the object's profile. For example, in the so-called Gray-code method systems [7] several binary patterns of varying spatial frequency are projected. Number of projections needed to compensate scarce information in binary pattern projection is substantially reduced by intensity or colour modulation of the projected patterns. Projection of more complicated patterns with increased number of stripes and intensity differences between the stripes involves more accurate but more difficult interpretation of the captured images.

A detailed review and classification of coded patterns used in projection techniques for the coordinates measurement is presented in [8]. The patterns are unified in three subdivisions based on spatial, temporal (time-multiplexing) or direct codification. The first group comprises patterns whose points are coded using information from the neighbouring pixels. The advantage of such an approach is capability for measurement of time-varying scenes. Its disadvantage is the complicated decoding stage due to shadowing effect as the surrounding area cannot always be recovered. Time-multiplexing approach is based on measurement of intensity values for every pixel as a sequence in time. In practice, this is achieved by successive projection of a set of patterns onto the object surface that limits its application only to static measurements. The codeword for a given pixel is usually formed by a sequence of intensity values for that pixel across the projected patterns. The third subdivision is based on direct codification which means that each point of the pattern is identified just by itself. There are two ways to obtain pixel coordinates using this type of pattern: by increasing the range of colour values or by introducing periodicity in the pattern. These techniques are very sensitive to noise due to vibration, shadowing, saturation or ill-illumination. Thus, preliminary calibration is needed in order to eliminate the colour of the objects using one or more reference images that make the method inapplicable for time-varying scenes measurements.

An attractive approach among structured light methods is the phase measuring profilometry (PMP) [9, 10] or fringe projection profilometry, in which the parameter being measured is encoded in the phase of a two-dimensional (2D) periodic fringe pattern. The main obligatory or optional steps of the PMP are shown schematically in Fig. 2. The phase measuring method enables determination of 3D coordinates of the object with respect to a reference plane or of absolute 3D coordinates of the object itself. The phase extraction requires a limited number of patterns and for some methods may need only one pattern, thus making real-time processing possible. Nowadays, the PMP is a highly sensitive tool in machine vision, computer-aided design, manufacturing, engineering, virtual reality, and medical diagnostics. A possibility for real-time remote shape control without the simultaneous physical presence of the two objects by using a comparative digital holography is shown in [11]. For the purpose, the digital hologram of the master object is recorded at one location and transmitted via Internet or using a telecommunication network to the location of the tested object where it is fed into a spatial light modulator (SLM).

### 1.2 Methods for Pattern Projection

In general, the pattern projected onto the object in the PMP is described by a periodic function, $f \in [-1, 1]$. The most of the developed algorithms

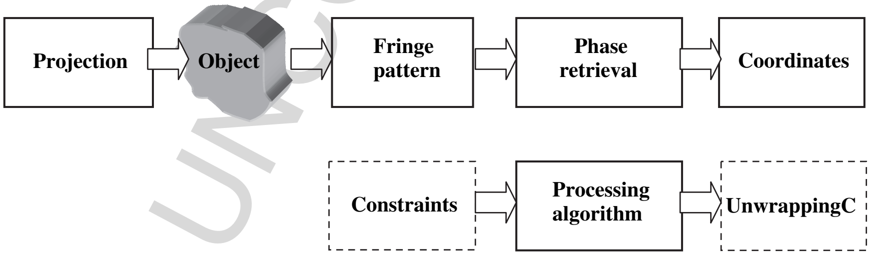

**Fig. 2.** Block-scheme of phase-measuring profilometry

in the PMP presume a sinusoidal profile of fringes, which means that these algorithms are inherently free of errors only at perfect sinusoidal fringe projection. Projection of purely sinusoidal fringes is not an easy task. The fringes that fulfil the requirement of $f = \cos[\ldots]$ can be projected by coherent light interference of two enlarged and collimated beams. As the fringes are in focus in the whole space, this method makes large-depth and large-angle measurements possible, however at limited lateral field of measurement, restricted by the diameter of the collimating lens. The main drawback of interferometrically created fringes is the complexity of the used set-up and vulnerability to the environmental influences as well as the inevitable speckle noise produced by coherent illumination. An interesting idea how to keep the advantages of coherent illumination and to avoid the speckle noise is proposed in [12] where the light source is created by launching ultra short laser pulses into highly nonlinear photonic crystal fibres.

Using of conventional imaging system with different types of single-, dual-, and multiple-frequency diffraction gratings, as an amplitude or phase sinusoidal grating or Ronchi grating, enlarges the field of measurement and avoids the speckle noise, however, at the expense of higher harmonics in the projected fringes. In such systems, a care should be taken to decrease the influence of the higher harmonics, e.g. by defocused projection of a Ronchi grating or by using an area modulation grating to encode almost ideal sinusoidal transparency as it is described in [9, 13]. A new type of projection unit based on a diffractive optical element in the form of saw tooth phase grating is described in [14]. The use of a programmable SLM, e.g. liquiud crystal display (LCD) [15, 16] or digital micro-mirror device (DMD) [17, 18, 19], permits to control very precisely the spacing, colour and structure of the projected fringes [20, 21], and to miniaturize the fringe projection system enabling applications in space-restricted environment [22]. Synthetic FPs produced by an SLM, however, also suffer from the presence of the higher harmonics. The discrete nature of the projected fringes entails tiny discontinuities in the projected pattern that lead to loss of information. This problem is more serious for the LCD projectors whereas the currently available DMD chips with 4k × 4k pixel resolution make the digital fringe discontinuities a minor problem [23]. For illustration, Figs. 3–5 show schematically implementation of the PMP based on classical Max-Zhender interferometer (Fig. 3) [24], on DMD projection (Fig. 4) [25] and by using a phase grating (Fig. 5) [26]. The wrapped phase maps and 3D reconstruction of the objects for these three types of illumination are presented in Fig. 6.

### 1.3 Phase Demodulation

The 2D fringe pattern (FP) that is phase modulated by the physical object being measured may be represented by the following mathematical expression:

$$I(\vec{r},t) = I_B(\vec{r},t) + I_V(\vec{r},t) f[\varphi(\vec{r},t) + \phi(\vec{r},t)] \quad (1)$$

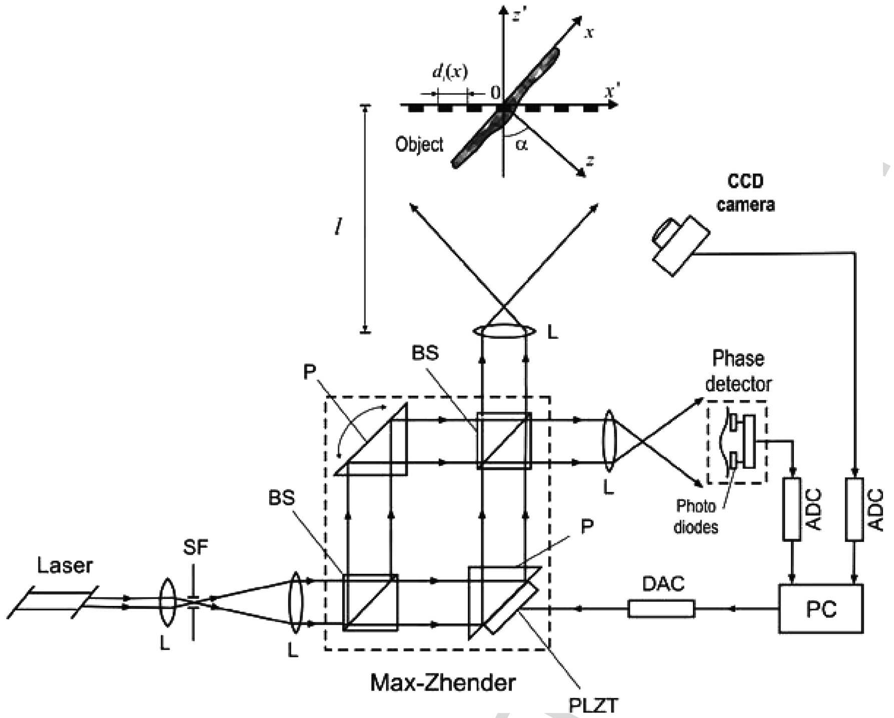

**Fig. 3.** Fringe projection system, based on a Mach-Zhender interferometer: L – lens; BS – beam splitter; SF – spatial filter; P – prism; PLZT – phase-stepping device

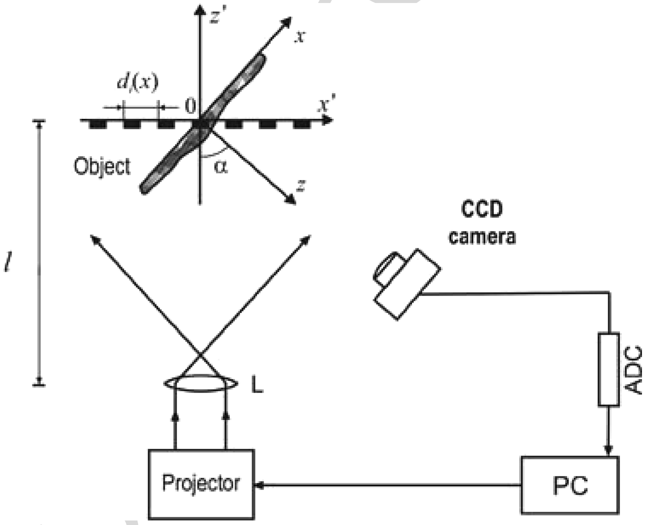

**Fig. 4.** Fringe projection system, based on computer generated fringe patterns. L – lens

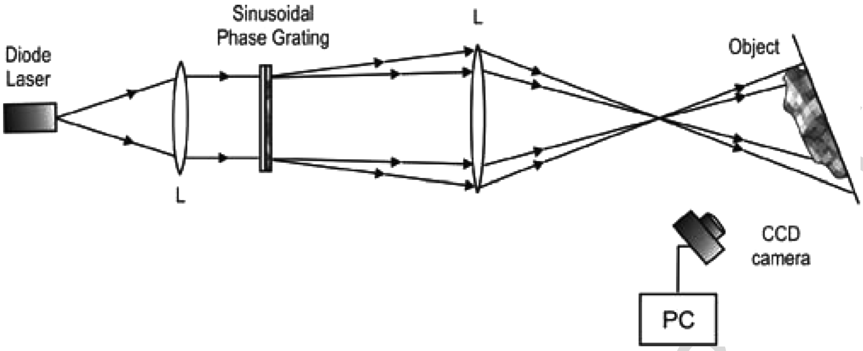

**Fig. 5.** Fringe projection system based on a sinusoidal phase grating; L – lens

where $I_B(\vec{r}, t)$ is a slowly varying background intensity at a point $\vec{r}(x, y)$ and a moment $t$, $I_V(\vec{r}, t)$ is the fringe visibility that is also a low-frequency signal, $\varphi(\vec{r}, t)$ is the phase term related to the measured parameter, e.g. object profile. The phase term $\phi(\vec{r}, t)$ is optional being introduced during the formation of the waveform $f$ or during the phase evaluation. The continuous FP (1) recorded at a moment $t$ is imaged over a CCD camera and digitized for further analysis as a 2D matrix of quantized intensities $I_{ij} \equiv I(x = i\Delta x, y = j\Delta y)$ with dimensions $N_x \times N_y$, where $\Delta x$ and $\Delta y$ are the sampling intervals along X and Y axes and define the spatial resolution, $N_x$ is the number of columns and $N_y$ is the number of rows. The camera spatial resolution is a crucial parameter for techniques based on the principle of optical triangulation. The brightness of each individual matrix element (pixel) is given by an integer that varies from the minimum intensity, equal to 0, to the maximum intensity, equal e.g. to 255. The purpose of computer-aided fringe analysis is to determine $\varphi(\vec{r}, t)$ across the pattern and to extract the spatial variation of the parameter being

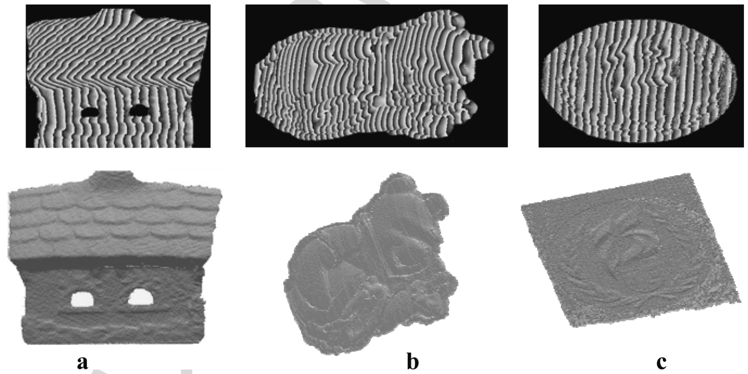

**a** **b** **c**

**Fig. 6.** Wrapped phase maps and 3D reconstruction of objects obtained with sinusoidal fringes generated using **a**) interferometer, **b**) DMD, **c**) phase grating

measured. In the case of profilometry, once the phase of the deformed waveform is restored, nonambiguous depth or height values can be computed. The process of phase retrieval is often called phase evaluation or phase demodulation. The fringe density in the FP is proportional to the spatial gradient of the phase [27]. Hence evaluation of the fringe density is also close to phase demodulation.

In general, the phase retrieval includes the steps:

(i) Phase evaluation step in which a spatial distribution of the phase, the so-called phase map, is calculated using one or more FPs. As the phase-retrieval involves nonlinear operations, implementation of many algorithms requires some constraints to be applied.
(ii) The output of the phase evaluation step, in most cases, yields phase values wrapped onto the range $-\pi$ to $\pi$, which entails restoration of the unknown multiple of $2\pi$ at each point. Phase unwrapping step is a central step to these algorithms, especially for realization of the automatic fringe analysis.
(iii) Elimination of additional phase terms introduced to facilitate phase measurement by an adequate least squares fit, an iterative process or some other method is sometimes required.

Historically, the PMP has emerged from the classical moiré topography [28], in which the fringes modulated by the object surface create a moiré pattern. In the dawn of the moiré topography operator intervention was required for assignment of fringe-orders, determination of fringe extrema or interpositions. Over the years, the phase-measuring systems with coherent and non-coherent illumination that realize the principles of moiré, speckle and holographic interferometry have been extensively developed for measurement of a wide range of physical parameters such as depth, surface profile, displacement, strain, deformation, vibration, refractive index, fluid flow, heat transfer, temperature gradients, etc. The development of interferometric methodology, image processing, and computer hardware govern the rapid progress in automation of fringe analysis. Gradually, a host of phase evaluation algorithms have been proposed and tested. A detailed overview of phase estimation methods is given in [29]. In terms of methodology, most algorithms fall into either of two categories: temporal or spatial analysis. A common feature of temporal analysis methods is that the phase value of a pixel is extracted based on the phase-shifted intensities of this pixel. Spatial analysis methods extract a phase value by evaluating the intensity of a neighbourhood of the pixel being studied [30]. A temporal analysis method is the phase-shifting profilometry. Typical spatial analysis methods are Fourier transforms methods with carrier fringes and without carrier fringes. Recently, the wavelet transform method has started to gain popularity. A crucial requirement for implementation of any algorithm is the ability for automatic analysis of FPs [31]. Another important requirement for capture of 3D coordinates is to perform the measurement in real time. From this point of view, the methods capable to extract phase information from a single frame are the most perspective. In order to replace the conventional 3D coordinate measurement machines using contact styli, the PMP should be able to measure diffusely reflecting surfaces and to derive correct information about discontinuous structures such as steps, holes, and protrusions [32].

### 1.4 Conversion from Phase Map to Coordinates

Usually, in the PMP the depth of the object is determined with respect to a reference plane. Two measurements are made for the object and for the reference plane that yield two phase distributions $\varphi_{obj}(x, y)$ and $\varphi_{ref}(x, y)$, respectively. The object profile is retrieved from the phase difference, $\Delta\varphi(x, y) = \varphi_{obj}(x, y) - \varphi_{ref}(x, y)$. Calibration of the measurement system, i.e. how to calculate the 3D coordinates of the object surface points from a phase map, is another important issue of all full-field phase measurement methods. The geometry of a conventional PMP system is depicted in Fig. 7. The reference plane is normal to the optical axis of the camera and passes through the cross-point of the optical axes of the projector and the camera. The plane $\mathrm{X}_C\mathrm{OY}_C$ of the Cartesian coordinate system $(\mathrm{OX}_C\mathrm{Y}_C\mathrm{Z}_C)$ coincides with the reference plane and the axis $\mathrm{Z}_C$ passes through the camera center. The plane P which is taken to pass through the origin of $(\mathrm{OX}_C\mathrm{Y}_C\mathrm{Z}_C)$ is normal to the optical axis of the projector. The Cartesian coordinate system $(\mathrm{OX}_P\mathrm{Y}_P\mathrm{Z}_P)$ with the plane $\mathrm{X}_P\mathrm{OY}_P$ coinciding with the plane P and axis $\mathrm{Z}_P$ passing through the center of the projector system can be transformed to $(\mathrm{OX}_C\mathrm{Y}_C\mathrm{Z}_C)$ by rotations around the $\mathrm{X}_C$ axis, $\mathrm{Y}_C$ axis, and $\mathrm{Z}_C$ axis in sequence, through the angles $\alpha$, $\beta$, and $\gamma$, respectively. Mapping between the depth and the phase difference depends on positions and orientations of the camera and projector, fringe spacing, location of the reference plane, etc. It is important to note that the mapping is described by the non-linear function [33]. According to

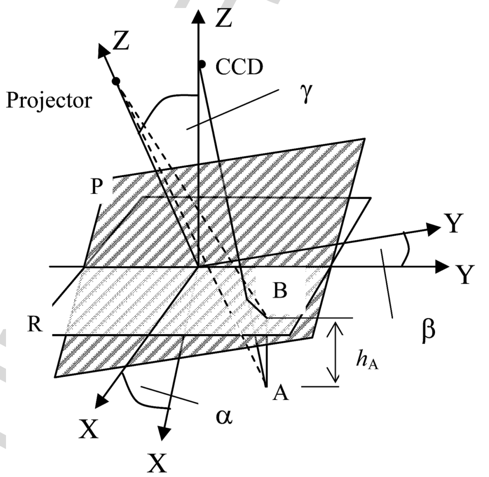

**Fig. 7.** Geometry of the pattern projection system. The depth (*or height*) of the object point A with respect to the reference plane R is $h_A$

the geometry depicted in Fig. 7, the phase difference at the camera pixel $(x = i\Delta x, y = j\Delta y)$ is connected to the depth (or height) $h_{ij}$ of the current point A on the object as viewed by the camera in $(x = i\Delta x, y = j\Delta y)$ with respect to the reference plane R by the expression [33]:

$$\Delta\varphi(x = i\Delta x, y = j\Delta y) \equiv \Delta\varphi_{ij} = \frac{a_{ij}h_{ij}}{1 + b_{ij}h_{ij}} \tag{2}$$

where the coefficients $a_{ij} = a_{ij}(L_P, L_C, d, \alpha, \beta, \gamma)$ and $b_{ij} = b_{ij}(L_P, L_C, d, \alpha, \beta, \gamma)$ depend on coordinates of point A, the rotation angles between $(\mathrm{OX}_C\mathrm{Y}_C\mathrm{Z}_C)$ and $(\mathrm{OX}_P\mathrm{Y}_P\mathrm{Z}_P)$, fringe spacing $d$ and distances $L_\mathrm{P}$ and $L_\mathrm{C}$ of the projector and the camera, respectively, to the reference plane. If the PMP is used for investigation of a specularly reflective surface, which acts as a mirror, the phase of the FP recorded by the CCD is distorted proportionally to the slope of the tested object [34]. In this simple model it is assumed that the lateral dimensions given usually by x and y coordinates are proportional to the image pixel index $(i, j)$. However, this simplified model gives inaccurate formulas in case of lens distortion and if magnification varies from point to point, which destroys proportionality of the $x$ and $y$ coordinates to the image index $(i, j)$ [35]. Reliable conversion of the phase map to 3D coordinates needs a unique absolute phase value. This phase value can be obtained using some calibration mark, e.g. one or several vertical lines with known positions on the projector at digital fringe projection. Calibration of PMP system based on a DMD digital fringe projection is addressed in [23] where a new phase-coordinate conversion algorithm is described. In [36] calibration is governed by a multi-layer neural network trained by using the data about the FP's irradiance and the height directional gradients obtained for the test object. In this way, it is not necessary to know explicitly the geometry of the profilometric system.

## 1.5 Error Sources

An important issue of all phase determination techniques is their accuracy and noise tolerance. It seems logical to adopt the following general model of the recorded signal:

$$\begin{aligned} I(\vec{r},t) = {} & N_m(\vec{r},t)\,\{I_B(\vec{r},t) + I_V(\vec{r},t) f[\varphi(\vec{r},t) \\ & + \phi(\vec{r},t) + N_{ph}(\vec{r},t)]\} + N_a(\vec{r},t) \end{aligned} \tag{3}$$

where the terms $N_m(\vec{r},t)$, $N_a(\vec{r},t)$ and $N_{ph}(\vec{r},t)$ comprise the possible deterministic and random error sources. Depending on the processing algorithm and the experimental realization of the profilometric measurement multiple error sources of different nature will affect the accuracy of phase restoration and henceforth, the 3-D profile recovery becomes a challenging task. Environmental error sources as mechanical vibration, turbulent and laminar air flows in the optical path, dust diffraction, parasitic fringes, ambient light, that occur during the acquisition of fringe data are unavoidable, being especially crucial in the interferometric set-ups. Error sources in the measurement system as the digitization error, low sampling rate due to insufficient resolution of the camera, nonlinearity error, electronic noise, thermal or shot noise, imaging error of the projector and the camera, the background noise, the calibration errors, optical system aberrations, beam power fluctuations and nonuniformity, frequency or temporal instability of the illuminating source, spurious reflections, and defects of optical elements, low precision of the digital-data processing hardware etc. occur in nearly all optical profilometric measurement systems leading to random variations of the background and fringe visibility. Measurement accuracy can be improved by taking special measures, e.g. by using a high-resolution SLM to reduce the digitization error of the projector and by defocusing the projected FPs or by selecting a CCD camera with a higher data depth (10 or 12 bits versus 8 bits). To reduce the errors due to calibration, a coordinate measuring machine can be used to provide the reference coordinates and to build an error compensating map [37]. Speckle noise affects the systems with coherent light sources [38, 39]. A special emphasis should be put on systematic and random error sources, $N_{ph}(\vec{r}, t)$, that influence the measured phase. Such error sources as miscalibration of the phase-shifting device or non-parallel illumination which causes non-equal spacing in the projected pattern along the object introduce a non-linear phase component. Methodological error sources such as shadowing, discontinuous surface structure, low surface reflectivity, or saturation of image-recording system, would produce unreliable phase data.

Accuracy of the measurement depends on the algorithm used for phase retrieval. For the local (pointwise) methods, the calculated output at a given point is affected by the values registered successively at this point or at neighbouring points whereas in global methods all image points affect the calculated value at a single point. A theoretical comparison of three phase demodulation methods in PMP in the presence of a white Gaussian noise is made in [40].

## 2 Phase Retrieval Methods

### 2.1 Phase-shifting Method

#### 2.1.1 General Description

A typical temporal analysis method is the phase-shifting (PS) algorithm in which, the phase value at each pixel on a data frame is computed from a series of recorded FPs that have undergone a phase shift described by a function $\phi(\vec{r}, t)$. If the reference phase $\phi_i, i = 1, 2, \ldots, M$ is kept constant during the capture time and is changed by steps between two subsequent FPs, the method is called phase stepping or phase shifting profilometry (PSP). In this case, to determine the values of $I_B(\vec{r})$, $I_V(\vec{r})$ and $\varphi(\vec{r})$ at each point, at least three FPs ($N = 3$) are required. In phase integration modification of the method, the reference phase is changed linearly in time during the measurement [41].

The PSP is well accepted in many applications due to its well-known advantages as high measurement accuracy, rapid acquisition, good performance at low contrast and intensity variations across the FP, and possibility for determination of the sign of the wave front. The PSP can ensure accuracy better than 1/100th of the wavelength in determination of surface profiles [42]. As in all profilometric measurements PSP operates either in a comparative mode with a reference surface or in an absolute mode

Usually, in PSP, phase evaluation relies on sinusoidal pattern projection

$$I(\vec{r},t) = I_0(\vec{r},t) + I_V(\vec{r},t)\cos[\varphi(\vec{r},t) + \phi(\vec{r},t)] \tag{4}$$

Violation of the assumption $f[\ldots] = \cos(\ldots)$ causes systematic errors in the evaluated phase distribution. Two approaches are broadly used in the phase-shifting, one based on equal phase steps – typically multiples of $\pi/2$ – and the other based on arbitrary phase steps. These two approaches are usually referred to as a conventional and a generalized PSP [43, 44]. A modification of the method with two successive frames shifted at known phase steps and one frame shifted at unknown phase step is proposed in [45]. All these phase-shifting algorithms can also be called digital heterodyning [46]. The most general approach for phase retrieval in the PSP with $M$ FPs shifted at known phase-steps is the least squares technique [47, 48]. Under the assumption that the background intensity and visibility have only pixel-to-pixel (inter-frame) variation, in the digitized FPs

$$I_{ij}^m = B_{ij}^m + V_{ij}^m \cos(\varphi_{ij} + \phi_m), m = 1, 2 \ldots M \tag{5}$$

where $B_{ij} = I_B(i\Delta_x, j\Delta_y)$ and $V_{ij} = I_V(i\Delta_x, j\Delta_y)$, $i = 1, 2, \ldots, N_y$, $j = 1, 2, \ldots, N_x$, we have

$$B_{ij}^1 = B_{ij}^2 = \ldots = B_{ij}^M = B_{ij} \text{ and } V_{ij}^1 = V_{ij}^2 = \ldots = V_{ij}^M = V_{ij} \tag{6}$$

Assuming also that the phase steps are known, the object phase is obtained from minimization of the least-square error between the experimental $\hat{I}_{ij}^m$ and the calculated intensity distribution

$$S_{ij} = \sum_{m=1}^{M} (\hat{I}_{ij}^m - I_{ij}^m)^2 = \sum_{m=1}^{M} (B_{ij} + a_{ij}\cos\phi_m + b_{ij}\sin\phi_m - \hat{I}_{ij}^m)^2 \tag{7}$$

The unknown quantities $a_{ij} = V_{ij}\cos\varphi_{ij}$ and $b_{ij} = -V_{ij}\sin\varphi_{ij}$ are found as the least squares solution of the Equation

$$\hat{\Omega}_{ij} = \begin{vmatrix} B_{ij} \\ a_{ij} \\ b_{ij} \end{vmatrix} = \hat{\Xi}_{ij}^{-1}\hat{\Upsilon}_{ij} \tag{8}$$

where $$\Xi_{ij} = \begin{vmatrix} M & \sum\limits_{m=1}^{M} \cos \phi_m & \sum\limits_{m=1}^{M} \sin \phi_m \\ \sum\limits_{m=1}^{M} \cos \phi_m & \sum\limits_{m=1}^{M} \cos^2 \phi_m & \sum\limits_{m=1}^{M} (\cos \phi_m) \sin \phi_m \\ \sum\limits_{m=1}^{M} \sin \phi_m & \sum\limits_{m=1}^{M} (\cos \phi_m) \sin \phi_m & \sum\limits_{m=1}^{M} \sin^2 \phi_m \end{vmatrix} \text{ and}$$

$$\hat{\Upsilon}_{ij} = \begin{vmatrix} \sum\limits_{m=1}^{M} I_{ij}^{m} \\ \sum\limits_{m=1}^{M} I_{ij}^{m} \cos \phi_m \\ \sum\limits_{m=1}^{M} I_{ij}^{m} \sin \phi_m \end{vmatrix}$$

The phase estimate is obtained in each pixel as

$$\hat{\varphi}_{ij} = \tan^{-1}(-b_{ij}/a_{ij}) \tag{9}$$

In the case of the so called synchronous detection the the $M$ FPs are equally spaced over one fringe period, $\phi_m = 2\pi m/M$, and the matrix $\Xi_{ij}$ becomes diagonal. More general approach is to take $M$ equally shifted FPs and to determine the phase from

$$\varphi(x, y) = \tan^{-1} \frac{\sum\limits_{m=1}^{M} b_m I_m(x, y)}{\sum\limits_{m=1}^{M} a_m I_m(x, y)} \tag{10}$$

The number of frames or "buckets" usually gives the name of the algorithm. Popular algorithms are the 3-frame algorithm with a step of 120° or 90° as well as the 4-frame algorithm and 5-frame algorithm with a step of 90°:

$$\hat{\varphi} = \arctan \frac{I_4 - I_2}{I_1 - I_3}, \hat{\varphi} = \arctan \frac{2(I_4 - I_2)}{I_1 - 2I_3 + I_5}, \alpha_i = (i - 1)\frac{\pi}{2} \tag{11}$$

### 2.1.2 Accuracy of the Measurement

The choice of the number of frames depends on the desired speed of the algorithm, sensitivity to phase-step errors and harmonic content of the function $f[\ldots]$, and accuracy of the phase estimation. The errors in the phase-step, $\phi(\vec{r}, t)$, and a nonsinusoidal waveform are the most common sources of systematic errors in the PSP [46, 49]. A nonsinusoidal signal may be caused by the non-linear response of the detector [46].

The phase shift between two consecutive images can be created using different means depending on the experimental realization of the profilometric system. Different phase-shifting devices are often subject to nonlinearity and may not ensure good repeatability. Miscalibration of phase shifters may be the most significant source of error [50]. In fringe-projection applications precise linear translation stages are used [51]. In interferometric systems a phase shifter usually is a mirror mounted on a piezoelectric transducer (PZT). In such systems non-stability of the driving voltage, nonlinearity, temperature linear drift and hysteresis of the PZT device and the tilt of the mirror affect the accuracy of the measurement. In the scheme presented in Fig. 3, a special feedback is introduced to keep constant the value of the phase-step. For large-scale objects it is more convenient to create a phase shift by slightly changing the wavelength of the light source. A phase-shifting system with a laser diode (LD) source has been proposed in [52] and [53], in which the phase shift is created by a change of the injection current of the LD in an unbalanced interferometer. The phase shift can be introduced by digitally controlling the SLM that is used for generation of fringes. As an example, an electrically addressed SLM (EA-SLM) is used to display a grating pattern in [42]. In [54] a DMD microscopic system is designed in which the three colour channels in the DMD projector are programmed to yield intensity profiles with $2\pi/3$ phase shift. Using the colour channel switching characteristic and removing the colour filter, the authors succeed to project grey-scale fringes and by proper synchronization between the CCD camera and the DMD projection to perform one 3D measurement within 10 ms.

A comprehensive overview of the overall error budget of the phase-shifting measurement is made in [55, 56]. The analysis in [57] divides the error sources in the PSP into three groups. The first group comprises systematic errors with a sinusoidal dependence on the measured phase as the phase-step errors and the detector non-linearities. The second group includes random error sources that may also cause sinusoidal $\varphi$-dependence of the measured phase error. Such sources are the instability of the light source, random reference phase fluctuations, and mechanical vibrations. The third group of errors consists of random errors which are not correlated to the measured phase as different noises that introduce random variation across the FP. Such noises are the detector output and quantization noise of the measured intensity.

According to [57], the systematic phase-step error $\delta\phi_i = \phi_i - \left\langle \hat{\phi}_i \right\rangle$, $i = 1, 2 \ldots M$, given by the difference between the theoretical phase step, $\phi_i$, for the $i$-th frame and the mean value of the phase step that is actually introduced by the phase-shifter, $\left\langle \hat{\phi}_i \right\rangle$, may be presented as a series $\delta\phi_i = \varepsilon_1\phi_i + \varepsilon_2\phi_i^2 + \varepsilon_3\phi_i^3 + \ldots$, with coefficients $\varepsilon_1$, $\varepsilon_2$, $\varepsilon_3, \ldots$ that depend on the phase shifter. The error analysis in [57] has indicated the linear and the quadratic phase step deviations as one of the main error sources degrading the phase measurement accuracy. If only the linear term is kept in $\delta\phi_i$, the error induced in $\varphi$ in all points of the FP for most of the PS algorithms is given by [57]:

$$\delta\varphi = \sum_{i=1}^{M} \left( \frac{\partial\varphi}{\partial I_i} \right) \left( \frac{\partial I_i}{\partial\phi_i} \right) \delta\phi_i \qquad (12)$$

The linear approximation (15) leads to dependence of the systematic error, $\delta\varphi$, on $\cos 2\varphi$ and $\sin 2\varphi$ [24, 58, 59, 60]. In fact, as it is shown in [57], the quadratic and cubic terms in (12) also lead to $\cos 2\varphi$ dependence of the systematic error. Influence of miscalibration and non-linearity of the phase-shifter for different phase-stepping algorithms is studied in [61].

The other frequently addressed systematic error is the non-linearity caused by the detector. To study its effect on the measured phase, [57] uses a polynomial description of intensity error, $\delta I_i = \left\langle \hat{I}_i \right\rangle - I_i = \alpha_1 I_i^2 + \alpha_2 I_i^3 + \alpha_3 I_i^4 + \ldots$, where $\alpha_1$, $\alpha_2$, $\alpha_3$ are constants. The detector non-linearity introduces higher harmonics in the recorded FP. Calculations and simulation made by different authors show that a linear approximation in $\delta I_i$ leads to dependence of the phase systematic error, $\delta\varphi$, on $\cos(M\varphi)$ e.g. for the four-step algorithm $\delta\varphi$ depends on $\cos(4\varphi)$.

Important source of intensity error is the quantization error in video cameras and frame grabbers used for data acquisition. By rounding or truncating values in the analog-to-digital conversion the quantization changes the real intensity values in the FP and causes an error in the phase estimate which depends on the number of intensity levels. Quantization is a non-linear operation procedure. First quantization error analysis in PSP is made in the thesis of Koliopoulus [62] and further developed by Brophy in [63]. Brophy [63] studies how the frame-to-frame correlations of intensity error influence the phase error. In the absence of frame-to-frame correlation the phase variance $\left\langle \delta\varphi^2 \right\rangle$ decreases as $1/M$. Brophy assumes in the analysis that the intensity quantization error expressed in grey levels is uniformly distributed in the interval $[-0.5, 0.5]$. This source of error does not exclude frame-to-frame correlation. As a result, $\left\langle \delta\varphi^2 \right\rangle$ may increase with the number of frames. Brophy obtains for a $Q$-level quantization the formula $\left\langle \delta\varphi^2 \right\rangle^{1/2} = 1/(\sqrt{3}Q)$. Specific algorithms could be designed in this case to decrease the phase variance. By introducing a characteristic polynomial method Zhao and Surrel [64, 65] succeed to avoid necessity to determine the inter-frame correlation of intensities in calculation of the phase variance. For the purpose, the phase in (10) can be taken as an argument of a linear combination

$$S(\varphi) = \sum_{m=1}^{M} c_m I_m = \frac{1}{2} I_V P(\varsigma) \exp(j\varphi) \tag{13}$$

in which the characteristic polynomial is defined by

$$P(\varsigma) = \sum_{m=1}^{M} c_m \varsigma^m \tag{14}$$

where $\varsigma = \exp(j\phi)$, $c_m = a_m + jb_m$. Surrel [66] shows that error-compensating behaviour of any phase-shifting algorithm can be determined by analyzing location and multiplicity of the roots of $P(\varsigma)$. This approach permits to find the sensitivity of the phase-shifting algorithms also to the harmonic content in the FP [66] and to obtain a simplified expression for the phase quantization error. It has been obtained that for an 8-bit or more quantization, this error is negligible for noiseless FPs, if the intensity is spread over the whole dynamic range of the detection system. The analysis and simulations made in [67] show that in the most common CCD cameras a nominal 6-bit range is used from the available 8-bit range which leads to a phase error of the order of 0.178 radians. The accuracy is increased by a factor of four if a 12-bit camera is used [67]. Algorithms with specific phase steps to minimize the errors from miscalibration and nonsinusoidal waveforms have been derived using the characteristic polynomial. It is obtained that a $(j+3)$-frame algorithm eliminates the effects of linear phase-shift miscalibration and harmonic components of the signal up to the $j$-th order.

Vibration as a source of error is essential in the interferometric set-ups. For example, testing of flat surfaces needs a very high accuracy of 0.01μm. Vibration induces blurring and random phase errors during acquisition of the successive frames in the temporal PS. For this reason interferometric implementation of the temporal PSP is appropriate whenever the atmospheric turbulence and mechanical conditions of the interferometer remain constant during the time required for obtaining the interferograms [31]. Analysis made in [68] shows that low frequency vibrations may cause considerable phase error whereas high frequency vibration leads to a reduced modulation depth [68]. In [68] a $(2+1)$ algorithm is proposed in which two interferograms, separated by a quarterwave step, are required to calculate the phase. A third normalizing interferogram, averaged over two phases that differ at 180°, makes possible to evaluate the background intensity. A thorough analysis of the vibration degrading effect is made in [69, 70]. Applying a Fourier analysis, an analytical description of the influence of small amplitude vibrations on the recorded intensity is obtained and the relationship between the Fourier spectrum of the phase error and the vibration noise spectrum is found by introduction of the phase-error transfer function which gives the sensitivity of the PS measurement to different noise frequency components. It is shown that immunity to vibration noise increases for the algorithms with higher number of recorded patterns. A max-min scanning method for phase determination is described in [71] and it is shown in [50] that it has a good noise tolerance to small amplitude low-frequency and high frequency noise.

Lower accuracy of phase demodulation and phase unwrapping should be expected in the image zones with low fringe modulation or contrast, e.g. in areas with low reflectivity. Fringe contrast is important characteristic for finding of an optimal unwrapping path and for optimal processing of phase data such as filtering, improving visualization, and masking [72]. However, using of high fringe contrast as a quality criterion of a good data is not always reliable because this feature of the FPs is insensitive to such surface structure changes as steps. In the areas with steps which do not cast shadow the fringe contrast is high but phase data are unreliable. Evaluation of the fringe contrast from several successively recorded images is inapplicable for real-time measurement. In [73] the fringe contrast and quality of the phase data are evaluated from a single FP by a least-squares approach.

It is rather complicated to perform *in situ* monitoring of the phase step, e.g. by incorporating additional interferometric arms. The more preferable approach is the so-called self-calibration of the phase steps [74] which makes use of the redundancy of the FPs. Some of the developed self-calibrating algorithms are pointwise whereas others take into account the information contained by the whole FP. However, most of the developed self-calibration methods put restrictions on the number and quality of the FPs and on the performance of the phase shifters.

Over the years, different approaches for deriving error-compensating algorithms have been proposed [49, 75]. Hibino [49] divides the PS algorithms into three categories according to their ability to compensate systematic phase-step errors. The first group comprises algorithms without immunity to systematic phase-step error, e.g. the synchronous detection algorithm. The second group consists of the error-compensating algorithms able to eliminate linear or nonlinear phase-step errors. The third group of algorithms compensate for systematic phase-step errors in the presence of harmonic components of the signal. To justify the compensating properties of the proposed algorithms different approaches have been invented as averaging of successive samples [76], a Fourier description of the sampling functions [77], an analytical expansion of the phase error [57] etc.

Currently, the five-frame algorithm proposed by Schwider–Hariharan [78] becomes very popular. Hariharan et al. show that the error of the five-frame algorithm has a quadratic dependence on the phase step error. A new four interferogram method for compensating linear deviations from the phase step is developed in [79]. To increase the accuracy, algorithms based on more frames start to appear [76]. Algorithms derived in [80] based on seven or more camera frames prove to have low vulnerability to some phase-step errors and to low-frequency mechanical vibration. In [81] three new algorithms are built with $\pi/2$ phase steps based on the Surrel [82] six-frame algorithm with a $\pi/2$ step, and four modifications of the conventional four-frame algorithm with a phase step of $\pi/2$ are studied using a polynomial model for the phase-step error. The ability to compensate errors is analyzed by the Fourier spectra analysing method. The main conclusion of the analysis is that it is possible to improve performance of $\pi/2$ algorithms by appropriate averaging technique. A self-calibrating algorithm proposed in [83] relies on the assumption of constant arbitrary phase-steps between the consecutive FPs and quasi-uniform distribution of the measured phase taken modulo $2\pi$ in the range $(0, 2\pi)$ over the recorded FP. When the phase steps differ from the actual ones, the probability density distribution of the retrieved phase is no longer uniform and exhibits two maxima. Applying of an iterative fitting procedure to a histogram built for the retrieved phase permits to find the actual phase steps and to correct the demodulated phase. The algorithm is further improved in [84] where the visibility of fringes across the FP is assumed to be constant whereas the background is allowed to have only intraframe variations. The improved algorithm introduces a feedback to adjust the supposed phase shifts until the calculated visibility map becomes uniform. The merit of the algorithm is its operation at arbitrary phase steps, however at the expense of constant visibity requiriment.

A general approach to diminish or eliminate some error sources in PS interferometry is proposed in [85]. A model for $N_{ph}(\vec{r}, t)$ is built which takes in account the phase-step error and considers an interferomer with a spherical Fizeau cavity. A generic algorithm for elimination of the mechanical vibration during the measurement is also described. Reference [77] adopts Fourier-based analysis to determine suitable sampling functions for the design of a five-frame PS algorithm that is insensitive to background variation when a laser diode is used as a phase shifter. Criteria are defined to check algorithm vulnerability to the background change. In addition, the authors evaluate the influence of the linear phase-shift miscalibration and the quadratic non-linearity of the detector error. An accurate method for estimation of the phase step between consecutive FPs is proposed in [51] for the case of five frame algorithm with an unknown but constant phase step, which permits to calculate the phase step as a function of coordinates and to use the so called lattice-site representation of the phase angles. In this representation the distance of the corresponding lattice site to the origin depends on the phase step. In the ideal case all lattice sites that correspond to a given phase step but to different phases lie on a straight line passing through the origin of the coordinate system whose both axes represent the numerator and denominator in the equation for phase step calculation [78]. The error sources deform somehow shape and spread of both histogram and lattice-site representation patterns. Application of the latter to analysis of behaviour of four and five frame algorithms is made in [86]. It is proven that the lattice-site representation outperforms the histogram approach for detection of errors in the experimental data.

A phase shifter in an interferometric setup is vulnerable to both translational and tilt-shift errors during shifting, which results in a different phase-step value in every pixel of the same interferogram. An iterative algorithm that compensates both translational- and tilt-shift errors is developed in [87] which is based on the fact that the 2D phase distribution introduced by the phase-shifter is a plane. This plane can be determined by a first-order Taylor series expansion that makes possible to transform the nonlinear equations for defining the phase-shift plane into linear ones. By using an iterative procedure both errors can be minimized. A liquid-crystal SLM may produce nonlinear and spatially nonuniform phase shift [75].

### 2.1.3 Generalized Phase-shifting Technique

In the conventional phase-shifting algorithms the phase steps are known and uniformly spaced. In this case simple trigonometry permits derivation of explicit formulas for the object phase calculation. It is also assumed that the background and visibility of fringes have only pixel-to-pixel variation but remain constant from frame to frame. In the generalized PSP, which in recent years gains increasing popularity because of the advantage to use arbitrary phase steps, these steps are unknown and should be determined from the recorded FPs. It is a frequently solved task in the PSP, e.g. for calibration of the phase-shifter.

Determination of the phase-step between two consecutive interferograms is similar to the signal-frequency estimation, which has attracted a lot of attention in the signal-processing literature. However, it is more complicated due to the fact that the background intensity (the dc component) is involved in the processed signal [88]. Determination of the phase step is equivalent to the task of the phase-step calibration which, generally speaking, can be performed by using two approaches: fringe tracking or calculation of the phase-step from the recorded FPs [89]. In the fringe tracking the size of the phase step is obtained from the displacement of fringes following some characteristic features of the fringes, e.g. positions of their extrema after performing fringe skeletonizing to find the centers of dark or bright interference lines [79]. An extensive overview of algorithms for determination of unknown phase steps from the recorded FPs is made in [90]. Phase step determination in a perturbing environment is analyzed in [91]. Several methods as Fourier series method, iterative linear and non-linear least squares methods are compared on the basis of computer simulations which prove the reliability of all of them for the derivation of the phase step.

Historically, development of self-calibrating algorithms starts with the first phase-stepping algorithm proposed by Carré in 1966 [92]. The algorithm is designed to operate at an arbitrary phase step, $\phi$, which is determined during the processing under assumption of linear phase step errors. It requires four phase-shifted images $I_i = I_0 + I_V \cos[\varphi + (i - 1.5)\phi]$, $i = 0, \ldots, 3$ under assumption of the same background intensity, modulation, and phase step for all recorded images.The Carré algorithm accuracy is dependent on the phase step. Carré recommends the value of 110 degrees as most suitable. The accuracy of the algorithm has been studied both theoretically [57] and by computer simulations [55] for the phase step $\pi/2$. Computer simulations and experiments performed in [79] for the case of white additive noise and Fourier analysis made in [93] confirm the conclusion of Carré that highest accuracy is observed at 110 deg. In [94] search for the best step that minimize the error of the Carré algorithm is made by means of linear approximation of Tailor series expansion of the phase error. Linear approximation yields correct results only in the case of small error expansion coefficients. The obtained results also indicate $\phi = 110^\circ$ as the best choice but only when the random intensity fluctuations (additive noise) are to be minimized. This value is not recommendable for compensation of a phase step error or a systematic intensity error. The authors draw attention to the fact that the numerator in the Carré algorithm should be positive which is fulfilled only for perfect images without noise. A number of other algorithms with a fixed number of equal unknown phase steps have been recently proposed in [95, 96, 97]. Use of a fixed number of equal steps is certainly a weak point in the measurement practice. This explains the urge of the phase-shifting community to elaborate more sophisticated algorithms with randomly distributed arbitrary unknown phase steps.

Direct real time evaluation of a random phase step in the generalized PS profilometry without calibration of the phase-shifter is realized in [98] where the phase step is calculated using a Fourier transform of straight Fizeau fringes that are simultaneously generated in the same interferometric set-up. The necessity to have an additional optical set-up puts limitation on the method application. Evaluation of the phase steps by Lissajous figure technique is described in [99, 100]. The phase is determined by ellipse fitting based on Bookstein algorithm of a Lissajous figure obtained if two phase-shifted fringe profiles are plotted against each other. The algorithm, however, is sensitive to noise and easily affected by low modulation of the FP. Some improvement of the algorithm is proposed in [100] where the Lissajous figures and elliptic serial least-squares fitting are used to calculate the object phase distribution. The algorithm has both immunity to errors in $\phi$ and possibility for its automatic calibration.

Reduction of phase error caused by linear and quadratic deviations of the phase step by means of a self-calibrating algorithm is proposed in [59]. The estimates of the phase steps are derived from each FP, and the exact phase difference between the consecutive patterns is calculated. Numerical simulation proves the efficiency of the algorithm up to 10% linear and 1% quadratic phase deviations and by experiments with a Twyman–Green interferometer for gauge calibration. Phase-calibration algorithm for phase steps less than $\pi$ that uses only two normalized FPs is proposed in [101]. For the purpose, a region that concises a full fringe (region with the object phase variation of at least $2\pi$) is chosen. The phase step is retrieved by simple trigonometry. A method for evaluation of irregular and unknown phase steps is described in [102] based on introduction of the carrier frequency in the FPs. The phase steps are determined from the phases of the first-order maximum in the spectra of the recorded phase-shifted FPs in the Fourier domain. The Fourier analysis can be applied to a subregion of the FP with high quality of the fringes. This straightforward and simple method works well only in the case of FPs with narrow spectra. Algorithms that exploit a spatial carrier use a relatively small number of interferograms. Improvement of the Fourier transform method based on the whole-field data analysis is proposed in [103]. The phase-step is obtained by minimization of the total energy of the first-order spectrum of the difference of two consecutive FPs with one of them multiplied by a factor of $\exp(j\phi)$ where $\phi$ is equal to the estimated value of the phase step to be determined. Simulations and experiments prove that the algorithm is effective, robust against noise, and easy to implement. Based on quadrature filter approach, Marroquin et al. propose in [104] an iterative fitting technique that simultaneously yields the phase steps and the object phase, which is assumed to be smooth. In [89] a method is proposed that requires only two phase-stepped images. The phase step is estimated as an arccosine from the correlation coefficient of both images without requirement for constant visibility and background intensity. The method can show position-dependent phase-step differences, but it is strictly applicable only to areas with a linear phase change.

To overcome the errors induced in the phase step by different sources it is desirable to develop a pointwise algorithm that can compute the phase step and the object phase at each pixel [105]. The first attempt to deduce an algorithm with unknown phase steps using the least-squares approach belongs to Okada et al. [106]. Soon it is followed by several proposals of self-calibrating least-squares PS algorithms [45, 107, 108, 109]. The essence of the least-squares approach is to consider both phase steps and object phase as unknowns and to evaluate them by an iterative procedure. This approach is especially reliable for FPs without spatial carrier fringes presenting stable performance in the case of nonlinear and random errors in the phase step. The number of equations which can be constructed from $M$ FPs each consisting of $N_x \times N_y$ pixels is $3M \times N_x \times N_y$ whereas the number of unknowns is $3N_x \times N_y + M - 1$. This entails the requirement $3M \times N_x \times N_y \geq 3N_x \times N_y + M - 1$ to ensure the object phase retrieval. To have stable convergence the least-squares PS algorithms with unknown phase steps need comparatively uniformly spaced initial phase steps that are close to the actual ones. These algorithms usually are effective only at small phase-step errors and require long computational time. They are not able to handle completely random phase-steps. As a rule, these methods are either subject to significant computational burden or require at least five FPs for reliable estimation. The least-squares approach is accelerated in [109, 110] where a computationally extensive pixel-by-pixel calculation of the phase step estimate is replaced with a $2 \times 2$ matrix equation for $\cos\phi$ and $\sin\phi$. The phase step is determined iteratively as $\hat{\phi} = \tan^{-1}(\sin\phi/\cos\phi)$ until the difference between two consecutive phase step estimates falls down below a predetermined small value. The limitations of the least squares approach are overcome by an advanced iterative algorithm proposed in [111] and [112] which consists of the following consecutive steps:

i) Using a least-squares approach, the object phase is estimated in each pixel under assumption of known phase steps and intraframe (pixel-to-pixel) variations of the background intensity and visibility.
ii) Using the extracted phase distribution, the phase steps $\phi_n = \tan^{-1}(-d_n/c_n)$ are updated by minimization of the least-square error.

$$S_n = \sum_{i=1}^{N_x}\sum_{j=1}^{N_y}(\hat{I}_{ij}^n - I_{ij}^n)^2 = \sum_{i=1}^{N_x}\sum_{j=1}^{N_y}(B^n + c_n\cos\varphi_{ij} + d_n\sin\varphi_{ij} - \hat{I}_{ij}^n)^2 \quad (15)$$

under assumption of interframe (frame-to-frame) variations of the background intensity and visibility, $B_{ij}^n = B^n$ and $V_{ij}^n = V^n$, with $c_n = V^n\cos\phi_n$ and $d_n = -V^n\sin\phi_n$.

iii) If the pre-defined converging criteria are not fulfilled the steps i) and ii) are repeated.

An improved iterative least-squares algorithm is constructed in [108] which minimizes the dependence of differences between the recorded intensities and their recalculated values with respect of the phase step errors. An iterative approach is considered in [113] where the phase steps are estimated by modelling of an interframe intensity correlation matrix using the measured FPs. This makes the method faster, more accurate and less dependent on the quality of the FPs. The smallest eigenvalue of this matrix yields the random error of intensity measurement. As few as four FPs are required for phase-steps estimation. The developed iterative procedure is rather simplified in comparison with the methods that rely on pixel-to-pixel calculation. The accuracy of $2 \times 10^{-3}$ rad has been achieved. A pointwise iterative approach for the phase step determination based on linear predictive property and least squares minimization of a special unbiased error function is proposed in [88]. The algorithm works well only for a purely sinusoidal profile of the FP. Phase retrieval and simultaneous reconstruction of the object wave front in PS holographic interferometry with arbitrary unknown phase steps is proposed in [107]. Assuming uniform spatial distribution of the phase step over the recorded interferogram, the authors obtain the following relationship between consecutive interferograms

$$p_n = \left\langle \left| \frac{I_{n+1} - I_n}{4\sqrt{I_0 I_r}} \right| \right\rangle = \frac{2}{\pi} \sin \frac{\phi_{n+1} - \phi_n}{2} \tag{16}$$

where $I_0$ and $I_r$ are the intensities of the object and the reference waves. The parameter $p_n$ can be determined for all recorded interferograms which further permits to restore the complex amplitude of the object wave. The process is repeated iteratively until the difference $\phi_{n+1} - \phi_n$ becomes less than a small predetermined value. The algorithm is proved to work well for any number of patterns $M > 3$ by computer simulations. Extension of the algorithm is proposed in [114] for the case when only the intensity of the reference beam must be measured. The need of iterations, however, makes it unsuitable for real-time measurement as the authors recommend at least 20 iterations in 1 min to reach the desired high accuracy. To avoid iterations and the need of alternative estimation of the object phase and the phase step, Qian et.al. [115] propose to apply a windowed Fourier transform to a local area with carrier-like fringes in two consecutive FPs.

The objective of [43] is to develop a generalized PS interferometry with multiple PZTs in the optical configuration that operates under illumination with a spherical beam in the presence of higher harmonics and white Gaussian intensity noise. These goals are achieved by a super-resolution frequency estimation approach in which Z-transform is applied to the phase-shifted FPs, and their images in the Z-domain are multiplied by a polynomial called an annihilating filter. The zeros of this filter in the Z-domain should coincide with the frequencies in the fringes. Hence, the parametric estimation of the annihilating filter provides the desired information about the phase steps. Pixelwise estimation of arbitrary phase steps from an interference signal buried in noise in the presence of nonsinusoidal waveforms by rotational invariance is proposed in [105]. First, a positive semidefinite autocorrelation matrix is built from the *M* phase-shifted records at each pixel (*i, j*) which depends only on the step between the samples. The signal is separated from the noise by a canonical decomposition to positive definite Toeplitz matrices formed from the autocorrelation estimates. The phase steps are determined as frequency estimates from the eigen decomposition of the signal autocorrelation matrices. The exact number of harmonics in the signal is required. The method is extended to retrieve two distinct phase distributions in the presence of higher harmonics and arbitrary phase-steps introduced by multiple PZTs [116]. In [117] the problem of using two or more PZTs in the PS interferometry with arbitrary phase steps in the presence of random noise is solved by maximum-likelihood approach. The developed algorithm should allow for compensation of non-sinusoidal wavefront and for non-collimated illumination.

### 2.1.4 Phase Unwrapping

As it has been already mentioned, the presence of the inverse trigonometric function arctg in the PS algorithms introduces ambiguity in the measured phase distribution. The calculated phase is wrapped into the interval of $(-\pi; +\pi)$. The process of removing $2\pi$ crossovers (unwrapping) could simply be described as subtracting or adding $2\pi$ multiples to the wrapped phase data [118] that is equivalent to assign the fringe order at each point:

$$\varphi_{unw}(i,j) = \varphi_{wr}(i,j) + 2\pi k(i,j), \tag{17}$$

where $\varphi_{unw}(i,j)$ is the unwrapped phase at the pixel (*i, j*), $\varphi_{wr}(i,j)$ is the experimentally obtained wrapped phase at the same point, and *k(i, j)* is an integer, that counts $2\pi$ crossovers from a starting point with a known phase value to the point (*i, j*) along a continuous path. Therefore, the phase unwrapping problem is a problem of estimation of the correct value of *k(i, j)* in order to reconstruct the initial true signal [119].

The described unwrapping procedure performs well only in the case of a noise-free, correctly sampled FP, without abrupt phase changes due to object discontinuities [120]. The basic error sources that deteriorate the unwrapping process are i) speckle noise, ii) digitalization and electronic noise in the sampled intensity value, iii) areas of low or null fringe visibility, and iv) violation of the sampling theorem [44, 120, 121]. In addition, the phase unwrapping algorithms should distinguish between authentic phase discontinuities and those caused by object peculiarity, coalescence [122], shadowing or non-informative zones due to limited detector visibility range. Over the years a lot of research is aimed to develop different unwrapping techniques [123], which should find the middle ground between alleviation of the computational burden and reduction of influence of the phase ambiguities [124]. One of the major problems in the phase unwrapping is how to estimate the unreliable data that may disturb actual data restoration. The principal categorization of algorithms that attack the major error sources is proposed in [125, 126], where three basic classes are outlined:

i) **Global class**. In global class algorithms the solution is formulated in terms of minimization of a global function. The most popular phase unwrapping approaches [125, 127, 128, 129, 130, 131, 132] are based on solution of a unweighted or weighted least-squares problem [123, 133]. All the algorithms in this class are known to be robust but computationally intensive. The presence of noise and other fringe discontinuities, however, leads to corrupted results because of the generalized least square approach applied. To overcome this disadvantage, a time-consuming post-processing should be utilized [126].

ii) **Region class**. An essential feature of these algorithms is subdivision of wrapped data in regions. Each region is processed individually and on this basis larger regions are formed till all wrapped phase values are processed. This restricts the local errors only to the processed zone of the FP preventing their propagation into the other regions. There are two groups of region algorithms: 1) *Tile-based* and 2) *Region-based*. In tile-based approach [134, 135] the phase map is divided into grid of small tiles, unwrapped independently by line-by-line scanning techniques and after that the regions are joined together. However, this algorithm is not successful in processing of very noisy data. The region-based approach, proposed initially by Geldorf [136] and upgraded by other researchers [119, 128, 137, 138, 139, 140] relies on forming uniform regions of continuous phase. A comparison of a pixel to its neighbour is performed. If the phase difference is within a predefined value, then the pixel and its neighbour are attached to the same region; otherwise, they belong to different regions. After that the regions are shifted with respect to each other to eliminate the phase discontinuities.

iii) **Path following class**, in which data unwrapping is performed using an integration path. The class of path-following algorithms can be subclassified into three groups: 1) *Path-dependant methods*; 2) *Residue-compensation methods* and 3) *Quality guided path methods*. The first group is characterized with phase integration on preliminary defined path (i.e. linear scanning, spiral scanning, multiple scan direction [141]); the simplest example of this type is proposed by Schafer and Oppenheim's [142]. Despite of their benefit to be low-time consuming, these methods are not reliable at the presence of noise and other error sources due to the fixed integration path. The residue-compensation methods rely on finding the nearest residues (defined as unreliable phase data) and connect them in pairs of opposite polarity by a branch-cut [143]. Uncompensated residues could be connected also to the image border pixels. The unwrapped procedure is realized without crossing any branch-cut placed, limiting the possible integration paths. Other similar approaches [144, 145] are also based on branch-cuts unwrapping strategy. These methods produce fast results, but an inappropriately placed branch-cut could lead to isolation of some phase zones and discontinuous phase reconstruction. Quality-guided path following algorithms initially unwrap the most reliable data, while the lowest reliable data are passed up in order to avoid error spreading. The choice of integration path depends on pixels quality in the meaning of quality map, first proposed by Bone [146], who uses a second difference as a criterion for data reliability, setting up a threshold, and the all phase data with calculated second derivatives under it are unwrapped in any order. The method is improved [147, 148] by introducing an adaptive threshold with increasing threshold value whose implementation allows all data to be processed. However, when reliable quality map is not presented, the method fails in phase restoration. The accuracy of the produced quality map assures successful performance of the method [149] with different type of phase quality estimators, such as correlation coefficients [123, 150] phase derivatives variance [151, 152] or fringe modulation [77, 153]. For illustration of some of the discussed phase unwrapping methods we processed the wrapped phase map (Fig. 8) of two real objects – plane and complicated relief surface, experimentally produced by two-spacing projection PS interferometry [5]. The results are shown in Fig. 9.

*Goldstein* algorithm (Fig. 9a) identifies the low quality phase values, but does not create correct branch-cuts. The main advantage of this algorithm is minimization of the branch-cut length, thus allowing for fast data processing. However, this approach is not efficient in the case of phase maps with sharp discontinuities. The same bad result is observed when implementing

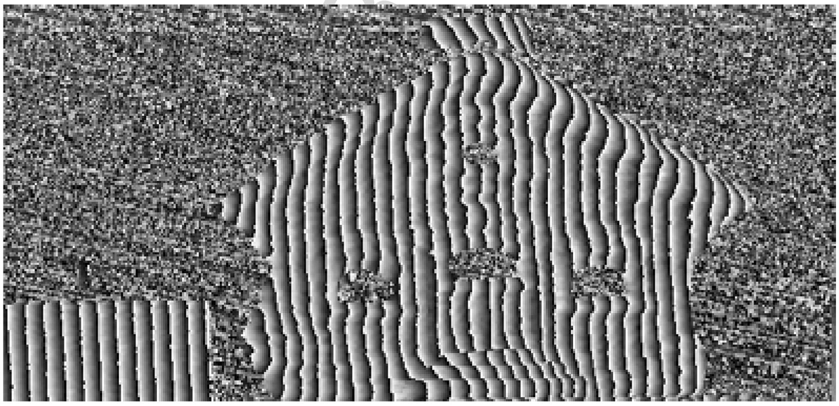

**Fig. 8.** Wrapped phase map of a test (*left*) and a real (*right*) object

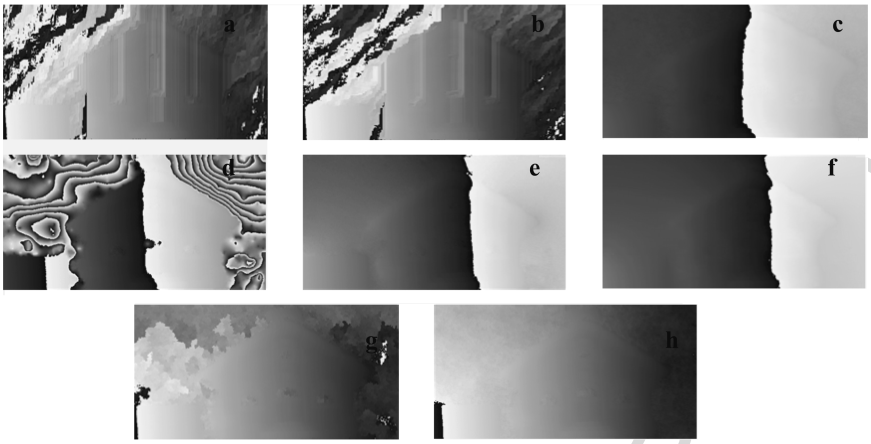

**Fig. 9.** Unwrapped phase map for **a**) Goldstein method, **b**) mask-cut method, **c**) minimum $L^p$ – norm method, **d**) weighted multigrid method, **e**) conjugated gradient method, **f**) least-squares method, **g**) quality-guided path following method and **h**) Flynn method

Mask-cut algorithm (Fig. 9b) that upgrades the *Goldstein* method with introducing quality map to guide the branch-cut placement. In comparison with *Goldstein* method, the incorrect interpretation of phase data could be due to low accuracy of the quality map. The phase unwrapping using all four minimum norm methods fails (Fig. 9) in the case of complex phase map with low quality noisy regions and discontinuities. A possible reason is the absence of a good quality map. Increasing the number of iterations improves the quality of the demodulated phase but at the expense of longer computational time. Quality-guided path following method (Fig. 9g) successfully demodulates the processed phase map. The regions with bad quality values (due to noise and shadowing) are recognized due to implementation of quality map that guides the integrating path. The algorithm is fast and successfully presents the small details that make it suitable for processing of complex phase maps. *Flynn* method (Fig. 9h) also provides phase reconstruction by effectively identifying phase discontinuities as a result of its main benefit – to perform well without an accurate phase map. However, in comparison with Quality-guided path following method it has poorer presentation of details and flat surfaces and is more time consuming.

Involvement of arctan function in phase retrieval is an obstacle in achieving the two main goals of the PMP: high measurement accuracy and unambiguous full-filed measurement. Among the solutions of this problem there is the so-called temporal-phase unwrapping method [154, 155] which makes pixel-by-pixel unwrapping along the time coordinate by projection of a proper number of FPs at different frequencies. Thus propagation of the unwrapping error to the neighbouring pixels is avoided. The first projected pattern in the temporal sequence consists of a single fringe, and the phase changes from $-\pi$ to $+\pi$ across the field of view [156]. If the number of fringes increases at subsequent time values as $n = 2, 3 \ldots, N$, so the phase range increases as $(-n\pi, n\pi)$. For each *n, M* phase-shifted FPs are recorded. Therefore, the measured intensity depends on pixel coordinates, current number of fringes and number of the phase-shifted patterns. Analysis made in [44, 157] shows that the error in depth determination scales as $N^{-1}$ to $N^{-3/2}$. Obviously, temporal unwrapping is suitable to applications when the goal is to derive the phase difference. Modifications of the original scheme have been tested aiming to reduction of the used FPs. As an example, in [158] two sinusoidal gratings with different spacings are used for fringe projection. The grating with higher spatial frequency ensures the sensitivity of the measurement while the coarse grating creates a reference pattern in the phase unwrapping procedure. Projection of tilted grids for determination of the absolute coordinates is proposed in [159]. In [20] a SLM is used to project fringes for surface contouring with a time-varying spatial frequency, e.g. linearly increasing, and by temporal unwrapping the 3D coordinates are restored pixel by pixel. In [157] an exponential increase of the spatial frequency of fringes is used which enhances the unwrapping reliability and reduces the time for data acquisition and phase demodulation. In [160] temporal unwrapping is combined with digital holography. The method requires a time-coded projection which is a serious limitation. This limitation is overcome in [161], where the authors propose projection of a single FP obtained by merging two sinusoidal gratings with two different spacings $1/f_1 > 1/f_2$. The following FP is recorded:

$$\begin{aligned} I(x,y) &= I_B(x,y) + I_1(x,y) + I_2(x,y) = \\ &= I_B(x,y) + I_V^1(x,y)\cos[2\pi f_1 x + \varphi(x,y)] \\ &\quad + I_V^2(x,y)\cos[2\pi f_2 x + \varphi(x,y)] \end{aligned} \tag{18}$$

Two phase maps $\varphi_{1,2}(x,y)$ are derived from the components $I_{1,2}(x,y)$ that are isolated from the registered FP and multiplied by the signals $\cos(2\pi f_{1,2}x)$ and $\sin(2\pi f_{1,2}x)$ respectively. Due to the relation, $f_1\varphi_2(x,y) = f_2\varphi_1(x,y)$, higher sensitivity is achieved, at least within non-ambiguity interval of $\varphi_1(x,y)$. In [162] two Ronchi gratings of slightly different spacings are used for fringe generation. The small difference in spacings is a ground to conclude that at a given point *(x, y)* both $\varphi_{1,2}(x,y)$ and their difference are monotone functions of the object depth or height, *h*. This allows for coarse and fine estimation of *h*. A multifrequency spatial-carrier fringe projection system is proposed in [22]. The system is based on two-wavelength lateral shearing interferometry and varies the spatial-carrier frequency of the fringes either by changing the wavelength of the laser light or by slight defocusing. In [163] a white-light Michelson interferometer produces the varying pitch gratings of different wavelengths which are captured and separated by a colour video camera using red, green and blue channels. Parallel and absolute measurement of surface profile with a wavelength scanning interferometry is given in [32]. By using Michelson and Fizeau interferometer the authors report measuring objects with steps and narrow dips. The multiwavelength contouring for objects with steps and discontinuities is further improved in [164] by an optimizing procedure for determination of the minimum number of wavelengths that are necessary for phase demodulation. A pair of coarse and fine phase diffraction gratings is used for simultaneous illumination at two angles of an object in a PS interferometric system for flatness testing. The synthetic wavelength is 12.5 mm, and a height resolution of 0.01 mm is achieved.

A PS approach without phase unwrapping is described in [165]. It includes calculation of the partial derivatives to build a 2D map of the phase gradient and numerical integration to find the phase map. The method proves to be less sensitive to phase step errors and does not depend on the spatial nonuniformity of the illuminating beam and on the shape of the FP boundary. Projection of a periodic sawtoothlike light structure and the PS approach are combined in [166]. Projection of such a pattern is simpler in comparison with the sinusoidal profile. The phase demodulation procedures are described for right-angle triangle teeth and isosceles triangle teeth. The method requires uniform reflectivity of the surface. The recommendable $\phi$ is half the period of the projected pattern.

## 2.2 Absolute Coordinates Determination

Projecting of two FPs with different spatial frequencies can be used for measurement of 3D coordinates as is proposed in [167]. The method is based on the generation in the $(x', y', 0)$ plane of fringes with spacings $d_1$ and $d_2$ that are parallel to the $y'$ axis (Fig. 10). The $y$ and $y'$ axes are perpendicular to the plane of the drawing. The phase of the projected fringes is determined as $\varphi'_i = 2\pi x'/d_i, i = 1, 2$. The phase is reconstructed in the $xyz$ coordinate

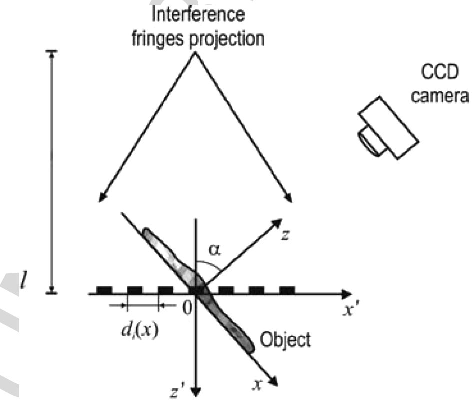

**Fig. 10.** Basic set-up for absolute coordinates determination

system, with the $z$ axis oriented parallelly to the optical axis of the CCD camera. Angle $\alpha$ is the inclination angle of the illumination axis $z'$ with respect to the observation axis $z$. The phase maps are determined by the five-step algorithm for each of the spacings. The smaller of the spacings is chosen to allow ten pixels per fringe period. The phase $\Delta\varphi_i(x, y)$ can be represented in the $xyz$ coordinate system as

$$\Delta\varphi_i(x, y) = \varphi_i(x, y) - \varphi_0 = \frac{2\pi}{d_i} \cdot \frac{lx \cos\alpha + lz(x, y) \sin\alpha}{l - z(x, y) \cos\alpha + x \sin\alpha} - \varphi_0, \tag{19}$$

where $i = 1, 2$; $z(x, y)$ is the relief of the object at point $(x,\ y)$, $l$ is the distance from the object to the exit pupil of the illumination objective, and $\varphi_0$ is an unknown calibration constant. Subtracting the obtained phase distributions and assuming, $\Delta\varphi_2(x, y) - \Delta\varphi_1(x, y) = 2\pi n_{x,y}$, we obtain the expression for the coordinate $z$ in the form

$$z(x, y) = \frac{n_{x,y}(1 + x \sin\alpha) + \chi lx \cos\alpha}{n_{x,y} \cos\alpha - \chi l \sin\alpha}, \quad \chi = \frac{d_2 - d_1}{d_1 d_2} \tag{20}$$

The vertical interference fringes, generated with a collimated laser light and a Michelson's interferometer (one mirror is mounted on a phase-stepping device) are projected on the plane $(x', y',0)$. Different spacings of interference patterns are used for successive illumination of the object surface ($d_1 = 1\,\text{mm}$, $d_2 = 2$ and $6\,\text{mm}$). The angle $\alpha$ of the object illumination is 30 deg. The wrapped phase maps at different spacings of the projected FPs are presented in Fig. 11. Figure 12 gives the 3D reconstruction of the object. The method's sensitivity mainly depends on the accuracy with which the phase difference is measured, i.e., on the accuracy of $n_{x,y}$ estimation. The influence of inaccuracy in determining $l$ and $\alpha$ can be neglected. The measurement accuracy increases with the difference $(d_1 - d_2)$ and with the illumination angle $\alpha$ but is not uniform over the length of the object and decreases as its transverse size increases.

It is interesting to compare the obtained result to the two-wavelength holographic contouring of the same object, presented in [168, 169]. In reconstruction with a single wavelength of the two-wavelength recorded hologram

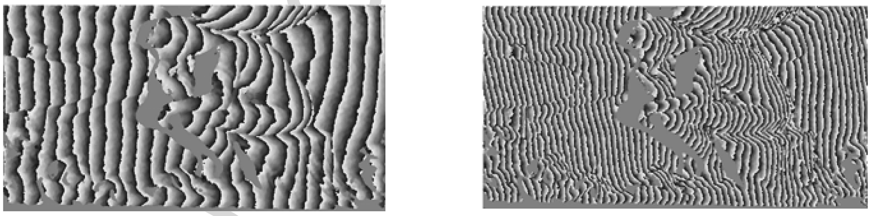

**Fig. 11.** Phase maps obtained for different spacings of the projected interference patterns after median filtration and low-quality zones detection; **left**) $d_1 = 1\,\text{mm}$, $d_2 = 2\,\text{mm}$; **right**) $d_1 = 1\,\text{mm}$, $d_2 = 6\,\text{mm}$

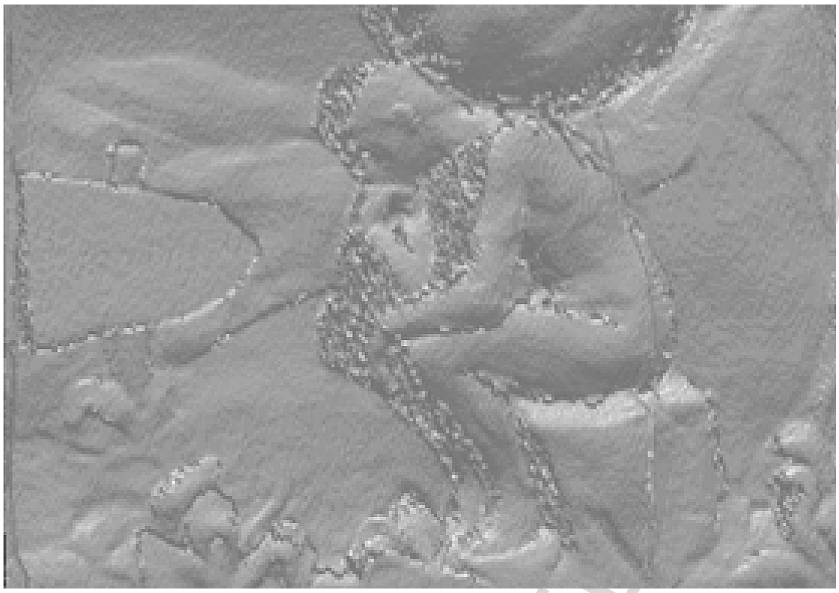

**Fig. 12.** Reconstructed 3D image from the difference phase map

the object's image is modulated as a result of interference of the two reconstructed images by sinusoidal contouring fringes in normal direction separated at distance Δz which depends on both recording wavelengths and the angle between the reference and the object beam (surface normal). A ten mW CW generating temperature stabilized diode laser, emitting two shifted at $\Delta\lambda \sim 0.08\,\text{nm}$ wavelengths in the red spectral region ($\sim 635\,\text{nm}$) is used for recording of a single exposure reflection (Denisyuk's type) hologram onto silver-halide light-sensitive material. The illumination angle is 30 deg. The image reconstructed in white light is shown in Fig. 13. The step between the contouring fringes is $\Delta z = 1.83\,\text{mm}$.

## 2.3 Fourier Transform Method

### 2.3.1 Basic Principle and Limitations

The most common and simple way for phase demodulation from a single FP is to use Fourier transform for analysis of the fringes. Almost three decades of intensive research and application make the Fourier transform based technique a well established method in holography, interferometry and fringe projection profilometry. In two works [170, 171] published within an year in 1982 and 1983 by Takeda and co-workers, it is shown that 1D version of the Fourier transform method can be applied both to interferometry [170] and PPP [171]. Soon after that, the method gains popularity under the name of Fourier fringe analysis (FFA) [172, 173, 174, 175, 176]. For the 3D shape measurement the method

**Fig. 13.** Reconstructed image in white light illumination of reflection hologram

becomes known as Fourier transform profilometry (FTP). The FTP surpasses in sensitivity and avoids all the drawbacks exhibited by the previously existing conventional moiré technique used for 3D shape measurement as the need to assign the fringe order, poor resolution, and the incapability of discerning concave or convex surfaces [177, 178]. The computer-aided FFA is capable to register a shape variation that is much less than one contour fringe in moiré topography [171]. Some years later, the 1D Fourier transform method is extended to process 2D patterns – firstly by applying 1D transform to carrier fringes parallel to one of the coordinate axes [179, 180] and further by generalization of the method to two dimensions [175]. Actually, as has been reported in [174], the algorithm proposed in [175] has been in use since 1976 for processing of stellar interferograms. The ability of FFA for fully automatic distinction between a depression and an elevation in the object shape put the ground for automated processing in the FTP [171].

The main idea of the FFA is to add a linearily varying phase into the FP, i.e. to use in (1) $\phi(\vec{r}) = 2\pi\vec{f_0} \cdot \vec{r}$, which can be done e.g. by tilting one of the mirrors in the interferometric setup or by using a diffraction grating for fringe projection. Obviously, the introduction of the carrier frequency $\vec{f_0} = (f_{0x}, f_{oy})$ is equivalent to adding a plane in the phase space, as it is shown in Fig. 14. The expression for the recorded intensity becomes:

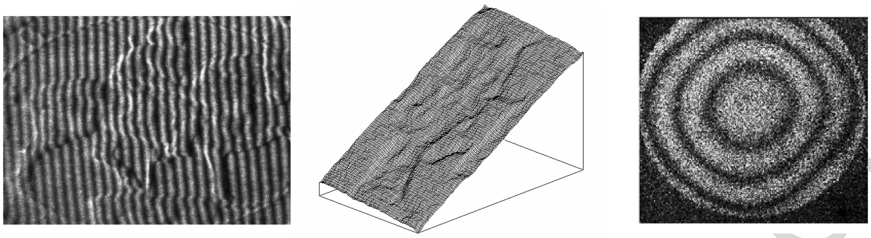

**Fig. 14. Left**: pattern with open fringes; **middle**: 3D presentation of the phase map without carrier removal; **right**: pattern with closed fringes

$$\begin{aligned} I(\vec{r}) &= I_B(\vec{r}) + I_V(\vec{r}) f[\varphi(\vec{r}) + 2\pi\vec{f}\cdot\vec{r}_0] \\ &= I_B(\vec{r}) + I_V(\vec{r}) \sum_{p=1}^{\infty} A_p \cos\left\{p\left[\varphi(\vec{r}) + 2\pi\vec{f}\cdot\vec{r}_0\right]\right\} \end{aligned} \tag{21}$$

where the dependence on time variable, $t$, is omitted since we consider the case of phase retrieval from a single FP. The purpose of carrier frequency introduction is to create a FP with open fringes in which the phase change is monotonic (Fig. 14). The further processing of (21) is straightforward and includes the steps:

i) Fourier transform of the carrier frequency FP that is modulated by the object

$$D(\vec{f}) = D_B(\vec{f}) + \sum_{\substack{p=-\infty \\ p\neq 0}}^{\infty} D_p(\vec{f} - p\vec{f}_0) \tag{22}$$

with $D_p(\vec{f}) = F\left\{\frac{1}{2}I_V(\vec{r})A_p e^{jp\varphi(\vec{r})}\right\}$ and $D_B(f_x, f_y) = F\{I_B(x,y)\}$, where $F\{\ldots\}$ denotes Fourier transform and $\vec{f} = (f_x, f_y)$ is the spatial frequency;

ii) selection of the fundamental spectrum that corresponds to one of the two first diffraction orders, $D_1(\vec{f} - \vec{f}_0)$ or $D_1(\vec{f} + \vec{f}_0)$, by proper asymmetric bandpass filtering;

iii) removal of the carrier frequency $D_1(\vec{f} - \vec{f}_0) \rightarrow D_1(\vec{f})$;

iv) inverse Fourier transform back to the spatial domain $F^{-1}\{D_1(\vec{f})\}$;

v) extraction of the phase information from the resulting complex signal $\Psi(\vec{r}) = \frac{1}{2}I_V(\vec{r})A_1(\vec{r})e^{jp\varphi(\vec{r})}$ in the spatial domain, whose argument is the searched phase:

$$\varphi(\vec{r}) = \tan^{-1}\frac{\mathrm{Im}[\Psi(\vec{r})]}{\mathrm{Re}[\Psi(\vec{r})]} \tag{23}$$

As is seen, introduction of the carrier frequency separates in the Fourier domain both counterparts of the fundamental spectrum from each other and from the background intensity contribution concentrated around the zero-frequency (Fig. 15). Due to the global character of the Fourier transform, the

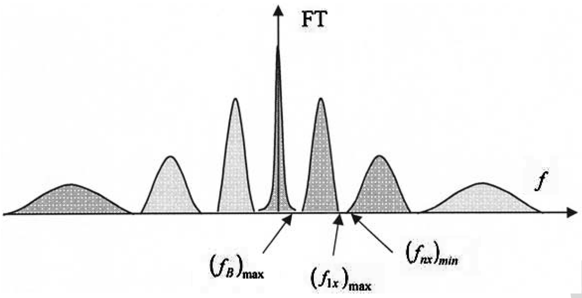

**Fig. 15.** Schematic of the Fourier fringe analysis

phase estimate calculated at an arbitrary pixel depends on the whole recorded FP. This means that any part of the pattern influences all other parts and vice versa. The successive steps of the FFA are illustrated in Fig. 16. Similar to the PS technique, the FFA returns a phase value modulo 2π and needs further unwrapping. As it can be seen from (23), the phase is restored without the influence of the terms $I_B(x, y)$ and $I_V(x, y)$. This means that the Fourier algorithm is not vulnerable to the noise sources that create $I_B(x, y)$ as e.g. stray light from the laboratory environment, unequal intensities in the two arms of interferometer or the dark signal from the imaging system, as well as to the noise contribution in $I_V(x, y)$ as e.g. nonuniform intensity distribution of the illuminating beam, optical noise or nonuniform response of the CCD [181].

In most cases, the higher harmonics content is ignored, and the recorded pattern with open fringes looks like [173]:

$$\begin{aligned} I(x, y) =& I_B(x, y) + \Psi(x, y)\exp[2\pi j(f_{0x}x + f_{0y}y)] \\ &+ \Psi^*(x, y)\exp[-2\pi j(f_{0x}x + f_{0y}y)] \end{aligned} \tag{24}$$

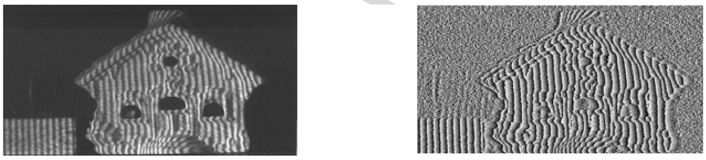

a) initial frame b) wrapped phase

c) Fourier spectrum d) 3D view of the unwrapped phase

**Fig. 16.** Single frame phase retrieval with FFA

The 2D Fourier transform of (24) can be written in the form:

$$D(f_x, f_y) = D_B(f_x, f_y) + D_1(f_x - f_{0x}, f_y - f_{0y}) + D_1^*(f_x + f_{0x}, f_y + f_{0y}) \quad (25)$$

where the asterisk represents the complex conjugate. If the background, the visibility and the phase vary slow in comparison to $(f_{0x}, f_{0y})$, the amplitude spectrum is a trimodal function with a broadened zero peak $D_B(f_x, f_y)$ and $D_1$ and $D_1^*$ placed symmetrically to the origin. In this case, the three parts of the spectrum in (25) can be well isolated from each other. A 2D bandpass filter centered at $(f_{0x}, f_{0y})$ extracts a single spectrum $D_1(f_x - f_{0x}, f_y - f_{0y})$ which is shifted to the origin in the frequency domain (Fig. 15). The amplitude of the zero-order spectrum at each point in the frequency domain exceeds at least twice the amplitudes of the first orders, which restricts the size of the filter window to remain, roughly speaking, less than halfway between zero- and first-order maxima. If after the filtering $D_1(f_x - f_{0x}, f_y - f_{0y})$ remains where it is, a tilt is introduced in the restored height distribution [182]. The inverse Fourier transform of $D_1(f_x, f_y)$ yields, at least theoretically, the complex signal, $\Psi(x, y)$.

The FTP uses optical geometries similar to those of projection moiré topography [171]. The most common and easy for implementation is the crossed-optical-axes geometry, like the one depicted in Fig. 1. For the measurement with a reference plane, the phase change is determined from $\Delta\phi(x, y) = \mathrm{Im}\{\log[\Psi(x, y)\Psi_r^*(x, y)]\}$ [183], where $\Psi_r^*(x, y)$ corresponds to the reference plane and is obtained after the inverse Fourier transform of the filtered positive or negative counterpart of the fundamental spectrum.

The necessary condition to avoid overlapping of the spectra in (37) if we assume without a loss of generality that the carrier fringes are parallel to the y axis, is given by [173]:

$$\left[f_{0x} + \frac{1}{2\pi}\frac{\partial\varphi(x, y)}{\partial x}\right]_{x,y\in S} > 0 \text{ or } \left[f_{0x} + \frac{1}{2\pi}\frac{\partial\varphi(x, y)}{\partial x}\right]_{x,y\in S} < 0 \quad (26)$$

The choice of the inequality depends on whether the positive or negative counterpart of first order spectrum has been filtered; here $S$ is the area occupied by the FP. This limitation on the phase variation and hence on the depth variation within the object under investigation is the main drawback of the FFA. It is obvious that the above condition is satisfied only for open fringes with monotonic phase behaviour which makes the FFA inapplicable to closed fringes.

In order to avoid aliasing, $(f_{1x})_{\max} \le (f_{nx})_{\min}$ for $n > 1$ and $(f_{1x})_{\min} \ge (f_B)_{\max}$ should be satisfied (Fig. 15), where $2\pi f_{nx} = n[2\pi f_{0x} + \partial\varphi(x, y)/\partial x]$ and $(f_B)_{\max}$ is the maximal frequency of the background spectrum. The above non-equalities entail

$$\left|\frac{\partial\phi(x, y)}{\partial x}\right| \le \frac{2\pi f_{0x}}{3} \text{ or } \left|\frac{\partial h(x, y)}{\partial x}\right| \le \frac{L_0}{3d} \quad (27)$$

When the height variation exceeds limitation (27), aliasing errors hamper the phase retrieval.

Application of the Fourier transform technique without spatial heterodyning was proposed by Kreis [44, 176]. Applying a proper bandpass filtering to the Fourier transform

$$D(f_x, f_y) = D_B(f_x, f_y) + D_1(f_x, f_y) + D_1^*(f_x, f_y) \tag{28}$$

of $I(x, y) = I_B(x, y) + \Psi(x, y) + \Psi^*(x, y)$, an estimate $\hat{D}_1(f_x, f_y)$ of $\hat{D}_1^*(f_x, f_y)$ can be derived and the phase distribution restored from

$$\hat{\varphi}(x, y) = \arg\left\{F^{-1}[D(f_x > 0, f_y > 0)]\right\} \tag{29}$$

However, the distortions in the restored phase due to possible overlapping of $D_1(f_x, f_y)$ and $D_1^*(f_x, f_y)$ are more severe in this case in comparison with the spatial heterodyning. This technique is appropriate for objects which cause slowly varying phase modulation centered about some dominant spatial frequency. In view of the obvious relations $f_x(x, y) = \partial\varphi(x, y)/\partial x$ and $f_y(x, y) = \partial\varphi(x, y)/\partial y$, the phase estimate increases monotonically along X and Y [184], and the sign of the local phase variation is not restored.

### 2.3.2 Accuracy Issues and Carrier Removal

Obviously, the two possible ways to improve the accuracy of the FFA is to vary the carrier frequency or the width of the filter window in the frequency domain. To ensure monotonic phase change throughout the FP the carrier frequency should be chosen large enough; however, it may happen that the carrier fringe period, $(f_{0x}^2 + f_{0y}^2)^{-1/2}$, exceeds the spatial resolution of the CCD camera. Therefore, high resolution imaging systems are required for the measurement of steep object slopes and step discontinuities [185]. Besides, introduction of the spatial carrier entails, as a rule, a change in the experimental setup which could require sophisticated and expensive equipment that may not always be available. In addition, the change in the carrier frequency could hardly be synchronized with the dynamic behaviour of the object. The width of the Fourier-plane window affects in opposite ways the accuracy of phase restoration and spatial resolution [186]. The three terms in (25) are continuous functions throughout the Fourier domain. If the filter width is taken too large the information from the rejected orders of the Fourier transform will leek into the processed frequency window leading to phase distortions. Decrease of the width worsens the spatial resolution. A trade-off between accuracy of phase determination and spatial resolution is required.

Obviously, for the real FP that is corrupted by noise the demodulated phase estimate, $\hat{\varphi}(x, y)$, differs from the real phase given by (23). Since the noise covers the whole Fourier transform plane, a decrease in filter width leads to considerable noise reduction. For optimal filtering prior information on the noise and bandwidth of the modulating signals is required. This dependence of filter parameters on the problem to be solved makes automatic processing of the fringe patterns difficult [187]. Using of tight square profile filter window leads to ‘filter ringing’ causing distortions in the restored phase distribution [182]. Phase accuracy of approximately 0.01 fringe is obtained for a Gaussian apodization window centered at the carrier frequency [172]. The main advantage of a Gaussian filter is its continuous nature and absence of zeros in the Fourier transform. Use of a 2D Hanning window is reported in [188] which provides better suppression of noise. The background phase distribution caused by optical aberrations can be also eliminated using differential mode [181]. Substantial reduction of the background intensity can be achieved by the normalization procedure developed in [189] which includes determination of two enveloping 2D functions $e_b(x,y)$ and $e_d(x,y)$ obtained by applying surface fitting to the centre lines of bright and dark fringes. The wrapped phase of the normalized fringe pattern

$$I_n(x,y) = A\frac{I(x,y) - e_d(x,y)}{e_b(x,y) - e_d(x,y)} + B \tag{30}$$

where A and B are normalization constants, remains the same as for the non-normalized pattern, but the contribution of the background is strongly diminished. A transform-domain denoising technique for processing of speckle FPs based on the discrete cosine transform with a sliding window and an addaptive thresholding is developed in [190]. To decrease the noise influence a method to enhance the FP by modifying the local intensity histogram before the Fourier transform is proposed in [184]. Modification is based on monotonic transformation from the real intensity values to the ideal values thus removing the noise without worsening of the contrast. A background removal is proposed in [191] for the case of continuous registration of FPs by adding the patterns in series. After normalization to the grey-level range of the CCD camera, the intensity distribution of the resulting pattern gives the background estimation at high number of added patterns. The method proves to be especially efficient for low carrier frequency FPs when the zero- and first-order peaks overlap to a great extent.

Improvement of the spatial resolution without loss of phase demodulation accuracy is proposed and verified in [186]. The idea is to make use of the two complementary outputs of an interferometer taking in view that the locations of constructive interference in the plane of the first output correspond to destructive interference at the second output, i.e. we have:

$$I_1(x,y) = I_{B1}(x,y) + I_{V1}(x,y)\cos[\varphi_1(x,y) + 2\pi(f_{0x}x + f_{0y}y)] \tag{31}$$

$$I_2(x,y) = I_{B2}(x,y) - I_{V2}(x,y)\cos[\varphi_2(x,y) + 2\pi(f_{0x}x + f_{0y}y)] \tag{32}$$

If precautions are taken to ensure equal contrasts and gains in a perfect way while recording the two interferograms by two different cameras, the zero-order spectrum vanishes at subtraction of the Fourier spectra of both patterns. This permits to increase the size of the window of the filter applied to the first-order spectrum and the spatial resolution respectively by a factor of 2. The FFA method with two complementary interferograms is very useful for images with high spatial frequencies in which the fundamental spectrum is not well localized or for the case of undersampling [181]. Elimination of the zero-order by registration of two FPs phase shifted at $\pi$ using a defocused image of a Ronchi grating is proposed in [192]. The authors reported contribution of the higher orders to be 25% in comparison with the fundamental spectrum. Projection of a quasi-sinusoidal wave and $\pi$ phase shifting technique increase the acceptable height variation to $|\partial h(x,y)/\partial x| \leq L_0/d$ [183].

A modification of the FFA which makes it suitable for a special class of closed FPs is proposed in [173]. The goal is achieved by transforming the closed FP into an open FP in a polar coordinate system using $x = X + r\cos\theta$, $y = Y + r\sin\theta$ where $X,\ Y$ are the coordinates of the center of the closed FP in the Cartesian coordinate system and the point (X,Y) is chosen for the origin of the polar coordinate system. The FP in the $r$-$\theta$ space consists of straight open fringes that permit application of the conventional FFA. However, this is true only for a concave or convex phase surface with the origin of the polar coordinate system coinciding with the apex of the wavefront. The phase retrieved in the $r$-$\theta$ space is transformed back to the Cartesian coordinate system and the phase map of the closed-fringe pattern is recovered.

The Fourier transform is calculated using a discrete Fourier transform (DFT). Using of DFT leads to the so-called leakage for frequencies that are not integer multiplies of $(1/N_x\Delta_x,\ 1/N_y\Delta_y)$ [193]. Several authors point out that the error induced by the leakage effect in the retrieved phase is inevitable due to the discretization of the image by the CCD and non-integer number of fringes within the image [172, 191, 193, 194]. The distortions caused by the leakage are negligible if the carrier frequencies ensure integer number of fringes within the image and the object height distribution is concentrated also within the image [194], i.e. no phase distortions occur at the image boundaries. To avoid the leakage effect when large objects are monitored with a non-vanishing height at image borders, a method is proposed in [194] in which the full image is divided in overlapping subimages by a window that slides along the axis normal to the carrier fringes, e.g. axis X. The window width is chosen approximately equal to one fringe period. If this width is $N_W$, $N_x - N_W$, consecutive images are processed. The next step is to apply Fourier transform successively to all rows parallel to the X-axis of each subimage, thus achieving a local phase demodulation. The sliding pace is one discretization step per subimage which in practice ensures phase recovery at each point of the image and explains why the method is called interpolated or regressive 1D Fourier transform [194]. Briefly, the fringe pattern in each subimage $I(x_k,\ldots,x_{k+N_W},y_l)$ is modelled by a single-frequency sine-wave $I_{k,l}(x) = A_{k,l}\sin(2\pi f_{k,l}x + \varphi_{k,l})$ with frequency $f_{k,l}$ and phase $\varphi_{k,l}$ connected to the height in the point $(k\Delta_x, l\Delta_y)$. The Fourier transform of the sine-wave leads to a set of two non-linear equations which when solved for the two largest Fourier coefficients yield the required frequency $f_{k,l}$ and phase $\varphi_{k,l}$ [194]. The frequencies evaluated by the proposed approach are not limited to the frequencies of the Fourier transform and no leakage occurs. The necessity to find out the two largest spectral lines of the locally computed FFT involves sorting operations which increases slightly the computational burden. Sine-wave modelling gives good results in image regions without abrupt phase changes, i.e. for smooth objects without height discontinuities.

The discrete nature of the Fourier spectrum may cause distortions in the recovered phase at the step of removal of the heterodyning effect. If the sampling interval in the frequency domain is considerably large, it is difficult to translate the positive or negative component of the fundamental spectrum by exactly $(f_{0x}, f_{0y})$ to the origin. If the bias error in the shifted position of the fundamental spectrum is $(\delta f_{0x}, \delta f_{0y})$, the retrieved phase is given by

$$\hat{\varphi}(x,y) = \varphi(x,y)\exp\left\{-2\pi j(x\delta f_{0x} + y\delta f_{0y})\right\} \tag{33}$$

with $|\delta f_{0x,y}| \leq 0.5\Delta f_{0x,y}$, where $\Delta f_{0x}$ and $\Delta f_{0y}$ give the resolution in the frequency domain. The modulation of the true phase may lead to considerable phase shifts in some parts of the object. Distortions in the recovered phase due to the discrete nature of the Fourier spectrum are studied in [175, 180]. The approach proposed there relies on background and carrier frequency evaluation by the least-squares fit of a plane in the part of the recorded image that is not affected by the object. The evaluated phase plane is subtracted from the retrieved phase in the spatial domain. However, this approach is rather cumbersome due to inevitable dependence on the proper choice of the object-free area. An efficient approach is proposed in [195] to evaluate the phase map $\psi(x,y) = 2\pi f_{0x}x + \varphi(x,y)$ from the FP by computing the mean value of its first phase derivative along the X-axis

$$\bar{\psi}'(x,y) = \left.\overline{\frac{\partial[\psi(x,y)]}{\partial x}}\right|_S = 2varphif_{0x} + \left.\overline{\frac{\partial\varphi(x,y)}{\partial x}}\right|_S \tag{34}$$

where $\left.\overline{()}\right|_S$ denotes averaging over the entire image $S$. It is reasonable to assume that the expectation of the derivative is given by $2\pi f_{0x}$. Thus subtraction of the estimate of the mean value (34) from the 2D map of the first phase derivative along the X-axis is expected to yield the first derivative of the phase modulation caused by the object. The first derivative is calculated as a difference of the phase values at two adjacent pixels, $\psi(x_{i+1}) - \psi(x_i)$.

In [196] carrier removal is performed using an orthogonal polynomial curve fitting algorithm. For the purpose, intensity distribution along one row parallel to e.g. X-axis is modelled by a sine-wave whose Fourier transform, $F_s(\omega)$, can be represented theoretically by [196]:

$$F_s(\omega) = \frac{a}{j\omega - \zeta} + \frac{a^*}{j\omega - \zeta^*} \tag{35}$$

where $\zeta$ is the pole of $F_s(\omega)$. By fitting $F_s(\omega)$ with an orthogonal polynomial and using a least-square approach, an estimate of the carrier frequency can be obtained from (35) as $\hat{\omega} = \left|\hat{\zeta}\right|$. The algorithm is based on the assumption that the carrier frequency is the same throughout the whole image. To find the carrier frequency [191] makes use of the sampling theorem applied to the amplitude of the Fourier transform in the spatial frequency domain. Using the interpolation formula [191]:

$$|D(f_x, f_y)| = \sum_{m,n} |D_{mn}| \sin c[\pi(f'_x - m)] \sin c[\pi(f'_y - n)] \, , \qquad f'_{x,y} = f_{x,y}(\Delta f_{x,y})^{-1} \tag{36}$$

with $D_{mn} = D(m\Delta f_x, n\Delta f_y)$, one is able to calculate precisely the carrier frequency.

An important drawback of carrier removal based on a frequency shift or by applying techniques described in [191, 195, 196] is inability to remove possible non-linear component of the carrier frequency. Such situation is encountered when divergent or convergent illumination is used for grating projection on the large- or small-scale object which yields a carrier FP with a non-equal spacing, for which the carrier removal by frequency shift fails [197]. To deal with this case Takeda et al proposed in [171] to use a reference plane. This solution entails implications such as the need of two measurements as well as the careful adjustment of the reference plane and increases the overall uncertainty of the measurement. Srinivasan et al. [198] propose a phase mapping approach without a reference plane. There have been developed methods that directly estimate a phase-to-height relationship from the measurement system geometry without estimating the carrier frequency. A profilometry method for a large object under divergent illumination is developed in [199] with at least three different parallel reference planes for calibration of the geometrical parameters of the system. The calibration permits to convert directly the phase value composed of both the carrier and shape-related components to a height value. However, high accuracy of determination of the geometrical parameters is required which makes the process of calibration very complicated. A general approach for the removal of a nonlinear-carrier phase component in crossed-optical-axes geometry is developed in [200] for divergent projection of the grating with a light beam directed at angle $\alpha$ to the normal to the reference plane and a CCD camera looking normally at it. If for this optical geometry the carrier fringes are projected along the Y-axis, the phase induced by them depends on x-coordinate in a rather complicated way [200]

$$\phi(x) = 2\pi \int_0^x f_{0x}(u)du = 2\pi p L_1 H \int_0^x (L_2 + u \sin\beta)^{-1} [H^2 + (d+u)^2]^{1/2} du + \phi(0) \tag{37}$$

where $\phi(0)$ is the initial carrier phase angle, $p$ is the grating pitch, $\beta$ is the angle between the grating and the reference plane and $L_1$, $L_2$, $H$ and $d$ are distances characterizing the optical geometry. The authors propose to use a power series expansion for $\phi(x)$:

$$\phi(x) = \sum_{n=0}^{\infty} a_n x^n \tag{38}$$

and to determine the coefficients $a_0, a_1, \ldots, a_n \ldots$ by a least-squares method minimizing the error function:

$$\Omega(a_0, a_1, \ldots, a_N) = \sum_{(x,y)\in S} [a_0 + a_1 x + \ldots + a_N x^N - \varphi(x,y)]^2 \tag{39}$$

where S comprises all image points, $\varphi(x, y)$ is the unwrapped phase, and the number $N$ ensures an acceptable fit to $\varphi(x, y)$. The method is generalized for carrier fringes with an arbitrary direction in the spatial plane. The phase-to-height conversion becomes much simpler at successful elimination of the nonlinear carrier.

Reliability of the FFA is thoroughly studied in [193] at all steps involved in the phase demodulation by means of 1D model of an artificial ideal noise-free open-fringes sinusoidal FP with constant magnitudes of $I_B(\vec{r})$, $I_V(\vec{r})$ and $\varphi(\vec{r})$ throughout the image. The purpose of analysis is to identify only the errors inherent in the FFA. The filter used in the spatial frequency domain is a rectangular window apodized by a Gaussian function. As a result, an improved formula for phase derivation from the complex signal $\Psi(x, y)$ is proposed.

One of the most serious problems of the FTP arises from objects with large height discontinuities that are not band-limited which hinders application of the Fourier analysis. In addition, discontinuous height steps and/or spatially isolated surfaces may cause problems with the phase unwrapping [158, 201]. A modification of FFA, proposed in [182], makes unnecessary phase unwrapping by simple elimination of any wraps in the calculated phase distribution. This is achieved by proper orientation of the projected fringes and by choosing independently the angle between the illumination and viewing directions, $\theta$, and the fringe spacing, $L$, in a way as to fulfil the requirement $h(x, y)L^{-1} \sin\theta \leq 1$ after removal of the carrier frequency. Obviously, the method is efficient only for comparatively flat objects at the expense of decreased resolution. A two-wavelength interferometer is developed in [202]. The recorded pattern is given by

$$\begin{aligned} I(x,y) = I_B(x,y) + I_{V1}(x,y)\cos[2\pi f_{1x} + \varphi_1(x,y)] \\ + I_{V2}(x,y)\cos[2\pi f_{2x} + \varphi_2(x,y)], \end{aligned} \tag{40}$$

where $\varphi_{1,2} = 2\pi h(x, y)/\lambda_{1,2}$ and $f_{1,2x}$ are inversely proportional to both used wavelengths. The Fourier transform of the recorded pattern yields

$$D(f_x, f_y) = D_B(f_x, f_y) + \sum_{k=1}^{2} [D_1^k(f_x - f_{1x}, f_y) + D_1^{k*}(f_{0x} + f_{1x}, f_y)] \quad (41)$$

Two first-order spectra are selected, e.g. $D_1^1$ and $D_1^{2*}$, by bandpass filtering and shifted towards the origin of the coordinate system. After the inverse Fourier transform one obtains:

$$\Psi(x, y) = I_V(x, y) \cos[\Xi(x, y)] \exp[j\Gamma(x, y)] \quad (42)$$

where precautions are taken to provide $I_V(x, y) = I_{V1}(x, y) = I_{V2}(x, y)$ and $\Xi(x, y) = \pi h(x, y)/\Lambda_1$ and $\Gamma(x, y) = \pi h(x, y)/\Lambda_2$. Here $\Lambda_1 = \lambda_1\lambda_2/(\lambda_1 + \lambda_2)$ is the average wavelength, and $f_x = \frac{\omega_0}{a_R}$ is the synthetic wavelength. As it could be seen, the phase modulation using the synthetic wavelength substantially increases the range of the interferometric measurement without need for phase unwrapping.

Correct restoration of the 3D object shape and accurate phase unwrapping across big height variations and surface discontinuities can be done using multiple phase maps with various sensitivities. A method called spatial-frequency multiplexing technique was proposed in [203]. The proposed idea is extended in [204] to a technique termed multichannel FFA. The key idea of the method is that phase discontinuities which are not due to the processing algorithm but to surface discontinuities would appear at the same location on FPs generated with differing carrier frequencies. These FPs can be projected simultaneously on the object surface if FFA is used [203]. The spectra that correspond to the used multiple FPs are separated in the frequency space by means of a set of bandpass filters tuned to the carrier frequencies of the fringes. A FFA interferometric technique for automated profilometry of diffuse objects with discontinuous height steps and/or surfaces spatially isolated from one another is designed and tested in [201]. It makes use of spatiotemporal specklegrams produced by a wavelength-shift interferometer with a laser diode as a frequency-tunable light source. Necessity to record and process multiple FPs under stringent requirement for vibration-free environment is the main drawback of the developed approach. Phase demodulation and unwrapping by FFA for discontinuous objects and big height jumps obtains further development in [205]; the merit of the work is that all necessary information is derived from a single FP. This is achieved by combining spatial-frequency multiplexing technique with Gushov and Solodkin unwrapping algorithm [206]. The FP projected on the object consists of multiple sinusoids with different carrier frequencies:

$$I(x, y) = I_B(x, y) + I_V(x, y) \sum_{k=1}^{K} \cos[\varphi_k(x, y) + 2\pi(f_{kx}x + f_{ky}y)] \quad (43)$$

Defining a set of simultaneous congruence equations for the real height distribution and height distributions corresponding to wrapped phase maps $\varphi_k(x, y)$

and using the Gushov and Solodkin algorithm, phase unwrapping can be done pixelwise. A coaxial optical sensor system is described in [207] for absolute shape measurement of 3-D objects with large height discontinuities and holes without shadowing. This is achieved by a depth of focus method with a common image plane for pattern projection and observation. The FFA is applied for evaluation of the contrast, $I_V(x, y)$. The absolute height distribution is determined from the translation distance of the image plane that ensures a maximum fringe contrast at each pixel like in a white-light interferometry. Absolute phase measurement using the FFA and temporal phase unwrapping is developed in [188]. Use of a four-core optical fibre for pattern projection and 2D Fourier analysis is demonstrated in [208]. The projected FP is formed as a result of interference of the four wave fronts emitted from the four cores located at the corners of the square.

In its essence, the FTP is based on determination of the quadrature component of the signal, i.e. it is described by approximation of the Hilbert transform. Kreis [209] is the first who applies a 2D generalized Hilbert transform for phase demodulation. However, the discontinuity of the used Hilbert transform operator at the origin leads to ringing in the regions where the phase gradient is close to zero. Accuracy of this approximation depends on the bandwidth of the processed signal. Contrary to the traditional opinion that it is not possible to find natural isotropic extension of the Hilbert transform beyond one dimension and to apply the analytic signal concept to multiple dimensions, a novel 2D quadrature (or Hilbert) transform is developed in [210, 211] as a combined action of two multiplicative operators: two-dimensional spiral phase signum function in the Fourier space and an orientational phase spatial operator. The quadrature component of the FP $\tilde{I}(\vec{r}) = I(\vec{r}) - I_B(\vec{r})$ obtained after the removal of background is obtained from the approximation

$$j \exp[j\theta(\vec{r})] I_V(\vec{r}) \sin[\varphi(\vec{r})] \cong F^{-1}\{S(\vec{f}) F[\tilde{I}(\vec{r})]\} \tag{44}$$

where $\theta(\vec{r})$ is the fringe orientation angle, and $S(\vec{f})$ is the 2D spiral phase signum function

$$S(\vec{f}) = \frac{f_x + j f_y}{\sqrt{f_x^2 + f_y^2}} \tag{45}$$

The new transform shows effective amplitude and phase demodulation of closed FPs. A vortex phase element has been applied in [212] for demodulation of FPs. The phase singularity of the vortex filter transforms the FP into a pattern with open fringes in the form of spirals which allows for differentiating between elevations and depressions in the object.

## 2.4 Space-frequency Representations in Phase Demodulation

### 2.4.1 Wavelet Transform Method

The FFA as a global approach exhibits unstable processing for patterns with low fringe visibility, non-uniform illumination, low SNR as well as in the presence of local image defects which influence the entire demodulated phase map [213]. Since the spatial gradient of the phase is proportional to the fringe density, information about the latter is a step towards phase demodulation. This observation paves a ground for introduction of space-frequency methods in the fringe analysis. New phase retrieval tools have been applied as the windowed Fourier transform (WFT) [214, 215] and the continuous wavelet transform (CWT) [216].

The wavelet transform is a method that can detect the local characteristics of signals. This explains extensive research in wavelet processing of FPs and interferograms during the last decade [217, 218]. It could be very useful for patterns with great variation of density and orientation of fringes – the case in which the standard FFA fails [28]. The other methods that are capable to ensure localized phase retrieval, as the WFT or the regularised phase-tracking algorithm generally would require *a priori* information about the fringe density and orientation. In the wavelet transform analysis it is not necessary to choose the filter in the frequency domain. An extensive review of the wavelet transform can be find in [219].

The idea to apply the CWT to the 2-D fringe data is proposed independently in [220] and [213]. The CWT can be applied both to open and closed fringes. The CWT shows promising results as a denoising tool for interferograms in holography and speckle interferometry [221] and as a method to improve bad fringe visibility in laser plasma interferometry [213]. In white-light interferometry, CWT proves to be very effective for detecting the zero optical path length [222]. The wavelets can be very useful for finding the zones with a constant law of variation of the fringes [223]. The CWT of a 1D function *I(x)* is defined as

$$\Phi(a,b) = \int\limits_{-\infty}^{\infty} I(x)\psi^*_{a,b}(x)dx = \sqrt{a}\int\limits_{-\infty}^{\infty} \hat{\psi}(af_x)D(f_x)\exp(jbf_x)df_x \qquad (46)$$

where $\psi_{a,b}(x) = |a|^{-1/2}\psi\left(\frac{x-b}{a}\right)$, $a \neq 0$ and $b$ are scaling and translation parameters which are real, and $\hat{\psi}(x) = F[\psi(x)]$. The kernel of the transform is a single template waveform, the so-called mother wavelet $\psi(x)$ which should satisfy the admissibility condition [219], in order to have a zero mean and should present some regularity to ensure the local character of the wavelet transform both in the space and frequency domains. The above conditions mean that the wavelet can be considered as an oscillatory function in the spatial domain and a bandpass filter in the frequency domain. The scaling factor entails the change of the width of the analyzing function thus making possible analysis of both high-frequency and low-frequency components of a signal with good resolution. Usually, the mother wavelet is normalized to have a unit norm [219]. The wavelet transform decomposes the input function over a set of scaled and translated versions of the mother wavelet. The Fourier transform of the daughter wavelet $\psi_{a,b}(x)$ is

$$\hat{\psi}_{a,b}(f_x) = |a|^{1/2}\hat{\psi}(af_x)\exp(-jbf_x) \tag{47}$$

where $\hat{\psi}(f_x)$ is the Fourier transform of the mother wavelet.

The wavelet transform $\Phi(a,b)$ plotted in the spatial coordinate/spatial frequency space gives information about the frequency content proportional to $1/a$ at a given position $b$. In case of the FPs the translation parameter $b$ follows the natural sampling of the FP, given by the pixel number, $b \to n, n = 0,\ldots,N$, where $N$ is the total number of pixels. The parameter $a \in [a_{\min}, a_{\max}]$ is usually discretized applying a log sampling $a = 2^m$, where $m$ is an integer. Finer sampling is given by [219, 224]:

$$\psi_n^{\nu}(x) = 2^{-(\nu-1)/N_{\nu}}\psi(2^{-(\nu-1)/N_{\nu}}x - n), \nu = 1,\ldots,N_{\nu} \tag{48}$$

where the fractional powers of 2 are known as voices and the spatial coordinate $x$ is also given in the units of a pixel number. One should make a difference between the CWT and the discrete wavelet transform which employs a dyadic grid and orthonormal wavelet basis functions and exhibits zero redundancy.

The modulus of the CWT $|\Phi(a,b)|^2$ is the measure of a local energy density in the $x - f_x$ space. The energy of the wavelet $\psi_{a,b}(x)$ in the $x - f_x$ space is concentrated in the so-called Heisenberg box centered at $(b, \eta/a)$ with lengths $a\Lambda_x$ and $\Lambda_f/a$ along the spatial and frequency axis respectively, where $\int\limits_{-\infty}^{\infty} x^2|\psi(x)|^2 dx = \Lambda_x^2$, $\frac{1}{2\pi}\int\limits_{0}^{\infty}(f_x - \eta)^2|\hat{\psi}(f_x)|^2 df_x = \Lambda_f^2$ and $\frac{1}{2\pi}\int\limits_{0}^{\infty} f_x|\hat{\psi}(f_x)|^2 df_x = \eta$. The area of the box, $\Lambda_x\Lambda_f$, remains constant. The plot of $I(x) = I_B(x) + I_V(x)\cos[2\pi f_{0x}(x)x + \varphi(x)]$ as a function of position and frequency is called a scalogram [215, 216]. The huge amount of information contained in the CWT $\Phi(a,b)$ could be made more condensed if one considers the local extrema of $\Phi(a,b)$. Two definitions of CWT maxima are widely used:

i) wavelet ridges used for determination of the instantaneous frequency and defined as

$$\frac{d(|\Phi(a,b)|^2/a)}{da} = 0; \tag{49}$$

ii) wavelet modulus maxima used to localize singularities in the signals and defined as

$$\frac{d|\Phi(a,b)|^2}{db} = 0; \tag{50}$$

The choice of a proper analyzing wavelet is crucial for the effective processing of the FPs. The most frequently used in interferometry and profilometry wavelet is the truncated form of the Morlet wavelet which is a plane wave modulated by a Gaussian envelope

$$\psi(x) = \pi^{-1/4}\exp(j\omega_0 x)\exp\left(-\frac{x^2}{2}\right) \tag{51}$$

It is well-suited for processing of pure sinusoids or modulated sinusoids; $\omega_0$ is the central frequency. The correction term $\exp(-\omega_0^2/2)$ which is introduced in the complete form of the Morlet wavelet $\psi(x) = \pi^{-1/4}\exp(j\omega_0 x - \omega_0^2/2)\exp(-x^2/2)$ to correct for the non-zero mean of the complex sinusoid is usually neglected as vanishing at high values of $\omega_0$. Usually $\omega_0 > 5$ is chosen to ensure $\hat{\psi}(f_x = 0) \approx 0$ [221], which means that the Morlet wavelet has five 'significant' oscillations within a Gaussian window. The Morlet wavelet provides high frequency resolution. The Fourier transform and energy spectrum of the Morlet wavelet are

$$\hat{\psi}(f_x) = \sqrt{2}\sqrt[4]{\pi}\exp\left[-\frac{(f_x - \omega_0)^2}{2}\right] \text{ and } |\hat{\psi}(f_x)|^2 = 2\sqrt{\pi}\exp\left[-(f_x - \omega_0)^2\right] \tag{52}$$

For complex or analytic wavelets the Fourier transform is real and vanishes for negative frequencies. So, the Morlet wavelet removes the negative frequencies and avoids the zero-order contribution [221]. The Morlet wavelet produces a bandpass linear filtering around the frequency $\omega_0/a$. Two other wavelets used in fringe analysis are the Mexican hat wavelet [216] and the Paul wavelet of order $n$ [225].

The apparatus of the wavelet ridges can be used for phase demodulation of FPs, if the analyzing wavelet is constructed as $\psi(x) = g(x)\exp(j\omega_0 x)$, where *g(x)* is a symmetric window function and $\omega_0 > 2\Lambda_f$, i.e. $\psi(x)$ practically rejects negative frequencies. The CWT of the AC component of one row or column of the FP *I(x,y)* takes a form:

$$\begin{aligned}\Phi(a,b) =& a^{-1/2}\int_{-\infty}^{\infty} I_V(x)\cos\varphi(x) g\left(\frac{x-b}{a}\right)\exp\left[-j\frac{\omega_0}{a}(x-b)\right]\\ dx =& \mathrm{Z}(\varphi) + \mathrm{Z}(-\varphi)\end{aligned} \tag{53}$$

where

$$\mathrm{Z}(\varphi) = \frac{a^{-1/2}}{2}\int_{-\infty}^{\infty} I_V(x+b)\exp[j\varphi(x+b)] g\left(\frac{x}{a}\right)\exp\left(-j\frac{\omega_0}{a}x\right)dx \tag{54}$$

It is difficult to solve analytically the integral in (54), but in the case of small variation of visibility and phase of the fringes over the support of the analyzing wavelet $\psi_{a,b}$, we can use a Taylor series expansion of $I_V(x)$ and $\varphi(x)$ to the first order to simplify (54).

$$I_V(x+b) \approx I_V(b) + xI'_V(b),\ \ \varphi(x+b) \approx \varphi(b) + x\varphi'(b) \tag{55}$$

where $I'_V(b)$ and $\varphi'(b)$ are the first order derivatives of $I_V$ and $\varphi(b)$ with respect to $x$. Taking in view the symmetric character of *g(x)* and the condition $\omega_0 > 2\Lambda_f$, one obtains [216]:

$$\Phi(a,b) \approx Z(\varphi) = \frac{\sqrt{a}}{2} I_V(b)\hat{g}\left\{a\left[\frac{\omega_0}{a} - \varphi'(b)\right]\right\}\exp[j\varphi(b)] \tag{56}$$

To make contributions of the second order terms negligible, the following nonequalities should be fulfilled for the second order derivatives [216]:

$$\frac{\omega_0^2}{|\varphi'(b)|^2}\frac{|I_V''(b)|}{|I_V(b)|} << 1 \text{ and } \omega_0^2\frac{|\varphi''(b)|}{|\varphi'(b)|^2} << 1 \tag{57}$$

As it can be seen from the expression (56), there are two possible ways to determine the phase from the CWT behaviour on the ridge:

i) from the rescaled scalogram

$$\frac{|\Phi(a,b)|^2}{a} = \frac{I_V^2(b)}{4}\left|\hat{g}\left\{a\left[\frac{\omega_0}{a} - \varphi'(b)\right]\right\}\right|^2 \tag{58}$$

which for the points on the ridge yields directly the instantaneous frequency $\omega_0 a_R^{-1}(b) = \varphi'(b)$, where $a_R$ is the value that maximizes $|\Phi(a,b)|^2$;

ii) from the phase of the CWT on the ridge

$$\Phi(a_R,b) \approx Z(\varphi) = \frac{\sqrt{a_R}}{2} I_V(b)\exp[j\varphi(b)] \tag{59}$$

In the gradient-based algorithm the phase is calculated by integration and no phase unwrapping is needed. In (59) the phase is determined modulo $2\pi$. Obviously in the case of open fringes the phase of the ridge is exactly the same as the phase of the signal [226]. For the closed fringes the sign of the phase gradient should be determined independently, e.g. by employing PS technique [227]. The ridge extraction is correct only for the so-called analytic asymptotic limit of the intensity signal with respect to the width of the analyzing wavelet which is a severe limitation on the CWT method, especially if objects with cracks, holes, or such that introduce slow variations in the phase are to be evaluated [221]. Analysis made in [221] reveals that the CWT method exhibits high accuracy at large phase gradients whereas slow variations of the phase are not so well localized. Improvement of accuracy requires to adopt the higher spatial fringe frequency direction [221]. The gradient-based method needs also knowledge in advance of the sign of the first derivative of the phase, and also of the phase itself over a set of points. Along the ridge of the 3-D surface $\Phi(a,b)$ the true input signal is efficiently captured even when it is strongly contaminated with noise. The strong noise suppression is intrinsic for the ridge extraction procedure. In other words, the phase gradient in the vicinity of the pixel $b$ is proportional to $1/a_R$. The ridge points can be found by a standard procedure applied to determine the maximum of a function or by more sophisticated algorithms to select accurately the ridge in noisy FPs. The direct approach when the maximum of $\Phi(a,b)$ is searched as the highest magnitude at each value of $b$ works well at high SNRs. In [228] ridge detection is based on minimization by Monte-Carlo type methods of a penalty function on the set of all possible ridge curve candidates taking into account *a priori* information of the signal and the noise. The procedure is shown to be robust to additive white noise. In [229] a cost function is built for the adaptive selection of the ridge:

$$\cos t[\varphi(b), b] = -C_0 \int\limits_b |\Phi[\varphi(b), b]|^2 db + C_1 \int\limits_b \left| \frac{\partial \varphi(b)}{\partial b} \right|^2 db \tag{60}$$

where $\varphi(b)$ is a parameter curve of $b$; $C_0, C_1$ are the positive weight coefficients. The cost function is small for signals with large magnitude and a smooth parameter curve.

In [220] the CWT is applied to the rows of a 2D interferogram using a Morlet analyzing wavelet. Each row after being extended by interpolation at its both edges to avoid discontinuities is processed separately from the other rows, and the phase is retrieved by integration from the phase gradient up to an additive constant. To find these constants, the CWT is applied also to the diagonal of the FP and the heights of the rows are adjusted correspondingly. Due to integration of the phase gradient, no phase unwrapping is required. Phase evaluation by integration of the phase gradient with a Paul wavelet is proposed in [230]. The efficiency of this analyzing wavelet is checked by means of simulated FPs which are processed row by row with extension of each row on both sides by zero padding. Reference [231] justifies CWT application in fringe profilometry with crossed-optical geometry. It is shown that the modulated phase $\Delta\varphi(x, y) = \varphi(x, y) - \varphi_r(x, y)$ can be obtained as a difference

$$\Delta\varphi(x, y) = \varphi(x, y) - \varphi_r(x, y) = \varphi(a_R, b) - \varphi_r(a_R^r, b) \tag{61}$$

where $a_R^r$ is the scale factor at the ridge of FP on the reference plane at every position $b$. The simulations and experiment prove that the CWT phase retrieval with the Morlet wavelet overcomes the limitation imposed by the FT profilometry on the height of the investigated objects. The same wavelet is used in [232] where the authors make comparison between the gradient-based CWT, phase-based CWT and FT profilometry.

A technique which is totally different from the gradient-based and phase-based CWT phase demodulation of carrier fringe patterns is presented in [233]. It implies that the spatial carrier frequency is much larger than expansion of the spectrum associated with the height variation of the object. The basic idea is to isolate the carrier frequency from the spectrum of $\varphi(x, y)$ on the frequency scale. For the purpose, the CCD-recorded spatial carrier FP is modulated by two sinusoidal waves generated at the carrier frequency $f_{x_0}$ and phase-shifted at $\pi/2$:

$$\begin{aligned} M_s(x, y) = {} & I_B(x, y)\sin(2\pi f_{0x}) \\ & + I_V(x, y)\left\{\cos[4\pi f_{0x} x + \varphi(x, y)] - \sin\varphi(x, y)\right\} \end{aligned} \tag{62}$$

$$\begin{aligned} M_c(x,y) = I_B(x,y)\cos(2\pi f_{0x}) \\ +I_V(x,y)\left\{\cos[4\pi f_{0x}x + \varphi(x,y)] + \cos\varphi(x,y)\right\} \end{aligned} \tag{63}$$

As it can be seen, the spectra of the terms $I_V(x,y)\sin\varphi(x,y)$ and $I_V(x,y)$ $\cos\varphi(x,y)$ are the lowest on the frequency scale. Now the object spectrum can be separated from all other contributions in (62) and (63) by the CWT using as an analyzing wavelet the scaling function which puts the spectra of $I_V(x,y)\sin\varphi(x,y)$ and $I_V(x,y)\cos\varphi(x,y)$ in the approximation band. This method requires phase unwrapping. The shortcomings of the method are the necessity to know the carrier frequency and the constraint imposed on the range of object phase variation.

In [234] the CWT is applied to remove irregular localized noise in a set of low-SNR phase-shifted moiré interferograms which are typical for measurements in which the physical change is of the order of the measurement sensitivity. The 1D CWT is used for preprocessing of the phase-shifted patterns recorded using a four-step algorithm. It is shown that the ridge extraction of the CWT yields information about the local spatial frequencies at each position of the processed FP whereas the spurious frequencies connected with the noise have negligible contribution in the ridge formation. Thus, restoration of the local frequency map from the ridge detection permits to regenerate denoised FPs.

Four-step PS interferometry and CWT are combined in [235] for phase demodulation with increased accuracy in moiré interferometry with noisy FPs. To avoid the error in calculation of the CWT that arises from the finite length of the data sequences, the authors propose to introduce computer-generated carrier phase in a way that the modified input sequence contains enough spatial periods to neglect the finite length of the data array. Application of the CWT to the measurement of in-plane displacements by the digital speckle pattern interferometry (DSPI) and out-of-plane deflection by the projecting moiré fringes has been recently reported for demodulation of fringes with non-uniform carrier frequency distribution over the image [236]. Considering a 1-D FP $I(x) = I_B(x) + I_V(x)\cos[2\pi f_{0x}(x)x + \varphi(x)]$ with a non-uniform carrier $f_{0x}(x)$ and representing the phase $\varphi(x)$ as a Taylor series near the point of interest $b$ up to the linear term $\varphi(x) \approx \varphi(b) + \varphi'(b)(x-b)$ on a limited support $[b - as, b + as]$ for a Morlet analyzing mother wavelet with a support $[-s, s]$, it is obtained [236]:

$$\begin{aligned} \Phi(a,b) = \sqrt{2\pi} I_B(b)\exp\left(-\tfrac{\omega_0^2}{2}\right) \\ +\tfrac{\sqrt{2\pi}}{2} I_B(b) I_V(b)\exp\{j\Omega(b)\}\exp\left(-\tfrac{a^2}{2}\Theta\right) \end{aligned} \tag{64}$$

where $\Theta = \Theta(a,b,\omega_0)$ and the phase $\Omega(b) = 2\pi f(b)b + \varphi(b)$ of $\Phi(a,b)$ contains information about the modulation phase $\varphi(x)$ at any point $b$ for a fixed value of $a$. The obtained expression permits to derive the phase change between two states of the object under condition that local value of the carrier frequency is kept unchanged. Since the support window depends on the scaling parameter $a$, a statistical procedure is developed to derive the phase searching in the whole scaling range of the wavelet transform. A similar idea is proposed in [237] for elimination of phase distortion in phase-shifted fringe projection method caused by declination of the projected FP from the ideal sinusoidal form. By differentiating the above expression for $\Phi(a, b)$, the phase value $\Omega(b)$ is evaluated from

$$\Omega(b) = \tan^{-1}\left\{\frac{\mathrm{Im}[\Phi(a_{\max}, b)]}{\mathrm{Re}[\Phi(a_{\max}, b)]}\right\} = 2\pi f_x b + \varphi(b) \tag{65}$$

where $a_{\max}$ is obtained from $d\Phi(a, b)/da = 0$. The described procedure for phase extraction requires phase unwrapping. Application of CWT for localization of defects in FPs in non-destructive testing is described in [238]. A new approach for micro-range distance measurement that makes use of moiré effect and wavelet representation is described in [239]. The 1D wavelet analysis with a Mexican hat wavelet is used to determine the pitch of the moiré pattern. In [226] a correlation is observed between a FP and its wavelet map. On the basis of this observation an algorithm is presented for reconstruction of lines of interference fringes, which, however, is effective only for vertical fringes. In all modifications of the CWT approach the 2-D FPs are simplified to 1D patterns [233]; therefore their implementation requires long computation times. At the same time, none of these modifications exhibit results that are superior to other widely used fringe processing techniques.

### 2.4.2 Windowed Fourier Transform Method

The 1D WFT and inverse WFT of the function $\zeta(x)$ can be written in a form:

$$\mathrm{Z}(u, f_x) = \int_{-\infty}^{\infty} \zeta(x) g(x-u) \exp(-j f_x x) dx \tag{66}$$

$$\zeta(x) = \frac{1}{2\pi} \int_{-\infty}^{\infty} \int_{-\infty}^{\infty} Z(u, f_x) g(x-u) \exp(j f_x x) df_x du \tag{67}$$

where $Z(u, f_x)$ is the WFT spectrum. As it can be seen, the WFT is similar to the FT except for the symmetrical window function $g(x)$. The WFT kernel is obtained by translation of the window at $u$ and by modulation at frequency $f_x$. The WFT processes the signal mainly in the local area defined by the extent of the window and signals that are separated by a distance greater than the window width do not influence each other. Thus the WFT spectrum gives information not only about contribution of different spectral components but also about where in the signal domain they occur. The resolution limit or the smallest Heisenberg box [215, 240] is achieved for a Gaussian window.

The WFT with a Gaussian window is usually called the Gabor transform. The extension of the 1D WFT to the 2D is straightforward.

Introduction of the window restricts the processed signal area and simplifies interpretation of the spectrum [214] which may consist of a single peak in the considered local area. Another advantage of the WFT can be effective noise reduction by implementation of a threshold that simply cuts off the low noise spectral amplitudes which are spread all over the frequency domain. Similar to CWT, these particular features of the WFT put foundations for two processing approaches known as the WF ridges method and the WF filtering method [214].

The Windowed Fourier filtering can be applied to phase-shifted patterns as well as to a single pattern with carrier fringes [241]. In the case of a four-step algorithm with $\pi/2$ phase step, the four recorded patterns can be combined to form the following complex signal [214, 240]:

$$I_{PS}(x) = \frac{1}{2}[I_1(x) - I_3(x) + jI_4(x) - jI_2(x)] = I_V(x)\exp[j\varphi(x)] \tag{68}$$

that undergoes the WFT filtering. In the case of a carrier FPs the signal itself is formed of a background and two exponential functions. By using the definition of the WFT, filtering of (68) or of a carrier FP is described with the following expression [214]:

$$\bar{I}(x) = \frac{1}{2\pi}\int\limits_a^b \left\{ \left[\overline{I(x)\otimes g(x)\exp(jf_x x)}\right] \otimes g(x)\exp(jf_x x)\right\} df_x \tag{69}$$

where $\otimes$ denotes a convolution with respect to the variable $x$, $\left[\overline{I(x)\otimes g(x)\exp(jf_x x)}\right]$ denotes that the threshold has been applied, and all spectrum parts that are below the threshold are set to zero. By setting the integration limits $a$ and $b$ only the desired part of the spectrum is processed interactively. In the case of phase-shifted images one chooses $a < 0$ and $b > 0$ to include both negative and positive frequencies of the FP. For carrier FPs by choosing $b > a > 0$, rejection of the background and the negative frequencies is accomplished. The WFT noise filtering outperforms the conventional FT filtering [242]. However, the need to determine the threshold and the limits $a$ and $b$ from the recorded FPs is a serious shortcoming.

To discretize optimally the continuous WFT, the authors of [242] apply frame theory to form a tight-windowed Fourier frame. It is shown by computer simulation that the tight frame is achieved if sampling intervals in the frequency domain are chosen inversely proportional to the spatial extensions of the 2D Gaussian kernel. The noise reduction achieved by the WF frame is better in comparison with the results obtained with the orthogonal wavelet transform.

The windowed Fourier ridges method relies on the assumption [240] that both $I_B(x)$ and $I_V(x)$ and the first derivative of the phase $\varphi'(x) = d\varphi(x)/dx$

are slowly varying functions over the window extent. It can be shown that in this case the WFT consists of 3 terms [240]:

$$\mathrm{Z}(u, f_x) = Z(I_B) + Z(\varphi) + Z(-\varphi) \tag{70}$$

where we have

$$Z(I_B) = I_B(u)\exp(-juf_x)\hat{g}(f_x) \tag{71}$$

$$Z(\pm\varphi) = \frac{1}{2}I_V(u)\exp\{\pm j[\varphi(u) \mp uf_x]\}\,\hat{g}[f_x \mp \varphi'(u)] \tag{72}$$

and the circumflex denotes the Fourier transform. The three terms of the WFT are separated in the frequency domain if $\varphi'(u) > \Lambda_f$, i.e. if the fringe density is rather high. In this case the terms $\mathrm{Z}(I_B)$ and $\mathrm{Z}(-\varphi)$ are negligible on the ridge of the transform at $f_x = \varphi'(u)$. This condition can be satisfied by introduction of carrier fringes. The carrier fringes are not necessary if the WFT is combined with the four-step PS technique [240]:

$$I_i = I_{Bi} + I_{Vi}\cos[\varphi + (i-1)\pi/2], i = 1, 2, 3, 4 \tag{73}$$

It is easy to show that [240]

$$\mathrm{Z}_1 - \mathrm{Z}_3 = 2\mathrm{Z}(\varphi) + 2\mathrm{Z}(-\varphi), \mathrm{Z}_4 - \mathrm{Z}_2 = \frac{2}{j}\mathrm{Z}(\varphi) + \frac{2}{j}\mathrm{Z}(-\varphi) \tag{74}$$

where $\mathrm{Z}_i$ is the WFT of the pattern $I_i$. Obviously, $\mathrm{Z}(\varphi)$ can be readily computed from

$$\mathrm{Z}(\varphi) = 0.25(\mathrm{Z}_1 - \mathrm{Z}_3 + j\mathrm{Z}_4 - j\mathrm{Z}_2) \tag{75}$$

even if $\varphi'(u) > \Lambda_f$ is not fulfilled but at the expense of recording four FPs instead of one.

Capability of the WFT to localize abrupt changes in the fringe density or local frequency makes it a suitable algorithm for fault detection [232] and condition monitoring in optical non-destructive testing. The WFT combines insensitivity to noise of the FFA and sensitivity to local changes of cross-correlation methods. Monitoring of local frequencies gives information about the FP evolution. The WFT or Gabor filtering is applied in [243] for effective removal of the spatial carrier in the case of real FPs, which could be hardly expected to have parallel and equally spaced spatial carrier fringes. To ensure effective phase demodulation in such cases, the method developed in [243] performs localized matching filtration with Gabor filters that form a specially constructed multi-channel Gabor spatial filter set which spans the total variation range of the carrier frequency $\vec{f_0} = (f_{x0}, f_{y0}) = \vec{f_0}(x, y)$. By comparing the outputs of the filters at each point $(x, y)$, a value of the central frequency of the filter with the maximum output is assigned to $\vec{f_0}(x, y)$. However, the underlying theory puts the constraint on the analyzed phase field which should vary so slowly that its spectrum to be entirely covered by the frequency band of each of the Gabor filters. Strain contouring using a set of Gabor filters is described also in [244]. In [245] a dilating Gabor transform is introduced by using a Gaussian function with a changeable window in order to improve the WFT efficiency when processing FPs with a spectral content that strongly varies across the FP. It is shown that the Fourier transform spectrum can be represented as a sum of the spectra obtained by the Gabor transform at different locations of the FP.

### 2.5 Single Frame Methods

As we have seen, phase demodulation is a relatively simple procedure for carrier-frequency FPs or for open fringes. However, introduction of carrier fringes in real time by technical means is a complicated task and restricts the spectrum of the signal that may be recovered. In many cases one encounters the problem to process wideband FPs without frequency that is dominant throughout the FP. Such are closed FPs in which the phase experiences nomonotonous change or FPs, in which the signal is noise dependent [246]. A frequently met problem is phase demodulation from patterns with partial-field fringes, in which the FP is available in a subregion of the image. The full-field methods as the Fourier transform applied to such a FP leads to artefacts at the borders. Suitable for the closed FPs is the PS technique but at the expense of acquisition of several frames which is unacceptable for time-varying scene capture. This motivates concentration of efforts on the development of phase demodulation techniques from a single FP which in general may consist of closed fringes.

From the mathematical point of view phase demodulation of a single FP is an ill-posed problem because of the inherent sign ambiguity [140]. The phase distributions $\varphi_1(x,y) = (x^2+y^2)$, $\varphi_2(x,y) = -(x^2+y^2)$, $\varphi_3(x,y) = \left|W(x^2+y^2)\right|$, $\varphi_4(x,y) = (x^2+y^2)$ at $x \le 0$ and $-(x^2+y^2)$ at $x > 0$ create the same FP [30, 247], as follows from $\cos\varphi_1 = \cos\varphi_3 = \cos\varphi_3 = \cos\varphi_4$; $W(.)$ is a phase wrapping operator. This makes impossible derivation of a unique solution from the observed data without introduction of prior constraints in the demodulation algorithm [140, 247]. Filtering an image or phase unwrapping of noisy images are also ill-posed problems due to unknown information near the borders of the filter and noise-generated inconsistencies [140].

A powerful tool for solution of such ill-posed problems is Bayesian estimation theory. The estimate is sought as the minimizer of a cost function [140] which contains data terms derived from the likelihood function and from the prior model. If the task is to estimate the function $f(\vec{r})$ on the nodes of a regular lattice $L$ from the observation data $I(\vec{r}) = Af(\vec{r}) + N(\vec{r})$, available in $\vec{r} \in S$, where $A$ is a noninvertible operator, $N$ is a random Gaussian field with variance $\sigma^2$, and $S$ is the subset of $L$, *the likelihood of* $I(\vec{r})$ *is given by* [248]:

$$P_{I|f}(f) = P_N(Af - I) = \frac{1}{K}\exp\left\{-\sum_{\vec{r}\in S}[Af(\vec{r}) - I(\vec{r})]^2/2\sigma^2\right\} \qquad (76)$$

where K is a normalization constant. A computationally efficient algorithm is possible if the prior constraints can be expressed as interactions of neighbouring pixels, i.e. if a Markov random-field model is used. Markovian prior distribution of $f(\vec{r})$ is given by the Gibbs distribution $P_f(f) = \exp\left[-\sum\limits_C V_C(f)\right] \Big/ K'$, where $K'$ is a normalization constant and the potential functions $V_C(f)$ describe the behaviour of $f(\vec{r})$ on a set of cliques that form a neighbourhood system in $L$. A clique comprises one or more sites in $L$ with any two of them being neighbours of each other. The maximum *a posteriori* estimator can be built from the posteriori distribution $P_{f|I}(f) = P_{I|f}(f)P_f(f)$ of $f(\vec{r})$ as a minimizer of the functional [248]:

$$U(\hat{f}) = \sum_{\vec{r}\in S} \Phi_{f,g}(\vec{r}) + \varepsilon \sum_C V_C(\hat{f}) \tag{77}$$

where the function $\Phi_{f,g}(\vec{r})$ depends on the observation data and the noise model. The regularization parameter $\varepsilon$ depends on the noise variance. The cost function (77) consists of data terms that ensure solution consistent with the observations and of regularization terms which take into the account some properties of the estimate. Following the natural expectation, a frequently applied constraint in the phase recovery problem is the smoothness of the phase field throughout the FP. In the case of globally smooth $f(\vec{r})$ the popular Markov random field models are the first-order (membrane) field described by the potential function $V_{ij}(f) = [f(i) - f(j)]^2$ between pairs of the nearest-neighbour sites, the second-order (thin-plate) model with the potential function $V_{ijk}(f) = [-f(i) + 2f(j) - f(k)]^2$ for three neighbouring sites, lying on a line, and the potential function associated with the sites in the corners of a rectangular $V_{ijkl}(f) = [-f(i) + f(j) - f(k) + f(l)]^2$, where $f(i) \equiv f(i\Delta_{x,y})$.

The maximum *a posteriori* estimate obtained as a result of minimization of (77) is equivalent to a low-pass linear filter acting on the pattern $I(\vec{r})$. *Such a fi*lter has the advantage to be independent on boundary conditions thus making possible to process FPs with irregular shapes, to enable recovery of missing data and to interpolate data between the lattice nodes. The regularized approach could also be applied for creation of robust non-linear filters or of quadrature filters (QFs) [249]. The frequency response of a linear QF is described by a window function $\hat{g}(\vec{\omega})$ *with* $\vec{\omega} = 2\pi\vec{f}$, *e.g. a Gaussian function as in* the case of a Gabor filter, centered at a given carrier frequency $\vec{\omega}_0 = 2\pi\vec{f}_0$ *which exceeds the spread of* $\hat{g}(\vec{\omega})$ *on the frequency axis. In the spatial domain this QF has a complex impulse response whose real and imaginary parts* $g(\vec{r})\cos(\vec{\omega}_0 \cdot \vec{r})$ *and* $g(\vec{r})\sin(\vec{\omega}_0 \cdot \vec{r})$ *respectively are connected through a Hilbert transform, where* $g(\vec{r})$ *is the inverse Fourier transform of* $\hat{g}(\vec{\omega})$. *So, if a QF is applied to* $\tilde{I}(\vec{r}) = I_V(\vec{r})\cos[\vec{\omega}_0 \cdot \vec{r} + \varphi(\vec{r})]$, *in which the phase change* $\varphi(\vec{r})$ *is small in comparison with* $\vec{\omega}_0 \cdot \vec{r}$ *and the filter window in the frequency domain covers the spectrum of* $\varphi(\vec{r})$, *the output of filter tuned at* $\vec{f}_0$ *gives the* complex signal $\tilde{I}(\vec{r}) = \frac{1}{2} I_V(\vec{r}) \exp\{j[\vec{\omega}_0 \cdot \vec{r} + \varphi(\vec{r})]\}$. *Determination of* $\varphi(\vec{r})$

*from this signal is straightforward if the requirement* $\varphi(\vec{r}) << \vec{\omega}_0 \cdot \vec{r}$ *is fulfilled.* In general, to apply the QF to $\tilde{I}(\vec{r})$ when the latter condition is not valid, one needs to know the sign of the spatial frequency $\vec{\omega} = 2\pi\vec{f}$ *at the point* $\vec{r}$ *to correct the sign of the Hilbert transform output* [250].

To extend the QF method for wideband or noisy FPs, in [251] it is proposed to apply the QF adaptively to a local part of the FP where it can be written in the form:

$$\tilde{I}(\vec{r}) = I_V(\vec{r})\cos[\varphi(\vec{r})] = I_V(\vec{r})\cos[\vec{\omega}(\vec{r})\cdot\vec{r} + \tilde{\varphi}(\vec{r})] \tag{78}$$

Such an adaptive QF can be designed using the Bayesian estimation theory, with Markov random fields as prior models, under the additional constraints that the FP is locally monochromatic and the dominant frequency $\vec{\omega}(\vec{r})$ is a smooth function across the FP. The idea is to build a complex image $\Omega(\vec{r}) = \Omega_{re}(\vec{r}) + j\Omega_{im}(\vec{r})$ as an output of the QF with a tunable frequency $\vec{\omega}(\vec{r})$. This complex image is subject to the following constraints [246]:

i) the real part $\Omega_{\mathrm{Re}}(\vec{r}) = \tilde{I}_V(\vec{r})\cos[\vec{\omega}(\vec{r})\cdot\vec{r} + \tilde{\varphi}(\vec{r})]$ is locally monochromatic, where $|\tilde{\varphi}(\vec{r})| << \omega(\vec{r})\cdot\vec{r}$; this constraint means that in the neighbouring points $\vec{s} = (x-1, y)$ or $\vec{s} = (x, y-1)$ one may write $\Omega_{\mathrm{Re}}(\vec{r}) \approx \tilde{I}_V(\vec{r})\cos[\vec{\omega}(\vec{r})\cdot\vec{s} + \tilde{\varphi}(\vec{r})]$;
ii) the imaginary part should approximate the corresponding quadrature image, i.e. $\Omega_{\mathrm{Im}}(\vec{r}) \approx \tilde{I}_V(\vec{r})\sin[\vec{\omega}(\vec{r})\cdot\vec{r} + \tilde{\varphi}(\vec{r})]$;
iii) the real part must be proportional to the observed FP, i.e. $\tilde{I}(\vec{r}) \propto I(\vec{r})$.

Thus the phase $\varphi(\vec{r})$ is determined from $\Omega(\vec{r})$. To fulfil the above constraints, the output of the filter, $\Omega(\vec{r})$, is constructed to minimize the following cost function [246]:

$$U(\Omega) = \begin{aligned}[t] &\sum_{(\vec{r},\vec{s})\in S} \left|\Omega(\vec{r}) - \Omega(\vec{s}) - 2[I(\vec{r}) - I(\vec{s})]\right|^2 + \\ &+\varepsilon \sum_{(\vec{r},\vec{s})\in S} \left|\Omega(\vec{r})\exp[-0.5j\vec{\omega}(\vec{r})\cdot(\vec{r}-\vec{s})]\right. \\ &\left.- \Omega(\vec{s})\exp[-0.5j\vec{\omega}(\vec{s})\cdot(\vec{s}-\vec{r})]\right|^2 \end{aligned} \tag{79}$$

where $(\vec{r},\vec{s}) \in S$ denotes that all nearest-neighbour pairs of sites $\vec{r}$ and $\vec{s}$ are included in the sums; $S$ is the region with available data, which in general may have an irregular shape. Each point $\vec{r} = (x, y)$ away from the borders has four nearest neighbours, which are the points $(x-1, y)$, $(x+1, y)$, $(x, y-1)$ and $(x, y+1)$. It is obvious that the first sum in the cost function controls the resemblance between the observed FP and the constructed complex image $\Omega(\vec{r})$. The value of the second sum is vanishing if the constraints i) and ii) are implemented. The parameter $\varepsilon$ controls the spectral properties of the filter. A large value of $\varepsilon$ produces a narrowband QF, which can effectively remove a signal-dependent noise [246], as is the noise caused by contrast variations or the speckle noise, without distortions of the signal. As the local frequency

$\vec{\omega}(\vec{r})$ *is also unknown, the cost function (79) must b*e modified to incorporate constraints set on the field $\vec{\omega}(\vec{r})$, *as is proposed in* [248]:

$$U'(\Omega) = U(\Omega) + \mu \left[ \sum_{[i,j,k]} V_{ijk}(\vec{\omega}) + \sum_{[i,j,k,l]} V_{ijkl}(\vec{\omega}) \right] \tag{80}$$

The minimization method proposed in [248] and characterized by the authors as computationally expensive and applicable only to low fringe densities is further improved in [246]. The idea is to build an estimate $\hat{\omega}(\vec{r}) = [\rho(\vec{r})\cos\theta(\vec{r}), \rho(\vec{r})\sin\theta(\vec{r})]$ by sequentially applying a regularization procedure to estimate the frequency vector orientation, $\theta(\vec{r})$, the frequency sign and the fringe density $\rho(\vec{r})$ at each point of the FP. The drawback of this approach is the necessity to minimize several cost functions which is a time-consuming procedure. The fringe orientation is given by the direction:

$$[\cos\theta(\vec{r}), \sin\theta(\vec{r})] \cdot \nabla\varphi(\vec{r}) = \Theta(\vec{r}) \cdot \nabla\varphi(\vec{r}) = 0 \tag{81}$$

The fringe orientation at site $\vec{r}$ is determined with $\pi$ ambiguity:

$$\theta(\vec{r}) = \tan^{-1}\left[\frac{\partial\tilde{I}(\vec{r})/\partial x}{\partial\tilde{I}(\vec{r})/\partial y}\right] \pm \frac{\pi}{2} \tag{82}$$

A $n$-dimensional quadrature transform is derived in [250] from the approximate equation

$$\nabla I(\vec{r}) \cdot \nabla\varphi(\vec{r}) \cong -I_V(\vec{r})\sin[\varphi(\vec{r})]\,|\nabla\varphi(\vec{r})|^2 \tag{83}$$

which is valid for a slowly varying contrast function $I_V(\vec{r})$ and becomes exact if the contrast of fringes is constant across the pattern. The QF is $n$-dimensional because it can be applied in the case of $\vec{r}(x_1, x_2, \ldots, x_n)$ in the form

$$Q_n\left\{I_V(\vec{r})\cos[\varphi(\vec{r})]\right\} = \vec{n}_\varphi(\vec{r}) \cdot \nabla I(\vec{r})\,|\nabla\varphi(\vec{r})|^{-1} \tag{84}$$

where $\vec{n}_\varphi(\vec{r})$ is the unit vector normal to the isophase contour at point $\vec{r}$. The performance of $Q_2$ for processing of closed FPs is compared to the vortex operator developed in [229]. Both algorithms proposed in [229] and [250] rely on two operators – an isotropic 2D Hilbert transform, and an operator which gives the orientation $2\pi$ of the fringes. Determination of the fringe orientation is more difficult task and requires a sequential approach. A regularized estimator for determination of an orientational vector field $\vec{n}_\varphi(\vec{r})$ through minimization of a cost function is proposed in [252]. It has been demonstrated in [253] that information of fringe orientation can be derived from the local gradients of the fringe intensity in a normalized FP obtained after a suitable bandpass derivative filtering. To increase the accuracy of $\theta(\vec{r})$ estimation, especially in a low modulation zones, the authors apply neighbouring-direction averaging.

An algorithm for accurate $\theta(\vec{r})$ extraction with four different derivative kernels is presented in [254].

Phase demodulation from a single FP based on phase-locked loop (PLL) has been proposed in a series of works [10, 255, 256]. The advantage of this technique is that the phase unwrapping is implicit in the PLL and, therefore, is not necessary. The principle of the PLL is well known since 1932 [257]. The output of the phase detector measures the difference between the phase of a discrete input signal and the phase of a digital controlled oscillator (DCO). From the output of the phase detector the digital filter produces a control signal which is fed into the DCO. The control signal changes the frequency of the DCO in a way to decrease the phase difference between the input signal and the DCO. If the control signal is equal to zero, the DCO generates a signal at a constant frequency which is called a free-running frequency of the DCO. In the case of phase demodulation, the PLL system locks and tracks the phase-modulated signal. The running frequency of the DCO is equal to the spatial carrier frequency of the fringes. In tracking state, the frequency of the DCO approaches the instantaneous frequency and is proportional to the control signal from the digital filter. Ideally, the control signal is a replica of the derivative of the modulating signal. A zero-order digital filter (a filter with only a proportional path) leads to a first-order digital PLL system, whereas the filter with a first-order infinite impulse response gives a second-order PLL [258]. The PLL can be applied only to open fringes. To achieve good results with the PLL, the background intensity distribution must be strongly attenuated or removed by a high-pass filter, e.g. by differentiation of the intensity distribution with respect to the $x$ coordinate. The second assumption of the PLL method is that the visibility of fringes is constant and one may set it equal to 1.0. If applied to a row in a FP, $\tilde{I}(x) = I_V(x)\cos[2\pi f_0 + \varphi(x)]$, the discretized first-order PLL system which is a nonlinear dynamic system is usually described by [259]

$$\hat{\varphi}(x+1) = \hat{\varphi}(x) + \tau\tilde{I}(x)\sin[2\pi f_0 + \hat{\varphi}(x)] \tag{85}$$

Therefore, the phase estimate, $\hat{\varphi}$, in a point $(x+1)$ is determined from the phase estimate in the previous point corrected by the term $\tau\tilde{I}(x)\sin[2\pi f_0 + \hat{\varphi}(x)]$. However, to construct the estimate an *a priori* knowledge about the spatial carrier frequency is required. In addition, the PLL system is not able to demodulate a low frequency carrier pattern modulated by a wideband signal. It may occur that the estimated phase map will be corrupted by the double fringe frequency. Another serious drawback of the first-order PLL algorithm is its low immunity to noise. To improve noise performance of the algorithm, a second-order PLL algorithm is proposed in [257]. The improved algorithm permits real time implementation; in [257] a frame rate of 25 processed frames per second is reported. However, the higher frequency disturbances of the PLL system itself are still present in the improved algorithm. The drawback of the PLL algorithms is their inability to handle FPs with rapid phase variations.

An idea to solve the phase modulation problem from the regularization point of view is realized also in the so called phase-tracking approach which gives a basis for creation of robust automatic algorithms for phase retrieval from wideband noisy FPs bounded by arbitrarily shaped pupils without any edge distortions. A regularized version of a phase-tracking detecting algorithm which can be employed for open or closed fringes is described in [30]. The regularized phase-tracking (RPT) yields a continuous phase estimate without phase unwrapping. The RPT uses a two terms cost function which implements the assumption of locally spatially monochromatic FP with smooth and continuous phase [30]:

$$\begin{aligned} U &= \sum_{x,y\in S} U_{x,y}(\hat{\varphi},\omega_x,\omega_y) \\ U_{x,y}(\varphi_0,\omega_x,\omega_y) &= \sum_{\mu,\eta\in(N_{xy}\cap S)} \Big\{[\tilde{I}(\mu,\eta)-\cos\varphi_e(x,y,\mu,\eta)]^2 \\ &\quad + \gamma[\hat{\varphi}(\mu,\eta)-\varphi_e(x,y,\mu,\eta)]^2 m(\mu,\eta)\Big\} \end{aligned} \tag{86}$$

where $\hat{\varphi}(x,y)$ is the phase estimate that minimizes the cost function, $S$ is the region occupied by the analyzed FP, $N_{xy}$ is the neighbourhood of the point of interest $(x, y)$, the term $U_{x,y}$ is the energy of the RPT system at the site $(x, y)$, $m(x,y)$ is an indicator which takes values of 1 and 0 to mark the previously used pixels. The FP $\tilde{I}(x,y)$ is obtained from $I(x, y)$ after subtraction of the background $I_B(x,y)$ and the normalization procedure $I_V(x,y)\approx 1$. The term $\varphi_e(x,y,\mu,\eta)$ is the local phase plane that is used to approximate simultaneously the observed data through a cosinusoidal model and the phase values that have already been estimated:

$$\varphi_e(x,y,\mu,\eta)=\hat{\varphi}(x,y)+\hat{\omega}_x(x,y)(x-\mu)+\hat{\omega}_y(x,y)(y-\eta) \tag{87}$$

where $\hat{\omega}_{x,y}$ (.) are the $x$- and $y$- components of the local frequency. As it can be seen, the second term in the cost function is small only if the phase estimate is very smooth. The parameter $\gamma$ controls the smoothness of the phase estimate. Due to the multimodal character of the cost function $U$, the problem of finding its global minimum is difficult and computationally expensive. To avoid this obstacle, the authors of [30] develop a sequential demodulating algorithm. The phase is calculated by a propagative scheme from pixel to pixel. To start the processing, a seed point $(x_0,y_0)$ is chosen in $S$, preferably in the region with low-frequency fringes. The function $U_{x,y}(\hat{\varphi},\hat{\omega}_x,\hat{\omega}_y)$ is optimized in the site $(x_0,y_0)$ by finding $\hat{\varphi}(x_0,y_0)$ and $\hat{\omega}_{x,y}(x_0,y_0)$, and the indicator $m(x_0,y_0)$ is set to 1 to show that this site has been already processed. By using the indicator function the other pixels are processed sequentially, and the first iteration of the estimated phase map $\hat{\varphi}^1(x,y)$ is obtained. The function $U_{x,y}(\hat{\varphi},\omega_x,\omega_y)$ is optimized in the site $(x, y)$ by using a simple gradient descent. The output of the RPT system gives the estimated phase already unwrapped. The authors investigate also another approach to refine the first iteration estimate. The latter can be used as an input to the iteration conditional mode algorithm which is designed to find a maximum *a posteriori* estimator for images that are modelled as random vector fields $\vartheta(x,y) = [\hat{\varphi}(x,y), \hat{\omega}_x(x,y), \hat{\omega}_y(x,y)]^T$ with posterior Gibbs distributions of the form $P(\vartheta) = \exp[-U(\vartheta)]/Z$, where $Z$ is a normalization constant and $U(\vartheta)$ is an energy function. The algorithm finds a local minimum of $U(\vartheta)$ with respect to $\vartheta$ at each site $(x, y)$ in a small number of steps. This shows that the RPT system can be considered as an adaptive narrowband filter. This makes the RPT more robust to noise when wideband FPs are processed. The cost function (121) ensures satisfactory results only for low noise closed fringes. To deal with a high noise level, the cost function must include an additional term. In [247] it is proposed to add a term that regularizes the requirement that a slightly phase-shifted FP should resemble the processed pattern. The authors recommend use of a constant phase shift between $0.1\pi$ and $0.3\pi$ rad; they also propose a new scanning strategy which initially demodulates pixels around the stationary points. The shortcoming of this fringe-follower regularized phase tracking is the need of low-pass filtering and a binary threshold operation.

The RPT is a local processing approach [214] in which appropriate cosine elements are fitted to the FP in a local area. Thus spatially separated signals have no influence on each other. It can be used for phase-shifted FPs, a single-carrier fringes FP, and a single closed fringe FP. In addition, the RPT shows very good behaviour close to the borders. The shortcomings are the necessity to optimize the estimates of the phase and the local frequency simultaneously, as well as the requirement to remove the background and to normalize the FP. In [40] an improved version of the RPT with a more robust minimization algorithm is used to demodulate squared-grating deflectograms. The propagative scheme of phase demodulation of open and closed fringes with introduction of a quality map is described in [260]. To avoid the necessity to normalize the FP, a modified cost function is proposed in [261] which assumes that the fringe modulation is also locally monochromatic and is described by

$$I_V^e(x,y,\mu,\eta) = I_V(x,y) + \beta_x(x,y)(x-\mu) + \beta_y(x,y)(y-\eta) \qquad (88)$$

where $\beta_{x,y}$ are the local modulation frequencies.

The RPT approach is further improved in [259] by combining quadrature estimation with the RPT. The sequential quadrature and phase tracking estimator builds the phase estimate by minimizing the following cost function:

$$\begin{aligned} U = [\tilde{I}(\vec{r}) - \cos\hat{\varphi}(\vec{r})]^2 + \left[\frac{\partial \tilde{I}(\vec{r})}{\partial x} + \hat{\omega}_x(\vec{r})\sin\hat{\varphi}(\vec{r})\right]^2 \\ + \left[\frac{\partial \tilde{I}(\vec{r})}{\partial y} + \hat{\omega}_y(\vec{r})\sin\hat{\varphi}(\vec{r})\right]^2 \end{aligned} \qquad (89)$$

The derivatives $\partial\tilde{I}(\vec{r})/\partial x$ and $\partial\tilde{I}(\vec{r})/\partial y$ are calculated from the first-order differences. The first term of the cost function tends to zero when the estimate $\hat{\varphi}(\vec{r})$ is close to $\varphi(\vec{r})$. The second term in (89) enforces the requirement on the estimates $\hat{\varphi}(\vec{r})$ and $\hat{\omega}_{x,y}(\vec{r})$ to make possible approximation of the quadrature of the signal. With this additional constraint the optimal values of $\hat{\varphi}(\vec{r})$ and $\hat{\omega}_{x,y}(\vec{r})$ are found by search along the direction of the steepest descend of the cost function [259]. The functions $\hat{\omega}_x$, $\hat{\omega}_y$, $\hat{\phi}$ are subject to optimization with initial conditions $\hat{\phi}(\vec{r}_i)^0 = \hat{\phi}(\vec{r}_{i-1})^\infty \hat{\omega}_x(\vec{r}_i)^0 = \hat{\omega}_x(\vec{r}_{i-1})^\infty \hat{\omega}_x(\vec{r}_i)^0 = \hat{\omega}_x(\vec{r}_{i-1})^\infty$, where the index $\infty$ denotes a stable pair $\hat{\phi}, (\hat{\omega}_x, \hat{\omega}_y)$ of estimates in the previous estimated site. This sequential approach evaluates the phase without phase unwrapping. The quadrature phase-tracking system can be used to demodulate open fringes without the need to know the carrier frequency, unlike the case in the PLL approach. It outperforms the PLL system also by its ability to process very low frequency fringes without worry of overlapping of low and higher frequency spectra. The quadrature phase tracking can be used to demodulate closed fringe patterns if instead of row-by-row scanning strategy one follows the path of the fringes.

The regularized techniques based on the minimization of quadratic functionals have been also applied for phase unwrapping in [217, 249]. In the proposed algorithms the smoothing regularization term serves to control interpolation (or extrapolation) especially in regions with bad data and to reduce the noise. This approach for phase unwrapping is extended to process ESPI images characterized with high level of speckle noise and phase discontinuities [262]. In [263] the authors propose to fit a global non-linear function in each pixel instead of a local plane using the genetic algorithm technique. The approach is checked for a polynomial fitting.

Phase demodulation from a single FP with open or closed fringes based on numerical correlation between the measured FP and a virtual FP is developed in [264, 265]. The recorded FP is divided into zones and in each zone the FP is approximated with parallel, inclinable, and equidistant fringes and the correlation function in the zone of interest is minimized with respect to amplitude modulation, background illumination, pitch, fringe orientation, and phase. In [264] the virtual FP is built with a sinusoidal profile whereas in [265] the approach is extended to polynomial fitting which allows for acceleration of the computation. Phase demodulation by means of a non-linear filtering method based on the theory of the Markov stochastic process is developed in [266] as a recurrence procedure under the condition of a correlated phase noise. The recurrent procedure enables real-time processing of noisy data and phase retrieval without unwrapping.

## 3 Capture of Real Objects

### 3.1 Full-field Measurement

In a simple pattern projection system only one part of the object surface is viewed both by projector and the image sensor which yields a solid angle of about $2\pi$ for reliable measurement. Measurement of surfaces with almost vertical structures as e.g. cylindrical surfaces and of front and back sides of a body requires 360 degrees of observation. In addition, effect of shadowing in objects with a strong surface tilt or distortions caused by non-linear recording due to specular reflection and diffraction at the object surface makes impossible observation within these parts of the image. To compensate for the loss of information, systems with multiple directions of illumination or observation are required. One of the main problems that should be solved for accurate performance of such a system is to make precise transformation of the coordinate systems attached to all sensors into a common global coordinate system. To determine accurately the relative orientation of the sensors, they could be fixed to mechanical devices that provide position information very precisely. Such systems are expensive and vulnerable to small angular inaccuracies that may cause large errors in coordinate calculation [267]. The matching of the point clouds obtained as a result of phase demodulation of the FPs recorded by different sensors can be done also numerically, e.g. by optimal fitting which sometimes may lead to ambiguous solutions.

To overcome most of these illumination-caused difficulties, a 3D optical sensor with a periodic illumination from at least three different directions using a telecentric projection system is described in [268]. A grating with grey code and with a sinusoidal intensity transmission is used for generation of a structured light pattern. A nearly complete 3D measurement of coordinates is realized for objects with very complex surface profiles by object rotation. The system measures the phase within a number of patches from the object surface. Determination of orientation of the patches in the space permits to match them all in a global coordinate system. In [267] the PS measurement system comprises two cameras and one projector. The cameras are calibrated by using a reference object with a large number of circular targets which is imaged by both cameras at different viewing angles. The global coordinates of the reference object are restored using photogrammetric processing.

To solve the problem with shadowing and to build a good estimator of 3D coordinates, we introduce two approaches – one with double symmetrical illumination (DSI) and the other with double symmetrical observation (DSO) of the object [25]. The DSI pattern projection system with an adjustable Michelson interferometer is presented in Fig. 17. One of the mirrors of the interferometer is attached to a PLZT for precise control of the phase step with an optoelectronic feedback. The light source is a HeNe laser with $\lambda = 632.8\,\text{nm}$. Vertical interference fringes are divided by a beam splitter into two arms (left – LA and right – RA) at equal intensity and projected onto the specimen. Two series of FPs for a 5-frames phase-stepping algorithm are recorded at two different spacings, $d_1$ and $d_2$. The angle of object illumination is $\alpha$ in both arms. A Peltier cooled CCD camera with $604 \times 288$ pixels and 8-bits grey-scale coding captures the deformed FPs. The wrapped phase maps are obtained as a difference between the calculated phase maps corresponding to $d_{1,2}$ for LA and RA illumination, respectively. The unwrapped phase maps

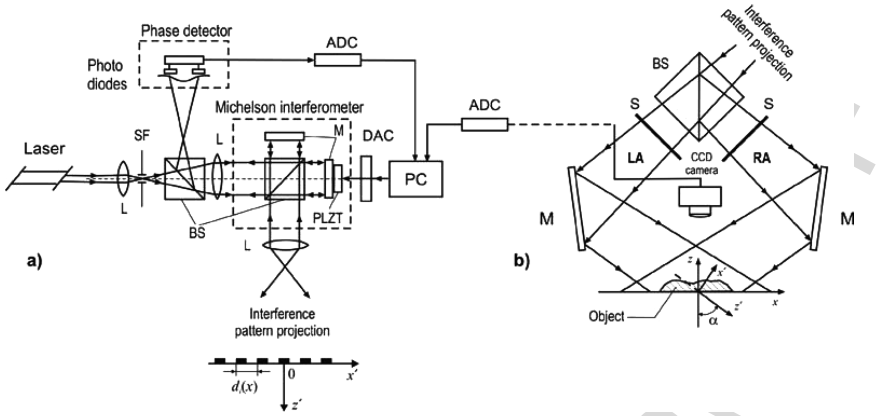

**Fig. 17.** Block diagram of DSI approach **a**) projection system **b**) optical setup for DSI, L – lens; BS – beam splitter; M – mirror; SF – spatial filter; S – shutter, PLZT – phase-stepping device

are obtained with a quality-guided path following method [123]. The pixels estimation is performed by a phase derivative variance algorithm in a $3 \times 3$ window and a quality map is produced that indicates low-quality regions. After unwrapping, a new phase map is composed, as the shadow zones from the phase map corresponding to one illumination direction are replaced and adjusted with good quality zones from the other map. The DSI approach is applied for examination of a test object (Fig. 18) and a real object (Fig. 19). The shadow zones are successfully recovered in the composed surfaces.

The DSO system is realized with Max-Zhender interferometer. The light source is an $\mathrm{Ar}^+$ laser with $\lambda = 488\,\mathrm{nm}$. Again two spacings, $d_1$ and $d_2$, and 5-frames phase-stepping algorithm are used. Two CCD cameras (resolution $604 \times 288$ pixels) positioned symmetrically capture the deformed FPs. The part of the interference pattern is reflected on the phase detector for the optoelectronic feedback. The wrapped phase maps are obtained as a difference between the calculated phase maps corresponding to $d_{1,2}$ for each point of view. The 3D distributions calculated from two observation points are transformed to a common coordinate system ($x'$, $y'$, $z'$). Figure 20 presents the experimental results for the DSO approach. The surface is successfully reconstructed, although some shadow zones are not recovered. The experimental results confirm that the increase of the angle and spacing difference ensure better sensitivity. The choice of a suitable illumination/observation angle is important to prevent partial recovery of the shadow zones and to avoid occurrence of areas that can not be observed with both CCD cameras. The real and the calculated from the measured data 3D coordinates of the test object are compared and the estimated error does not exceed ±3%.

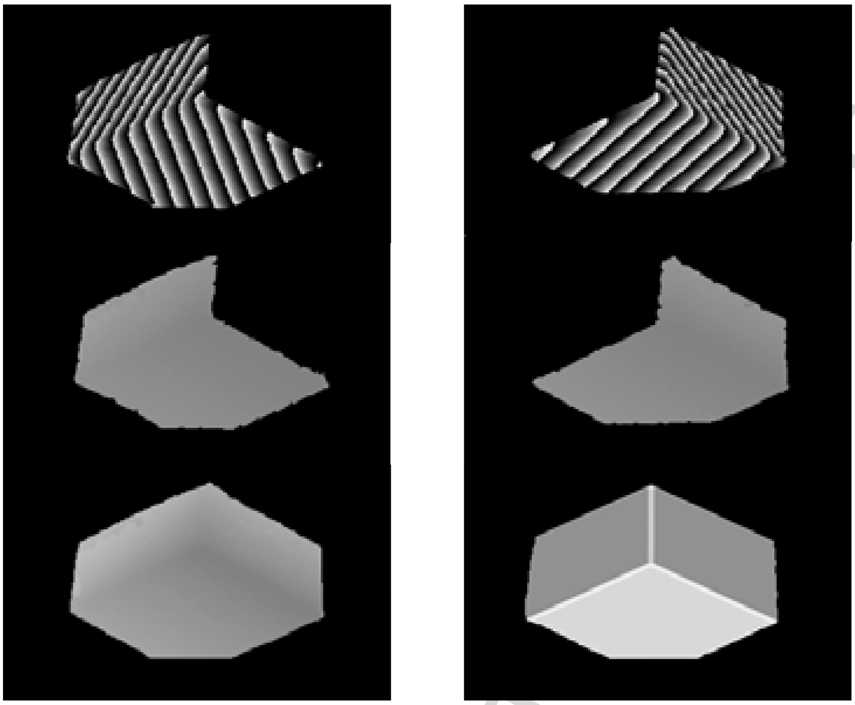

**Fig. 18.** Wrapped (**top**) and unwrapped (**middle**) phase maps and 3D visualization for DSI measurement of a test object at $d_1 = 2.3\,\mathrm{mm}$ and $d_2 = 8.5\,\mathrm{mm}$; shadow zones are masked with black colour. Left – LA direction, right – RA direction

### 3.2 Real-time Measurement

The two possible ways to realize a real-time measurement are to develop processing approaches for phase demodulation of a single pattern (single-frame or single-shot acquisition) or to record multiple patterns at high acquisition speed that are processed by the well-known phase-stepping algorithms.

As we have seen in the previous sections, during the last two decades, various methods for single frame fringe pattern demodulation have been explored. The straightforward Fourier transform phase demodulation with and without carrier fringes suffers from filtering problems caused by wideband noisy carriers and a limitation on object height variation. In addition, introduction of the carrier frequency which follows the rate of change in the observed object is not a trivial task and may require expensive equipment. The choice of filter parameters is problem dependent and requires preliminary information about the noise and bandwidth of the modulating signals. This jeopardizes automatic processing of the FPs which is one of the main requirements for realization of the capture process in a 3D dynamic display. The alternative spatial analysis method for phase retrieval from a single frame as the regularized phase

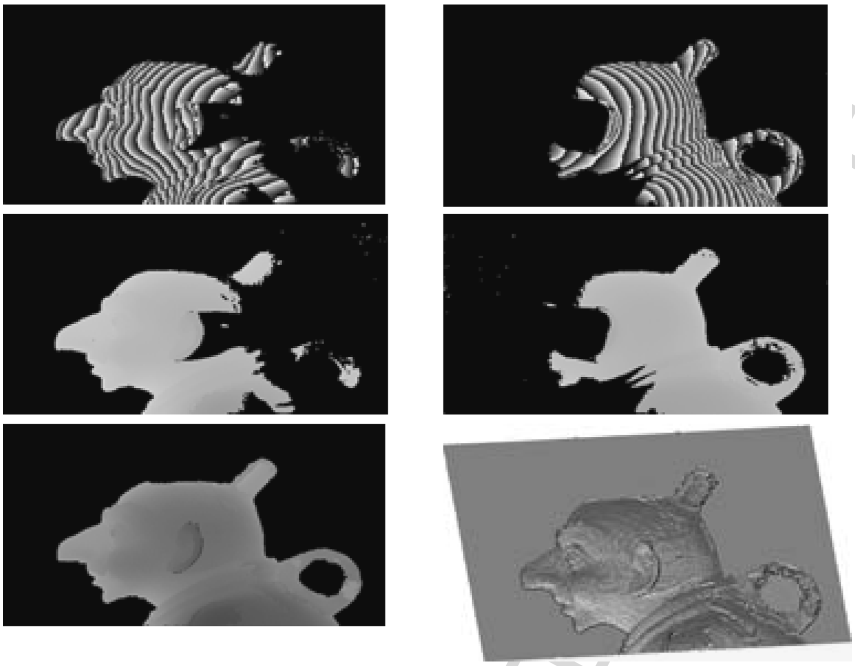

**Fig. 19.** Wrapped (**top**) and unwrapped (**middle**) phase maps and 3D visualization for SI measurement of a bronze statuette at $d_1 = 2\,\mathrm{mm}$ and $d_2 = 7.5\,\mathrm{mm}$; shadow zones are masked with black colour. Left – LA direction, right – RA direction

tracking shows high accuracy both for patterns with open and closed fringes and is capable to process noisy images with irregular shape borders. It fits local plane surfaces to the recovered phase which makes unavoidable averaging over several pixels. Due to the fact that it seeks the phase estimate through

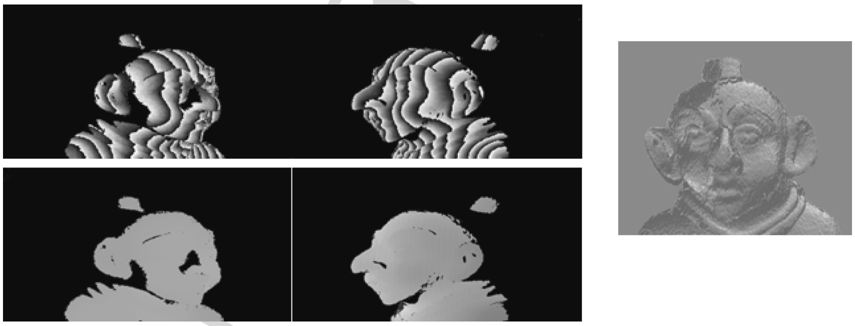

**Fig. 20.** DSO experimental results of bronze statuette measurements with periods of interference patterns $d_1 = 2\,\mathrm{mm}$ and $d_2 = 3.8\,\mathrm{mm}$; Shadow zones are masked with black colour. Wrapped phase, unwrapped phase 3D reconstruction

minimization of a cost function, this approach involves iterative solving a set of linear equations and is time-consuming. There have been developed other methods as the fitting-error modified spatial fringe modulation [78]; phase demodulation based on fringe skeletonizing when an extreme map is introduced by locating the fringes minima and maxima [187, 269, 270]; phase-stepping recovery of objects by numerical generation of multiple frames from a single recorded frame [271] or by developing a spatial modification based on assumption of slowly varying phase [272].

The main drawback of many of the spatial analysis methods is the inevitable averaging over several pixels in the neighbourhood of the point of interest which hampers investigation of high-frequency content FPs. This stimulates search and development of methods with multiple frames registration and real-time demodulation. A single-shot measurement is realized in [273] by simultaneous projection of three colour patterns (red, green and blue) on the object at different angles and Fourier analysis of the deformed image recorded by a single CCD camera. A phase-stepping method for measuring the 3-D surface profile of a moving object by projection of a sinusoidal grating pattern and continuous intensity acquisition by three phase-shifted linear array sensors positioned along the projected stripes is proposed in [274]. The method is restricted to objects moving at a constant speed. High-resolution 3D measurement of absolute coordinates using three phase-shifted fringe patterns coded with three primary colours and recorded at data acquisition speed of 90 fps is presented in [275]. Optimal intensity-modulation projection technique is proposed in [276] based on optimization procedure for rearranging the intensities in a projection pattern in order to improve detection of the stripe-order and to make possible measurement in real-time. A shadow moiré system with three TV cameras that is able to measure the shape of an object in a dynamic event is described in [66, 277]. The entries to the three cameras permit to construct a general nonlinear function of the object depth, and using Newton–Raphson method for numerical analysis to find the object profile. To improve the accuracy of the measurement, a new algorithm is proposed that takes into the account the higher harmonics in the projected FP.

The PS methodology can be applied for direct detection of the complex amplitude at the image sensor and to reconstruct the 3D image from four holograms that are sequentially recorded using reference waves phase-shifted at 0, $\pi/2$, $\pi$ and $3\pi/2$. The main advantage is the ability to register only the first-order diffracted wave. For real-time reconstruction quasi-PS digital holography is proposed by implementing a spatial division multiplexing technique. For the purpose, the digital hologram is divided into segments of $2 \times 2$ pixels. The four pixels are phase-shifted at the required phase step by numerical generation and are further extracted and relocated to construct four phase-shifted holograms. The improved reconstruction scheme of the method is described in [278]. A method for automatic phase extraction from a single pattern with closed noisy fringes based on an arccosine function is developed in [187]. To overcome phase jumps of $\pi$ and sign ambiguities, an extreme map is attached to the processed FP after adaptive weighted filtering for noise reduction and contrast enhancing. The extreme map indicates positions of fringe peaks and throughs throughout the entire area of the FP.

High-speed 3-D surface contouring by DMD projection of a colour-encoded digital FP whose RGB components comprise three phase-shifted at $2\pi/3$ FPs is tested in [279]. Using of DMD permits to enhance substantially the contrast of the projected pattern. The image deformed by the object is recorded by a colour CCD camera and sent to a computer to separate the RGB components and to create three grey-scale phase-shifted images. The intensities for the red, blue and green channels are recalculated from the recorded intensities to compensate for the coupling between the three channels. With a standard video camera, a contouring speed up to 60 frames/s can be expected. A high-speed system in which a SLM is used to generate FPs with five optimized spacings is described in [280]. To implement a four-frame algorithm 20 FPs are recorded at video rate and processed in real time using a pipeline image processor which ensures measurements of 250,000 coordinates in less than 1 s. However, the pixilated nature of the SLM restricts the measurement accuracy up to $5.10^{-4}$ from the object size [1].

A single-shot PMP system based on the PS principle can be realized by simultaneous projection of four phase-shifted at $\pi/2$ sinusoidal FPs of equal intensity, contrast and spacing that are generated at four different wavelengths. To simplify the technical solution and to have better stability, we analyze the system realization by using of sinusoidal phase diffraction gratings [27]. The FP generation module consists of 4 blocks (FPG1-4) corresponding to four different wavelengths ($\lambda_1 - \lambda_4$) as is shown in Fig. 21 left, where the FPGs are FP Generators, DLs are 20 mW CW single mode diode lasers, G1 − G4 are phase gratings. The diode lasers emit at wavelengths: $\lambda_1 = 785\,\text{nm}$, $\lambda_2 = 808\,\text{nm}$, $\lambda_2 = 830\,\text{nm}$ and $\lambda_4 = 850\,\text{nm}$. To optimize the optical efficiency of wavelength mixing, the interference mirrors (IM1 − 3) are used as follows: the mirror IM1 transmitting $\lambda_1$, $\lambda_2$ and reflecting $\lambda_3$, $\lambda_4$; the mirror IM2 transmitting $\lambda_1$ and reflecting $\lambda_2$ and the mirror IM3 transmitting $\lambda_3$ and reflecting $\lambda_4$. The registration module (Fig. 21 right) consists of four synchronized CCD cameras. The spectral separation of the individual FPs is provided by a second set of mirrors IM1–3. The precise positioning and adjustments of cameras and optical elements ensure parallel recording of the FPs.

The proposed four-wavelength system relies on the independence of the spatial period of the the Fresnel diffraction pattern created by a sinusoidal phase grating with transmittance [281] $t(x, y) = \exp[im \sin(2\pi x/d)]$, where $m$ is the modulation parameter and $d$ is the spatial grating period along the $x$ axis, on the wavelength. At plane wave illumination, the complex amplitude at distance $z$ behind the grating is a structure periodical along $x$ and $z$:

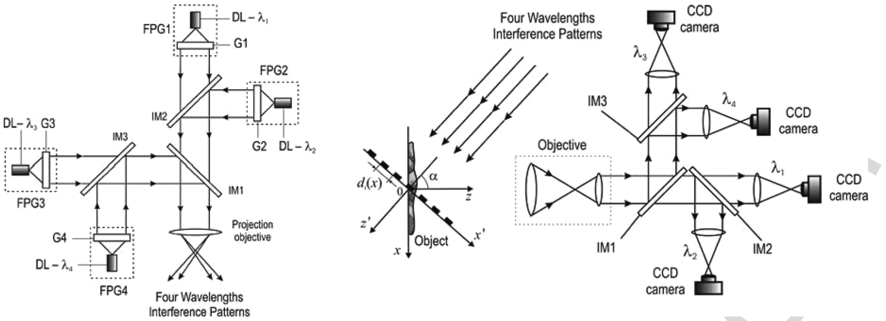

**Fig. 21.** Optical arrangement of the four-wavelengths PMP system: left) FP generation module right) registration module

$$
\begin{aligned}
U(x,y,z) = {} & J_0(m) + 2\sum_{q=0}^{\infty}\{J_{2q}(m)\cos[4q\pi x/d] \\
& \times\left\{\cos[(2q)^2\pi\lambda z/d^2] - i\sin[(2q)^2\pi\lambda z/d^2]\right\} + \\
& + iJ_{2q+1}(m)\sin[(2q+1)2\pi x/d] \\
& \times\left\{\cos[(2q+1)^2\pi\lambda z/d^2] - i\sin[(2q+1)^2\pi\lambda z/d^2]\right\}\}
\end{aligned}
\tag{90}
$$

The $y$-axis is parallel to the fringes, $J_q$ is the Bessel function of the order $q$ and $\lambda$ is the wavelength. By a proper choice of $m$, the influence of higher diffraction orders could be minimized. Figure 22 shows intensity distribution behind the phase grating ($z = 0.1\,\mathrm{m}$) at $m = 3$ and $d = 0.4\,\mathrm{mm}$ as a function of the

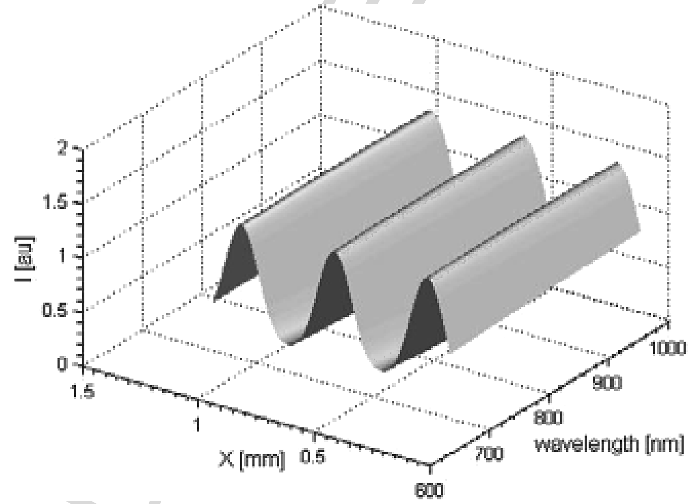

**Fig. 22.** Intensity distribution behind a phase grating in a plane parallel to its surface as a function of the wavelength

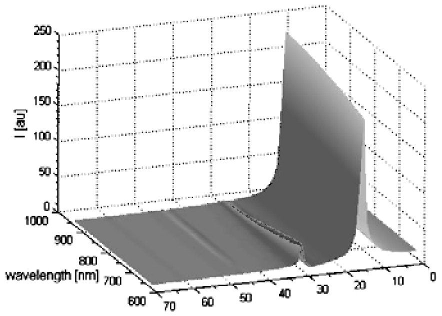

**Fig. 23.** Fourier spectrum of the intensity distribution in Fig. 27 (the zero-term is excluded)

wavelength whereas Fig. 23 depicts the corresponding Fourier spectrum. As it can be seen, the projected FP is practically with an identical sinusoidal profile for the chosen spectral region from 785 nm to 850 nm, i.e the degrading effect of the higher frequency components is overcome. The requirement for close location along $z$ of the Talbot planes corresponding to the four wavelengths is also fulfilled. These features of the used sinusoidal phase gratings are the most important for realization of real time operating PMP system for 3D coordinate measurement of dynamic scenes.

## References

1. Chen F, Brown GM, Song M (2000) Overview of Three-Dimensional Shape Measurement Using Optical Methods. Opt Eng 39: 10–22
2. Tiziani H-J (1993) Optical techniques for shape measurements. In: Juptner W, Osten W (eds) Fringe'93. Akademie, Berlin, pp. 165–174
3. Sainov V, Stoilov G, Tonchev D et al. (1996) Shape and Normal Displacement Measurement of Real Objects in a Wide Dynamic Range. In: Optical Metrology. Akad. Verlag, pp. 52–60.
4. Xie H, Liu Z, Fang D et al. (2004) A study on the digital nano-moiré method and its phase shifting technique. Meas Sci Technol 15: 1716–1721
5. Harizanova J (2006) Holographic and digital methods for recording and processing of information for cultural heritage protection. Ph.D. thesis, CLOSPI-BAS
6. Li J, Hassebrook L, Guan C (2003) Optimized two-frequency phase-measuring profilometry light-sensor temporal-noise sensitivity. J Opt Soc Am A 20: 106–115
7. Sansoni G, Corini S, Lazzari S et al. (1997) Three-dimensional imaging based on Gray-code light projection: characterization of the measuring algorithm and development of a measuring system for industrial applications. Appl Opt 36: 4463–4472
8. Pages J, Salvi J, Garcia R et al. (2003) Overview of Coded Light Projection Techniques for Automatic 3D Profiling. In: Proc IEEE, Intl. Conf. on Robotics & Automation, pp. 133–138.

9. Xian T, Su X (2001) Area modulation grating for sinusoidal structure illumination on phase-measuring profilometry. Appl Opt 40: 1201–1208
10. Gurov I., Hlubina P, Chugunov V (2003) Evaluation of spectral modulated interferograms using a Fourier transform and the iterative phase-locked loop method. Meas Sci Technol 14: 122–130
11. Baumbach T, Osten W, von Kopylow C.et al. (2006) Remote metrology by comparative digital holography. Appl Opt 45: 925–934
12. Su W, Shi K, Liu Z et al. (2005) A large-depth-of-field projected fringe profilometry using supercontinuum light illumination. Opt Express 13: 1025–1032
13. Xue L, Su X (2001) Phase-unwrapping algorithm based on frequency analysis for measurement of a complex object by the phase measuring profilometry method. Appl Opt 40: 1207–1216
14. Schirripa-Spagnolo G, Ambrosini D (2001) Surface contouring by diffractive optical element-based fringe projection. Meas Sci Technol 12: N6–N8
15. Quan C, He XY, Wang CF et al. (2001) Shape measurement of small objects using LCD fringe projection with phase-shifting. Opt Commun 189: 21–29
16. Quan C, Tay CJ, Kang X et al. (2003) Shape measurement by use of liquid-crystal display fringe projection with two-step phase shifting. Appl Opt 42: 2329–2335
17. Huang P, Zhang C, Chiang F-P (2003) High-speed 3-D shape measurement based on digital fringe projection. Opt Eng 42: 163–168
18. Sitnik R, Kujavinska M, Wonznicki J (2002) Digital Fringe Projection System for Large-Vol. 360 deg Shape Measurement. Opt Eng 41: 443–449
19. Sitnik R, Kujavinska M (2000) Opto-numerical methods for data acquisition for computer graphics and animation systems. In: Proc. SPIE 3958, pp. 36–45
20. Saldner H, Huntley J (1997) Profilometry using temporal phase unwrapping and a spatial light modulator-based fringe projector. Opt Eng 36: 610–615
21. Mehta D, Dubey S, Hossain M et al. (2005) Simple multifrequency and phase-shifting fringe-projection system based on two-wavelength lateral shearing interferometry for three-dimensional profilometry. Appl Opt 44: 7515–7521
22. Chen L-C, Huang C-C (2005) Miniaturized 3D surface profilometer using digital fringe projection. Meas Sci Technol 16: 1061–1068
23. Chen L-C, Liao C-C (2005) Calibration of 3D surface profilometry using digital fringe projection. Meas Sci Technol 16: 1554–1566
24. Harizanova J, Sainov V (2006) Three-Dimensional Profilometry by Symmetrical Fringes Projection Technique. Opt Las Eng 44: 1270–1282
25. Harizanova J, Kolev A (2005) Comperative study of fringes generation in two-spacing phase-shifting profilometry. In: Proc. SPIE 6252, pp. 21–25
26. Sainov V, Stoykova E, Harizanova J (2006) Real Time Phase Stepping Pattern Projection Profilometry. In: Proc. SPIE 6341, pp. 63410P–63411/63416
27. Quan C, Tay C, Chen L (2005) Fringe-density estimation by continuous wavelet transform. Appl Opt 44: 2359–2365
28. Meadows D, Johnson W, Allen J (1970) Generation of surface contours by moiré patterns. Appl Opt 9: 942–947
29. Dorrio B, Fernandez J (1999) Phase-evaluation methods in whole-field optical measurement techniques. Meas Sci Technol 10: R33–R55
30. Servin M, Marroquin JL, Cuevas FJ (1997) Demodulation of a single interferogram by use of a two-dimensional regularized phase-tracking technique. Appl Opt 36: 4540–4548

31. Wang Z, Ma H (2006) Advanced continuous wavelet transform algorithm for digital interferogram analysis and processing. Opt Eng 45: 045601
32. Yamaguchi I, Yamamoto A, Yano M (2000) Surface topography by wavelength scanning interferometry. Opt Eng 39: 40–46
33. Guo H, He H, Yu Y et al. (2005) Least-squares calibration method for fringe projection profilometry. Opt Eng 44: 033603
34. Skydan O, Lalor M, Burton D (2005) Three-dimensional shape measurement of non-full-field reflective surfaces. Appl Opt 44: 4745–4752
35. Hu Q, Harding K (2007) Conversion from phase map to coordinate: Comparison among spatial carrier, Fourier transform, and phase shifting methods. Opt Las Eng 45: 342–348
36. Cuevas FJ, Servin M, Stavroudis O et al. (2000) Multi-layer neural network applied to phase and depth recovery from fringe patterns. Opt Commun 181: 239–259
37. Huang P, Hu Q, Chiang F-P (2003) Error compensation for a three-dimensional shape measurement system. Opt Eng 42: 482–486
38. Yu F, Wang E (1973) Speckle reduction in holography by means of random spatial sampling. Appl Opt 12: 1656–1659
39. Liu H, Lu G, Wu S et al. (1999) Speckle-induced phase error in laser-based phaseshifting projected fringe profilometry. J Opt Soc Am A 16: 1484–1495
40. Berryman F, Pynsent P, Cubillo J (2003) A theoretical comparison of three fringe analysis methods for determining the three-dimensional shape of an object in the presence of noise. Opt Las Eng 39: 35–50
41. Lei Z, Kang Y, Yun D (2004) A numerical comparison of real-time phase-shifting algorithms. Opt Las Eng 42: 395–401
42. Bitou Y (2003) Digital phase-shifting interferometer with an electrically addressed liquid-crystal spatial light modulator. Opt Lett 28: 1576–1578
43. Patil A, Langoju R, Rastogi P (2004) An integral approach to phase shifting interferometry using a super-resolution, frequency estimation method. Opt Express 12: 4681–4697
44. Kreis T (2004) Handbook of Holographic Interferometry. Wiley-VCH GmbH, Weinheim.
45. Li W, Su X (2001) Real-time calibration algorithm for phase shifting in phase-measuring philometry. Opt Eng 40: 761–766
46. Rathjen C (1995) Statistical properties of phase-shift algorithms. J Opt Soc Am A 12: 1997–2008
47. Morgan C (1982) Least-squares estimation in phase-measurement interferometry. Opt Lett 7: 368–370
48. Greivenkamp J (1984) Generalized data reduction for heterodyne interferometry. Opt Eng 23: 350–352
49. Hibino K (1997) Susceptibility of systematic error-compensating algorithms to random noise in phase-shifting interferometry. Appl Opt 36: 2084–2093
50. Ding X, Cloud G, Raju B (2005) Noise tolerance of the improved max-min scanning method for phase determination. Opt Eng 44: 035605–035607
51. Gutmann B, Weber H (1998) Phase-shifter calibration and error detection in phase-shifting applications: a new method. Appl Opt 37: 7624–7631
52. Ishii Y, Chen J, Murata K (1987) Digital phase-measuring interferometry with a tunable laser diode. Opt Lett 12: 233–235
53. Ishii Y (1999) Wavelength-tunable laser-diode interferometer. Opt Rev 6: 273–283

54. Zhang C, Huang PS, Chiang F (2002) Microscopic phase-shifting profilometry based on digital micromirror device technology. Appl Opt 41: 5896–5904
55. Creath K (1988) Phase-measurement interferometry techniques. Prog Opt 26: 349–393
56. Schwider J (1990) Advanced evaluation techniques in interferometry. Prog Opt 28: 271–359
57. Van Wingerden J, Frankena HJ, Smorenburg C (1991) Linear approximation for measurement errors in phase shifting interferometry. Appl Opt 30: 2718–2729
58. Ahmad F, Lozovskiy V, Castellane R (2005) Interferometric phase estimation through a feedback loop technique. Opt Commun 251: 51–58
59. Li Y, Zhu Z, Li X (2005) Elimination of reference phase errors in phase-shifting interferometry. Meas Sci Technol 16: 1335–1340
60. Schwider J, Dresel T, Manzke B (1999) Some considerations of reduction of reference phase error in phase stepping interferometry. Appl Opt 38: 655–659
61. Arai Y, Yokozeki S (1999) Improvement of measurement accuracy in shadow moire' by considering the influence of harmonics in the moiré profile. Appl Opt 38: 3503–3507
62. Koliopoulos C (1981) Interferometric optical phase measurement techniques. Ph.D. Thesis, University of Arizona, Source: Dissertation Abstracts International, Vol: 42-08, Section: B, p. 3319
63. Brophy C (1990) Effect of intensity error correlation on the computed phase of phase-shifting interferometry. J Opt Soc Am A 7: 537–541
64. Zhao B, Surrel Y (1997) Effect of quantization error on the computed phase of phase-shifting measurements. Appl Opt 36: 2070–2075
65. Zhao B (1997) A statistical method for fringe intensity-correlated error in phase-shifting measurement: the effect of quantization error on the N-bucket algorithm. Meas Sci Technol 8: 147–153
66. Surrel Y (1996) Design of Algorithms for Phase Measurements by the Use of Phase Stepping. Appl Opt 35: 51–60
67. Skydan O, Lilley F, Lalor M et al. (2003) Quantization error of CCD cameras and their influence on phase calculation in fringe pattern analysis. Appl Opt 42: 5302–5307
68. Wizinowich P (1990) Phase-shifting interferometry in the presence of vibration: a new algorithm and system. Appl Opt 29: 3271–3279
69. De Groot P (1995) Vibration in Phase-Shifting Interferometry. J Opt Soc Am A 12: 354–365
70. De Groot P, Deck L (1996) Numerical simulations of vibration in phase-shifting interferometry. Appl Opt 35: 2172–2178
71. Ding X, Cloud G, Raju B (2004) Improved signal processing algorithm for the max-min scanning method for phase determination. Opt Eng 43: 63–68
72. Strobel B (1996) Processing of interferometric phase maps as complex-valued phasor images. Appl Opt 35: 2192–2198
73. Quan C, Tay C, Chen L et al. (2003) Spatial-fringe-modulation-based quality map for phase unwrapping. Appl Opt 42: 7060–7065
74. Cheng Y, Wyant J (1985) Phase-shifter calibration in phase-shifting interferometry. Appl Opt 24: 3049–3052
75. Hibino K, Oreb B, Farrant D et al. (1997) Phase-shifting algorithms for nonlinear and spatially nonuniform phase shifts. J Opt Soc Am A 14: 918–930

76. Schmit J, Creath K (1995) Extended averaging technique for derivation of error-compensating algorithms in phase-shifting interferometry. Appl Opt 34: 3610–3619
77. Afifi M, Nassim K, Rachafi S (2001) Five-frame phase-shifting algorithm insensitive to diode laser power variation. Opt Commun 197: 37–42
78. Hariharan P, Oreb B, Eiju T (1987) Digital phase-shifting interferometry: a simple error compensating phase calculation algorithm. Appl Opt 26: 2504–2505
79. Schwider J, Falkenstorfer O, Schreiber H et al. (1993) New Compensating Four-Phase Algorithm for Phase-Shift Interferometry. Opt Eng 32: 1883–1885
80. De Groot P (1995) Derivation of algorithms for phase-shifting interferometry using the concept of a data-sampling window. Appl Opt 34: 4723–4730
81. Zhang H, Lalor M, Burton DR (1999) Error-compensating algorithms in phase-shifting interferometry: a comparison by error analysis. Opt Las Eng 31: 381–400
82. Zhao B, Surrel Y (1995) Phase-shifting: six-sample self-calibrating algorithm insensitive to the second harmonic in the fringe signal. Opt Eng 34: 2821–2822
83. Dobroiuy A, Logofatu P, Apostol D et al. (1997) Statistical self-calibrating algorithm for three-sample phase-shift interferometry. Meas Sci Technol 8: 738–745
84. Dobroiuy A, Apostol D, Nascov V et al. (1998) Self-calibrating algorithm for three-sample phase-shift interferometry by contrast leveling. Meas Sci Technol 9: 744–750
85. Zhu Y, Gemma T (2001) Method for designing error-compensating phase-calculation algorithms for phase shifting interferometry. Appl Opt 40: 4540–4546
86. Styk A, Patorski K (2007) Identification of nonlinear recording error in phase shifting interferometry. Opt Las Eng 45: 265–273
87. Chen M, Guo H, Wei C (2000) Algorithm immune to tilt phase-shifting error for phase-shifting interferometers. Appl Opt 39: 3894–3898
88. Guo H, Chen M (2005) Least-squares algorithm for phase-stepping interferometry with an unknown relative step. Appl Opt 44: 4854–4859
89. Brug H (1999) Phase-step calibration for phase-stepped interferometry. Appl Opt 38: 3549–3555
90. Patil A, Rastogi P (2005) Approaches in generalized phase shifting interferometry. Opt Las Eng 43: 475–490
91. Perry K, McKelvie J (1995) Reference phase shift determination in phase shifting interferometry. Opt Las Eng 22: 77–90
92. Carré P (1966) Installation et utilisation du comparateur photoelectrique et interferentiel du Bureau International des Poids et Mesures. Metrologia 2: 13–23
93. Freischlad K, Koliopoulos C (1990) Fourier description of digital phase-measuring interferometry. J Opt Soc Am A 7: 542–551
94. Kemao Q, Fangjun S, Xiaoping W (2000) Determination of the best phase step of the Carr'e algorithm in phase shifting interferometry. Meas Sci Technol 11: 1220–1223
95. Stoilov G, Dragostinov T (1997) Phase-stepping interferometry: five-frame algorithm with an arbitrary step. Opt Las Eng 28: 61–69
96. Kreis T (1993) Computer aided evaluation of fringe patterns. Opt Eng 19: 221–240

97. De Lega XC, Jacquot P (1996) Deformation measurement with object-induced dynamic phase shifting. Appl Opt 35: 5115–5120
98. Lai G, Yatagai T (1991) Generalized phase-shifting interferometry. J Opt Soc Am A 8: 822–827
99. Kinnstaetter I, Lohmann A, Schwider J et al. (1988) Accuracy of phase shifting interferometry. Appl Opt 27: 5082–5087
100. Wei C, Wang Z (1999) General phase-stepping algorithms with automatic calibration of Phase Steps. Opt Eng 38: 1357–1360
101. Chen X, Gramaglia M, and Yeazell J (2000) Phase-shift calibration algorithm for phase-shifting interferometry. J Opt Soc Am A 17: 2061–2066
102. Goldberg K, Bokor J (2001) Fourier-transform method of phase-shift determination. Appl Opt 40: 2886–2894
103. Guo C, Rong Z, He J et al. (2003) Determination of global phase shifts between interferograms by use of an energy-minimum algorithm. Appl Opt 42: 6514–6519
104. Marroquin J, Servin M, Rodriguez-Vera R (1998) Adaptive quadrature filters for multiple phase-stepping images. Opt Las Eng 23: 238–240
105. Patil A, Rastogi P, Raphael B (2005) Phase-shifting interferometry by a covariance-based method. Appl Opt 44: 5778–5785
106. Okada K, Sato A, Tsujiuchi J (1991) Simultaneous calculation of phase distribution and scanning phase shift in phase shifting interferometry. Opt Commun 84: 118–124
107. Cai LZ, Liu Q, Yang XL (2003) Phase-shift extraction and wave-front reconstruction in phase-shifting interferometry with arbitrary phase steps. Opt Lett 28: 1808–1810
108. Guo H, Zhao Z, Chen M (2007) Efficient iterative algorithm for phase-shifting interferometry. Opt Las Eng 45: 281–292
109. Kim S-W, Kang M-G, Han G-S (1997) Accelerated phase-measuring algorithm of least squares for phase-shifting interferometry. Opt Eng 36: 3101–3106
110. Han G-S, Kim S-W (1994) Numerical correction of reference phases in phase-shifting interferometry by iterative least-squares fitting. Appl Opt 33: 7321–7325
111. Wang Z, Han B (2004) Advanced iterative algorithm for phase extraction of randomly phase-shifted interferograms. Opt Lett 29: 1671–1674
112. Wang Z, Han B (2007) Advanced iterative algorithm for randomly phase-shifted interferograms with intra- and inter-frame intensity variations. Opt Las Eng 45: 274–280
113. Yun H, Hong C (2005) Interframe intensity correlation matrix for self-calibration in phase-shifting interferometry. Appl Opt 44: 4860–4870
114. Cai LZ, Liu Q, Yang XL (2004) Generalized phase-shifting interferometry with arbitrary unknown phase steps for diffraction objects. Opt Lett 29: 183–185
115. Qian K, Soon S, Asundi A (2004) Calibration of phase shift from two fringe patterns. Meas Sci Technol 15: 2142–2144
116. Patil A, Rastogi P (2005) Rotational invariance approach for the evaluation of multiple phases in interferometry in the presence of nonsinusoidal waveforms and noise. J Opt Soc Am A 22: 1918–1929
117. Patil A, Langoju R, Rastogi P (2007) Phase-shifting interferometry using a robust parameter estimation method. Opt Las Eng 45: 293–297

118. Gorecki C (1992) Interferogram analysis using a Fourier transform method for automatic 3D surface measurement. Pure Appl Opt 1: 103–110
119. Baldi A (2003) Phase unwrapping by region growing. Appl Opt 42: 2498–2505
120. Meneses J, Gharbi T, Humbert P (2005) Phase-unwrapping algorithm for images with high noise content based on a local histogram. Appl Opt 44: 1207–1215
121. Herraez MA, Gdeisat MA, Burton DR et al. (2002) Robust, fast, and effective two-dimensional automatic phase unwrapping algorithm based on image decomposition. Appl Opt 41: 7445–7455
122. Schofield MA, Zhu Y (2003) Fast phase unwrapping algorithm for interferometric applications. Opt Lett 28: 1194–1196
123. Ghiglia DC, Pritt MD (1998) Two-Dimensional Phase Unwrapping. J. Wiley&Sons
124. Arines J (2003) Least-squares modal estimation of wrapped phases: application to phase unwrapping. Appl Opt 42: 3373–3378
125. Baldi A (2001) Two-dimensional phase unwrapping by quad-tree decomposition. Appl Opt 40: 1187–1194
126. Baldi A, Bertolino F, Ginesu F (2002) On the performance of some unwrapping algorithms. Opt Las Eng 37: 313–330
127. Takajo H, Takahashi T (1988) Noniterative method for obtaining the exact solution for the normal equation in least-squares phase estimation from the phase difference. J Opt Soc Am A 5: 1818–1827
128. Hung KM, Yamada T (1998) Phase unwrapping by regions using least-squares approach. Opt Eng 37: 2965–2970
129. Pritt MD, Shipman JS (1994) Least-squares two-dimensional phase unwrapping using FFTs," IEEE Trans on Geoscience and Remote Sensing 11: 706–708
130. Ghiglia DC, Romero LA (1996) Mimimum $L^P$-norm two-dimensional phase unwrapping. J Opt Soc Am A 13: 1–15
131. Marroquin JL, Rivera M, Botello S et al. (1999) Regularization methods for processing fringe-pattern images. Appl Opt 38: 788–794
132. Lyuboshenko I, Maitre H, Maruani A (2002) Least-mean-squares phase unwrapping by use of an incomplete set of residue branch cuts. Appl Opt 41: 2129–2148
133. He X, Kang X, Tay C et al. (2002) Proposed algorithm for phase unwrapping. Appl Opt 41: 7422–7428
134. Herraez MA, Burton DR, Lalor MJ et al. (2002) Fast two-dimensional phase-unwrapping algorithm based on sorting by reliability following a noncontinuous path. Appl Opt 41: 7437–7444
135. Stephenson P, Burton DR, Lalor MJ (1994) Data validation techniques in a tiled phase unwrapping algorithm. Opt Eng 33: 3703–3708
136. Geldorf J (1987) Phase unwrapping by regions. In: Proc. SPIE 818, pp. 2–9
137. Huntley JM, Saldner H (1993) Temporal phase-unwrapping algorithm for automated interferogram analysis. Appl Opt 32: 3047–3052
138. Huang MJ (2002) A quasi-one-frame phase-unwrapping algorithm through zone-switching and zone-shifting hybrid implementation. Opt Commun 210: 187–200
139. Qiu W, Kang Y, Qin Q et al. (2006) Regional identification, partition, and integral phase unwrapping method for processing moiré interferometry images. Appl Opt 45: 6551–6559

140. Huang MJ, He Z (2002) Phase unwrapping through region-referenced algorithm and window-patching method. Opt. Commun 203: 225–241
141. Robinson DW (1993), In: Raed CR, Robinson DW (eds) Interferogram Analysis: Digital Fringe Pattern Measurement Techniques, Institute of Physics Publishing, Bristol, pp. 192–229
142. Oppenheim AV, Schafer RW (1975) Digital Signal Processing, Prentice Hall
143. Goldstein RM, Zebker HA, Werner CL (1988) Satellite radar interferometry: two-dimensional phase unwrapping. Rad. Scien. 23: 713–720
144. Cusack R, Huntley JM, Goldrein HT (1995) Improved Noise-Immune Phase-Unwrapping Algorithm. Appl. Opt. 34: 781–789
145. Chen CW, Zebker HA (2000) Network approaches to twodimensional phase unwrapping: intractability and two new algorithms. J Opt Soc Am A 14: 401–414
146. Bone DJ (1991) Fourier Fringe Analysis: The Two-Dimentional Phase-Unwrapping Problem. Appl Opt 30: 3627–3662
147. Quiroga JA, Gonzalez-Cano A, Bernabeu E (1995) Stablemarriage algorithm for preprocessing phase maps with discontinuity sources. Appl Opt 34: 5029–5038
148. Lim H, Xu W, Huang X (1995) Two new practical methods for phase unwrapping. In Proc. Intl. Geoscience and Remote Sensing Symp. N.J., IEEE, pp. 196–198
149. Gao Y, Liu X (2002) Noise immune unwrapping based on phase statistics and self-calibration. Opt Las Eng 38: 439–459
150. Roth M (1995) Phase Unwrapping for Interferometric SAR by the Least-Error Path. In: Technical Memorandum F1B0-95U-019 (JHU/APL, Laurel, MD)
151. Lu Y, Wang X, Zhang X (2007) Weighted least-squares phase unwrapping algorithm based on derivative variance correlation map. Optik 118: 62–66
152. Pritt MD (1996) Phase unwrapping by means of multigrid techniques for interferometric SAR. IEEE Trans. Geosci. Remote Sess. 34: 728–738
153. Li W, Su XY (2002) Phase unwrapping algorithm based on phase fitting reliability in structured light projection. Opt Eng 41: 1365–1372
154. Huntley JM, Saldner H (1993) Temporal phase-unwrapping algorithm for automated interferogram analysis. Appl Opt 32: 3047–3052
155. Saldner H, Huntley J (1997) Temporal phase unwrapping: application to surface profiling of discontinuous objects. Appl Opt 36: 2770–2775
156. Huntley JM, Saldner HO (1997) Error-Reduction Methods for Shape Measurements by Temporal Phase Unwrapping. J Opt Soc Am A 14: 3188–3196
157. Huntley JM, Saldner HO (1997) Shape Measurement by Temporal Phase Unwrapping: Comparison of Unwrapping Algorithms. Meas Sci Technol 8: 986–992
158. Zhao H, Chen W, Tan Y (1994) Phase-unwrapping algorithm for the measurement of three-dimensional object shapes. Appl Opt 33: 4497–4500
159. Nadeborn W, Andra P, Osten W (1996) A robust procedure for absolute phase measurement. Opt Las Eng 24: 245–260
160. Pedrini G, Alexeenko I, Osten W et al. (2003) Temporal phase unwrapping of digital hologram sequences. Appl Opt 42: 5846–5854
161. Sansoni G, Redaelli E (2005) A 3D vision system based on one-shot projection and phase demodulation for fast profilometry. Meas Sci Tech 16: 1109–1118
162. Hao Y, Zhao Y, Li D (1999) Multifrequency grating projection profilometry based on the nonlinear excess fraction method. Appl Opt 38: 4106–4111

163. Gilbert B, Blatt J (2000) Enhanced three-dimensional reconstruction of surfaces using multicolor gratings. Opt Eng 39: 52–60
164. Wagner C, Osten W, Seebacher S (1999) Direct shape measurement by digital wavefront reconstruction and multiwavelength contouring. Opt Eng 39: 79–85
165. Paez G, Strojnik M (1999) Phase-shifted interferometry without phase unwrapping: reconstruction of a decentered wave front. J Opt Soc Am A 16: 475–480
166. Fang Q, Zheng S (1997) Linearly coded profilometry. Appl Opt 36: 2401–2407
167. Sainov V, Harizanova J, Stoilov G et al. (2000) Relative and Absolute Coordinates Measurement by Phase-Stepping Laser Interferometry. In: Optics and Lasers in Biomedicine and Culture, Springer, pp. 50–53
168. Sainov V, Harizanova J, Shulev A (2003) Two-wavelength and two-spacing projection interferometry for real objects contouring. In: Proc. SPIE 5226, pp. 184–188
169. Sainov V, Stoykova E, Harizanova J (2006) Optical Methods for Contouring and Shape Measurement. In: Proc. ICO'06, Opto-informating &Information Photonics. St. Petersburg, Russia, pp. 130–132
170. Takeda M, Ina H, Kobayashi S (1982) Fourier-transform method of fringe-pattern analysis for computer-based tomography and interferometry. J Opt Soc Am A 72: 156–160
171. Takeda M, Mutoh K (1983) Fourier transform profilometry for the automatic measurement 3-D object shapes. Appl Opt 22: 3977–3982.
172. Kostianovski S, Lipson S, Ribak E (1993) Interference microscopy and Fourier fringe analysis applied to measuring the spatial refractive-index distribution. Appl Opt 32: 4744–4750
173. Ge Z, Kobayashi F, Matsuda S et al. (2001) Coordinate transform technique for closed-fringe analysis by the Fourier-transform method. Appl Opt 40: 1649–1657
174. Roddier C, Roddier F (1987) Interferogram analysis using Fourier transform techniques Appl Opt 26: 1668–1673
175. Bone DJ, Bachor HA, Sandeman R (1986) Fringe pattern analysis using a 2-D Fourier transform Appl Opt 25: 1653–1660
176. Kreis T (1986) Digital holographic interference phase measurement using the Fourier-transform method. J Opt Soc Am A 3: 847–856
177. Sciammarella CA (2000) Computer-assisted holographic moiré contouring. Opt Eng 39: 99–105
178. D'Acquisto L, Fratini L, Siddiolo AM (2002) A Modified Moire Technique for Three-Dimensional Surface Topography. Meas Sci Technol 13: 613–622
179. Macy W (1983) Two-dimensional Fringe-Pattern Analysis. Appl Opt 22: 3898–3901
180. Nugent K (1985) Interferogram analysis using an accurate fully automatic algorithm. Appl Opt 24: 3101–3105
181. Liu J, Ronney P (1997) Modified Fourier transform method for interferogram fringe pattern analysis. Appl Opt 36: 6231–6241
182. Burton D, Goodall A, Atkinson J et al. (1995) The Use of Carrier Frequency Shifting for the Elimination of Phase Discontinuities in Fourier Transform Profilometry. Opt Las Eng 23: 245–257
183. Su X, Chen W (2001) Fourier transform profilometry: a review. Opt Las Eng 35: 263–284

184. De Nicola S, Ferraro P, Gurov I et al. (2000) Fringe analysis for moiré interferometry by modification of the local intensity histogram and use of a two-dimensional Fourier transform method. Meas Sci Technol 11: 1328–1334
185. Srinivasan V, Liu HC, Halioua M (1984) Automated phase-measuring profilometry of 3-D diffuse objects. App Opt 23: 3105–3108
186. Vander R, Lipson SG, Leizerson I (2003) Fourier fringe analysis with improved spatial resolution. Appl Opt 42: 6830–6837
187. Quan C, Tay C, Yang F et al. (2005) Phase extraction from a single fringe pattern based on guidance of an extreme map. Appl Opt 44: 4814–4821
188. Kinell L (2004) Spatiotemporal approach for real-time absolute shape measurements by use of projected fringes. Appl Opt 43: 3018–3017
189. Hu X, Liu G, Hu C et al. (2006) Characterization of static and dynamic microstructures by microscopic interferometry based on a Fourier transform method. Meas Sci Technol 17: 1312–1318
190. Shulev A, Gotchev A, Foi A et al. (2006) Threshold selection in transform-domain denoising of speckle pattern fringes. In: Proc. SPIE 6252, pp. 21–27
191. Lovric D, Vucic Z, Gladic J et al. (2003) Refined Fourier-transform method of analysis of full two-dimensional digitized interferograms. Appl Opt 42: 1477–1484
192. Li J, Su X, Guo L (1990) Improved Fourier transform profilometry of automatic of 3-D object shapes. Opt Eng 29: 1430–1444
193. Vucic Z, Gladic J (2005) Phase retrieval errors in standard Fourier fringe analysis of digitally sampled model interferograms. Appl Opt 44: 6940–6948
194. Vanherzeele J, Guillaume P, Vanlanduit S (2005) Fourier fringe processing using a regressive Fourier-transform technique. Opt Las Eng 43: 645–658
195. Li JL, Su XY, Su HJ et al. (1998) Removal of carrier frequency in phase-shifting techniques. Opt Las Eng 30: 107–115
196. Lu M, He X, Liu S (2000) Powerful frequency domain algorithm for frequency identification for projected grating phase analysis and its applications. Opt Eng 39: 137–142
197. Chen L, Quan C (2005) Fringe projection profilometry with nonparallel illumination: a least-squares approach. Opt Lett 30: 2101–2104
198. Srinivasan V, Liu H, Halioua M (1985) Automated phase-measuring profilometry: a phase mapping approach. J Opt Soc Am A 24: 185–188
199. Zhou W, Su X (1994) A direct mapping algorithm for phase-measuring profilometry. J Mod Opt 41: 89–94
200. Chen L, Tay CJ (2006) Carrier phase component removal: a generalized least-squares approach. J Opt Soc Am A 23: 435–443
201. Takeda M, Yamamoto H (1994) Fourier-transform speckle profilometry: three-dimensional shape measurements of diffuse objects with large height steps and/or spatially isolated surfaces. Appl Opt 33: 7829–7837
202. Onodera R, Ishii Y (1998) Two-wavelength interferometry that uses a Fourier-transform method. Appl Opt 37: 7988–7993
203. Takeda M, Kitoh M (1992) Spatiotemporal frequency multiplex heterodyne interferometry. J Opt Soc Am A 9: 1607–1614
204. Burton D, Lalor M (1994) Multichannel Fourier fringe analysis as an aid to automatic phase unwrapping. Appl Opt 33: 2939–2948
205. Takeda M, Gu Q, Kinoshita M et al. (1997) Frequency-multiplex Fourier-transform profilometry: a single-shot three-dimensional shape measurement

of objects with large height discontinuities and/or surface isolations. Appl Opt 36: 5347–5354
206. Gushov V, Solodkin Y (1991) Automatic processing of fringe patterns in integer interferometers. Opt Las Eng 14: 311–324
207. Takeda M, Aoki T, Miyamoto Y et al. (2000) Absolute three-dimensional shape measurements using coaxial and coimage plane optical systems and Fourier fringe analysis for focus detection. Opt Eng 39: 61–68
208. Bulut K, Naci Inci M (2005) Three-dimensional optical profilometry using a four-core optical fibre. Opt Las Tech 37: 463–469
209. Kreis T (1986) Digital holographic interference phase measurement using the Fourier-transform method. J Opt Soc Am A 3: 847–856
210. Larkin KG, Bone D, Oldfield M (2001) Natural demodulation of two-dimensional fringe patterns. I. General background of the spiral phase quadrature transform. J Opt Soc Am A 18: 1862–1870
211. Larkin KG, Bone D, Oldfield M (2001) Natural demodulation of two-dimensional fringe patterns. II. Stationary phase analysis of the spiral phase quadrature transform. J Opt Soc Am A 18: 1871–1881
212. Jesacher A, Fürhapter S, Bernet S et al. (2006) Spiral interferogram analysis. J Opt Soc Am A 23: 1400–1409
213. Tomassini P, Giulietti A, Gizzi L et al. (2001) Analyzing laser plasma interferograms with a continuous wavelet transform ridge extraction technique: the method. Appl Opt 40:6561–6568
214. Qian K (2004) Windowed Fourier transform for fringe pattern analysis. Appl Opt 43: 2695–2702
215. Sciammarella C, Kim T (2003) Determination of strains from fringe patterns using space-frequency representations. Opt Eng 42: 3182–3193
216. Watkins L (2007) Phase recovery from fringe patterns using the continuous wavelet transform. Opt Las Eng 45: 298–303
217. Marroquin J, Rivera M (1995) Quadratic regularization phase functional for phase unwrapping. J Opt Soc Am A 12: 2393–2400
218. Colonna de Lega X (1997) Processing of non-stationary interference patterns: adapted phase shifting algorithms and wavelet analysis. Application to dynamic deformation measurements by holographic and speckle interferometry. Swiss Federal Institute of Technology.
219. Daubechies I (1992) Ten lectures on wavelets, PA: SIAM, Philadelphia.
220. Watkins LR, Tan SM, Barnes TH (1999) Determination of interferometer phase distributions by use of wavelets. Opt Lett 24: 905–907
221. Federico A, Kaufmann G (2002) Evaluation of the continuous wavelet transform method for the phase measurement of electronic speckle pattern interferometry fringes. Opt Eng 41: 3209–3216
222. Kadooka K, Kunoo K, Uda N et al. (2003) Strain analysis for moiré interferometry using the two-dimensional continuous wavelet transform. Exp Mech 43: 45–51
223. Belyakov A, Gurov I (2003) Analyzing interference fringes by the wavelet method. J Opt Tech 70: 13–17
224. Daubechies I (1990) The wavelet transform, time-frequency localization and signal analysis. IEEE Trans I 36: 961–1005
225. Dursun A, Ozder S, Ecevit F (2004) Continuous wavelet transform analysis of projected fringe patterns. Meas Sci Technol 15: 1768–1772

226. Belyakov A (2006) Analyzing interference-fringe patterns by discriminating the features of wavelet maps of symmetric wavelets. J Opt Tech 73: 183–187
227. Zheng R, Wang Y, Zhang X et al. (2005) Two-dimensional phase-measuring profilometry. Appl Opt 44 : 954–958
228. Carmona R, Hwang W, Torresani B (1997) Characterization of Signals by the Ridges of Their Wavelet Transforms. IEEE Trans Sig Proccess 45: 2586–2590
229. Liu H, Cartwright A, Basaran C (2004) Moire interferogram phase extraction: a ridge detection algorithm for continuous wavelet transforms. Appl Opt 43: 850–857
230. Afifi M, Fassi-Fihri A, Marjane M et al. (2002) Paul wavelet-based algorithm for optical phase distribution evaluation. Opt Com 211: 47–51
231. Zhong J, Weng J (2004) Spatial carrier-fringe pattern analysis by means of wavelet transform: wavelet transform profilometry. Appl Opt 43: 4993–4998
232. Qian K, Seah H, Asundi A (2005) Fault detection by interferometric fringe pattern analysis using windowed Fourier transform. Meas Sci Technol 16: 1582–1587
233. Zhou J (2005) Wavelet-aided spatial carrier fringe pattern analysis for 3-D shape measurement. Opt Eng 44: 113602.
234. Liu H, Cartwright A, Basaran C (2003) Sensitivity improvement in phase-shifted moiré interferometry using 1-D continuous wavelet transform image processing. Opt Eng 42: 2646–2652
235. Liu H, Cartwright A, Basaran C (2004) Experimental verification of improvement of phase shifting moire interferometry using wavelet-based image processing. Opt Eng 43: 1206–1214
236. Li H, Chen H, Zhang J et al. (2007) Statistical searching of deformation phases on wavelet transform maps of fringe patterns. Opt Las Eng **39: 275–281**
237. Miao H, Quan C, Tay CJ et al. (2007) Analysis of phase distortion in phase-shifted fringe projection. Opt Las Tech 45: 318–325
238. Li X (2000) Wavelet transform for detection of partial fringe patterns induced by defects in non-destructive testing of holographic interferometry and electronic speckle pattern interferometry. Opt Eng 39: 2821–2827
239. Chang RS, Sheu J, Lin CH et al. (2003) Analysis of CCD moire pattern for micro-range measurements using the wavelet transform. Opt Las Tech 35: 43–47
240. Qian K, Soon S, Asundi A (2003) Phase-shifting windowed Fourier ridges for determination of phase derivatives. Opt Lett 28: 1657–1659
241. Qian K (2004) Windowed Fourier transform method for demodulation of carrier fringes. Opt Eng 43: 1472–1473
242. Qian K, Soon S (2005) Two-dimensional windowed Fourier frames for noise reduction in fringe pattern analysis. Opt Eng 44: 075601.
243. Yao W, He A (1999) Application of Gabor transformation to the twodimensional projection extraction in interferometric tomography. J Opt Soc Am A 16: 258–263
244. Jun W, Asundi A (2002) Strain contouring with Gabor filters: filter bank design. Appl Opt 41: 7229–7236
245. Zhong J, Weng J (2004) Dilating Gabor transform for the fringe analysis of 3-D shape measurement. Opt Eng 43: 895–899.
246. Marroquin J, Rodriguez-Vera R, Servin M (1998) Local phase from local orientation by solution of a sequence of linear systems. J Opt Soc Am A 15: 1536–1544

247. Servin M, Marroquin J, Cuevas F (2001) Fringe-follower regularized phase tracker for demodulation of closed-fringe interferograms. J Opt Soc Am A 18: 689–695
248. Marroquin J, Figueroa J, Servin M (1997) Robust quadrature filters. J Opt Soc Am A 14: 779–791
249. Rivera M, Marroquin J, Botello S et al. (2000) Robust spatiotemporal quadrature filter for multiphase stepping. Appl Opt 39: 284–292
250. Servin M, Quiroga J, Marroquin J (2003) General $n$-dimensional quadrature transform and its application to interferogram demodulation. J Opt Soc Am A 20: 925–934
251. Marroquin J, Servin M, Rodriguez-Vera R (1997) Adaptive quadrature filters and the recovery of phase from fringe pattern images. J Opt Soc Am A 14: 1742–1753
252. Villa J, De la Rosa I, Miramontes G et al. (2005) Phase recovery from a single fringe pattern using an orientational vector-field-regularized estimator. J Opt Soc Am A 22: 2766–2773
253. Zhou X, Baird J, Arnold J (1999) Fringe-Orientation Estimation by use of a Gaussian Gradient Filter and Neighboring-Direction Averaging. Appl Opt 38: 795–804
254. Canabal H, Quiroga J, Bernabeu E (1998) Automatic processing in moire deflectometry by local fringe direction calculation. Appl Opt 37: 5894–5901
255. Villa J, Quiroga J, Servin M (2000) Improved regularized phase-tracking technique for the processing of squared-grating deflectograms. Appl Opt 39: 502–508
256. Servin M, Malacara D, Cuevas F (1994) Direct phase detection of modulated Ronchi rulings using a phase locked loop. Opt Eng 33: 1193–1199
257. Gdeisat M, Burton D, Lalor M (2000) Real-time fringe pattern demodulation with a second-order digital phase-locked loop. Appl Opt 39: 5326–5336
258. Gdeisat M, Burton D, Lalor M (2002) Fringe pattern demodulation with a two-frame digital phase-locked loop algorithm. Appl Opt 41: 5471–5578
259. Servin M, Marroquin J, Quiroga J (2004) Regularized quadrature and phase tracking from a single closed-fringe interferogram. J Opt Soc Am A 21: 411–419
260. Rivera M (2005) Robust phase demodulation of interferograms with open or closed fringes. J Opt Soc Am A 22: 1170–1175
261. Legarda-Saenz R, Osten W, Jüptner W (2002) Improvement of the regularized phase tracking technique for the processing of nonnormalized fringe patterns. Appl Opt 41: 5519–5526
262. Rivera M, Rodriguez-Vera R, Marroquin J (1997) Robust procedure for fringe analysis. Appl Opt 36: 8391–8396
263. Cuevas F, Sossa-Azuela J, Servin M (2002) A parametric method applied to phase recovery from a fringe pattern based on a genetic algorithm. Opt Commun 203: 213–223
264. Joo W, Cha S (1996) Knowledge-based hybrid expert system for automated interferometric data reduction. Opt Las Eng 24: 57–75
265. Robin E, Valle V, Brémand F (2005) Phase demodulation method from a single fringe pattern based on correlation with a polynomial form. Appl Opt 44: 7261–7269
266. Gurov I, Sheynihovich D (2000) Interferometric data analysis based on Markov nonlinear filtering methodology. J Opt Soc Am A 17: 21–26

267. Reich C, Ritter R, Thesing J (2000) 3-D shape measurement of complex objects by combining photogrammetry and fringe projection. Opt Eng 39: 224–231
268. Kowarschik R, Kuhmstedt P, Gerber J et al. (2000) Adaptive optical three-dimensional measurement with structured light. Opt Eng 39: 150–158
269. Kreis T, In: Rastogi PK (ed) Holographic Interferometry: Principles and Methods, Springer, Heidelberg, pp. 151–212
270. Tay CJ, Quan C, Yang FJ et al. (2004) A new method for phase extraction from a single fringe pattern. Opt Commun 239: 251–258
271. Liebling M, Blu T, Unser M (2004) Complex-wave retrieval from a single off-axis hologram. J Opt Soc Am A 21: 367–377
272. De Angelis M, De Nicola S, Ferraro P et al. (2005) Profile measurement of a one-dimensional phase boundary sample using a single shot phase-step method. Opt Las Eng 43: 1305–1314
273. Skydan O, Lalor M, Burton D (2005) Using coloured structured light in 3-D surface measurement. Opt Las Eng 43: 801–814
274. Yoneyama S, Morimoto Y, Fujigaki M et al. (2003) Three dimensional surface profile measurement of moving object by a spatial-offset phase stepping method. Opt Eng 42, 137–142
275. Zhang S, Yau S (2006) High-resolution, real-time 3D absolute coordinate measurement based on a phase-stepping method. Opt. Express 14: 2644–2654
276. Lu C, Xiang L (2003) Optimal intensity-modulation projection technique for three-dimensional shape measurement. Appl Opt 42: 4649–4657
277. Arai Y, Yokozeki S, Yamada T (1995) Fringe-scanning method using a general function for shadow moiré. Appl Opt 34: 4877–4882
278. Awatsuji Y, Sasada M, Fujii A et al. (2006) Scheme to improve the reconstructed image in parallel quasi-phase-shifting digital holography. Appl Opt 45: 968–974
279. Huang P, Hu Q, Jin F et al. (1999) Color-encoded digital fringe projection technique for high-speed three-dimensional surface contouring. Opt Eng 38:1065–1071
280. Coggrave C, Huntley J (2000) Optimization of a shape measurement system based on spatial light modulators. Opt Eng 39: 91–98
281. Goodman J (2004) Introduction to Fourier Optics, Roberts & Company Publishers